NOTICE

The quality of this microform is heavily dependent upon the quality of the original thesis submitted for microfilming. Every effort has been made to ensure the highest quality of reproduction possible.

If pages are missing, contact the university which granted the degree.

Some pages may have indistinct print especially if the original pages were typed with a poor typewriter ribbon or if the university sent us an inferior photocopy.

Reproduction in full or in part of this microform is governed by the Canadian Copyright Act, R.S.C. 1970, c. C-30, and subsequent amendments.

AVIS

La qualité de cette microforme dépend grandement de la qualité de la thèse soumise au microfilmage. Nous avons tout fait pour assurer une qualité supérieure de reproduction.

S'il manque des pages, veuillez communiquer avec l'université qui a conféré le grade.

La qualité d'impression de certaines pages peut laisser à désirer, surtout si les pages originales ont été dactylographiées à l'aide d'un ruban usé ou si l'université nous a fait parvenir une photocopie de qualité inférieure.

La reproduction, même partielle, de cette microforme est soumise à la Loi canadienne sur le droit d'auteur, SRC 1970, c. C-30, et ses amendements subséquents.

Numerical Modelling of Ice Cover Melting Under Turbulent Flow Conditions

Raafat G. Saadé

A Thesis
in
The Department
of
Civil Engineering

Presented in Partial Fulfillment of the Requirements
for the Degree of Master of Applied Science at
Concordia University
Montréal, Québec, Canada

December 1990

ISBN 0-315-68734-7

ABSTRACT

Numerical Modelling of Ice Cover Melting Under
Turbulent Flow Conditions

Raafat G. Saadé

Ice covers are formed on rivers in cold regions for most of the winter season. This affects the usage of these rivers for transportation, power generation, water supply and municipal and industrial waste water disposal. The discharge of waste heat into these rivers result in rising the water temperature and in suppressing the ice cover from growing.

The present thesis deals with the formulation and implementation of a two-dimensional turbulence model which simulates the turbulent flow characteristics, thermal distribution, and ice cover melting, of an ice covered river. The unsteady depth-averaged continuity and St. Venant momentum equations that govern the flow regime are used. Turbulent flow characteristics that effect the ice cover melting process are evaluated, based on the depth-averaged (k-ε) turbulence model, where k is the local turbulent kinetic energy and ε is the rate of its dissipation. Consequently, ice cover melting is determined by establishing the heat budget at the water-ice and ice-air interfaces.

An explicit finite difference method was used for the solution of the hydrodynamic equations. The method is based on the Modified MacCormack scheme, which involves the splitting of a two-dimensional calculation into sequences of two one-dimensional operations. The upwind scheme is used for the descretization of the temperature, k, and ε equations.

Three series of tests have been performed using the turbulence model, for the evaluation of its performance. The first series of tests dealt mainly with the verification of the model capability in predicting hydrodynamic conditions, which is very important since inaccurate hydrodynamic predictions result in inaccurate evaluations of ice cover melting. The model compares well with other measured and computed hydrodynamic results. Once that the hydrodynamic computations were verified, verification of ice cover melting predictions were performed by numerically reproducing 6 laboratory experiment. The model predictions compares excellent with some of the experiments and satisfactory with others. The primary reason would be due to the difficulty in experimenting with ice. The third series of tests is concerned with a field study done on the Mississippi river. A comparison of hydrodynamic conditions, temperature distributions and ice free openings were carried out, with good agreement in all counts.

DEDICATION

This thesis is dedicated to the memory of my father, George Christo Saadé

"To the son He saw in me"

ACKNOWLEDGEMENT

I take this opportunity to thank my thesis advisor, Dr. Semaan Sarraf, for his patience towards my ignorance, his willingness to teach me what he knows and his guidance in the completion of the thesis.

I also wish to thank my sister Tina for bearing with me during my undergraduate years. Also I would like to show my everlasting indebtness to my parents Georges and Eleonore for their love and support that they have given me, and continue to do so.

Last but not least, I would like to express my sincere appreciation to my wife Christina for her support and understanding while carrying out this thesis.

TABLE OF CONTENT

Page

LIST OF FIGURES

LIST OF TABLES

LIST OF SYMBOLS

a	=	annual variation in solar radiation constant, in cal $cm^{-2}day^{-1}$
b	=	annual variation in solar radiation constant
C	=	cloud cover, in tenths
C_c	=	coefficient for ice cover reduction in conductive heat transfer
C_e	=	coefficient for ice cover reduction in evapo-condensation heat flux
C_{el}	=	celerity of water wave, in m s^{-1}
C_p	=	specific heat of water, in cal kg^{-1} $°C^{-1}$
C_{wi}	=	heat transfer constant water to ice, in cal $\cdot^{-0.2}$ $m^{-2.6}$ $°C^{-1}$
c	=	empirical constant for atmospheric radiation
D_x	=	longitudinal dispersion coefficient in x direction, in m^2 s^{-1}
D_y	=	longitudinal dispersion coefficient in y direction, in m^2 s^{-1}
d	=	empirical constant for atmospheric radiation
e_a	=	air vapour pressure, in mb
e_s	=	saturation vapour pressure, in mb
G	=	production of turbulent kinetic energy by the interaction of turbulent stresses with horizontal mean velocity gradients.
g	=	gravitational acceleration, in m s^{-2}

h	=	water depth, in m
h_{wi}	=	heat transfer coefficient at water-ice interface, in cal m^{-2} s^{-1} $°C^{-1}$
k	=	turbulent kinetic energy
K_i	=	ice thermal conductivity, in cal $m^{-1}s^{-1}$ $°C^{-1}$
k_c	=	empirical constant for atmospheric radiation
k_n	=	coefficient for free convection
k_x	=	longitudinal dispersion constant in x direction
k_y	=	longitudinal dispersion constant in y direction
L_i	=	latent heat of fusion, in cal kg^{-1}
L_x	=	McCormack operator x-direction backward predictor,forward corrector
L_y	=	McCormack operator y-direction backward predictor,forward corrector
L'_x	=	McCormack operator x-direction forward predictor,backward corrector
L'_y	=	McCormack operator y-direction forward predictor,backward corrector
n	=	Combined Manning's coefficient
n_b	=	Manning's coefficient of river bed
n_i	=	Manning's coefficient of the underside of ice cover
q_{wi}	=	heat flux, water to ice cover, in cal $m^{-2}s^{-1}$
R	=	hydraulic radius, in m

S_{fx} = friction slope in the x-direction

S_{fy} = friction slope in the y-direction

S_{ox} = bed slope in the x-direction

S_{oy} = bed slope in the y-direction

T = water temperature, in °C

T_a = air temperature, in °C

T_{ak} = air temperature, in °K

T_f = freezing point temperature, in °C

T_i = ice cover internal temperature, in °C

T_s = ice top surface temperature, in °C

T_{sk} = ice top surface temperature, in °K

t = time, in seconds

Δt = time step, in seconds

Δt_2 = one half the time step, in seconds

U = unit discharge in the longitudinal direction, in $m^2 s^{-1}$

U^* = shear velocity in x-direction, in $m s^{-1}$

u = flow velocity component in x-direction, in $m s^{-1}$

V = unit discharge in y-direction, in $m^2 s^{-1}$

V^* = shear velocity in y-direction, in $m s^{-1}$

VV = resultant water velocity, in $m s^{-1}$

V_a = wind velocity at 2 m above surface, in $m s^{-1}$

v = flow velocity component in y-direction, in $m s^{-1}$

x,y	=	space coordinates in planar directions, in m
Δx	=	grid spacing in the x-direction, in m
Δy	=	grid spacing in the y-direction, in m
Z_f	=	bed elevation, in m
z	=	space coordinate in the vertical direction, in m
α	=	surface albedo
α_a	=	empirical constant for ice surface albedo
α_i	=	empirical constant for ice surface albedo
β_i	=	fraction of solar radiation which penetrates ice-water interface
$\Delta\theta_s$	=	ice thickness change at top surface, in m
$\Delta\theta_w$	=	ice thickness change at bottom surface, in m
ε	=	dissipation of turbulent kinetic energy
ε_s	=	emissivity of water or ice surface
θ	=	ice thickness, in m
ρ	=	water density, in kg m^{-3}
ρ_i	=	ice density, in kg m^{-3}
σ	=	Stefan-Boltzman constant, in cal cm^{-2} day^{-1}
τ_i	=	bulk extinction coefficient, in cm^{-1}

τ_{bx} = bottom shear stress in x-direction

τ_{by} = bottom shear stress in y-direction

τ_{sx} = surface shear stress in x-direction, in kg s^{-2} m^{-1}

τ_{sy} = surface shear stress in y- direction, in kg s^{-2} m^{-1}

τ_{ij} = turbulent shear stresses

Φ = source term, in °C m s^{-1}

ϕ = heat transfer to water, in cal cm^{-2} day^{-1}

ϕ_b = effective back radiation, in cal cm^{-2} day^{-1}

ϕ_{ba} = atmospheric radiation, in cal cm^{-2} day^{-1}

ϕ_{bn} = net atmospheric radiation, in cal cm^{-2} day^{-1}

ϕ_{bs} = longwave radiation emitted by the river surface, in cal cm^{-2} day^{-1}

ϕ_c = conductive heat transfer, in cal cm^{-2} day^{-1}

ϕ_e = evapo-condensation flux, in cal $cm^{-2}day^{-1}$

ϕ_{lat} = latitude on earth's surface, in degrees

ϕ_{ri} = incoming shortwave radiation, in cal cm^{-2} day^{-1}

ϕ_s = net shortwave radiation, in cal cm^{-2} day^{-1}

ϕ_{sp} = shortwave penetration into the waterbody, in cal cm^{-2} day^{-1}

ψ = dummy variable

CHAPTER 1.0
INTRODUCTION

Background

Rivers in cold regions freeze for most of the winter season, resulting in the formation of an ice cover that affects their use for transportation, power generation, water supply and waste water disposal. Although the discharge of warm water into rivers may conflict with environmental regulations, yet the resulting rise in temperature can be effective in suppressing the ice cover formation. This heat can be sufficient to keep major reaches of rivers ice free. Several investigators have performed studies on the prediction of the ice-free lengths in river reaches after a period of ice cover melting. The capability of predicting the magnetude and extent of ice cover melting due to an addition of heated thermal effluents, is important for the efficient use of rivers during the winter season. The maximum effectiveness of the disposed heated water is obtained by suppressing the ice cover from forming, thereby extending the navigation period in rivers during ice covered seasons, thereby implying economical advantages.

The subject of ice cover melting due to warm water has been previously approached by a number of researchers. Pruden, et al. (1954), studied the feasibility of keeping much of the St. Lawrence river free from ice for parts of the winter. Kreith (1958), considered the melting rate of an ice cover where the problem of heat transfer from a moving liquid to the solid boundary was formulated as a boundary value problem. Ashton (1971), performed a study on the patterns exhibited by an

ice-water interface while freezing or melting, thus finding the existence of two-dimensional wavy boundary whose crests are oriented transverse to the flow direction. It was then hypothesised that the heat flux to the interface is sinusoidal and that the mean heat flux is proportional to the ratio of amplitude and wavelength of the ripples underneath the ice cover. Hsu (1973), extended the work of Ashton and verified the quasi-steadiness of the heat conduction through the ice slab. Gallardo (1974), measured the vertical temperature distribution of the flow, and the effects of air and water characteristics on the vertical displacement of the ice-water interface during the melting of an ice cover. Gallardo found that under laboratory conditions, and air temperatures close to the freezing mark, the effect of the heat transfer coefficient at the ice-air interface was small compared with the other expressions. However, for temperatures of the air lower than -10^0C the rate of heat transfer to the air cannot be neglected. Hewlett (1976), investigated the rate of melting of an ice cover due to a heat source. The investigation showed that the leading edge motion of an ice cover under various air and water conditions is possible through the application of the general heat balance equations if the heat transfer coefficient distribution can be properly estimated.

Field studies were also conducted to evaluate the process of river ice cover melting by a thermal effluent. Dingman et al. (1970), carried out a study on the North Saskatchewan River at Edmonton, Alberta, while Ashton (1981), conducted a study on the Mississippi River at Bettendorf, Iowa. Field data on many aspects of ice melting was collected during the study period. Also, Hayes and Ashton (1985), collected data downstream of the power plants in the Pittsburgh and Pennsylvania areas to further test their model.

Dingman et. al. (1967), presented a one-dimensional solution of the steady-state energy equation. The diffusion terms were neglected and the velocity field assumed to be uniform. Paily et. al. (1974), solved the one-dimensional unsteady energy equation including the longitudinal dispersion terms. A linearisation of heat exchange relations were developed and used in the solution. Ashton (1979), solved the one-dimensional quasi-steady energy equation. Heat transfer processes at the ice cover interfaces were considered as well as varying meteorological conditions. Shen and Chiang (1984), developed a one-dimensional model of the ice cover growth and decay on the St. Lawrence River by using a uniform velocity field and including a complete ice cover and open water heat transfer formulation. Al-Salah et. al. (1987), performed an analytical solution of the one-dimensional energy equation, including converging or diverging river flow using a linear heat transfer relation in the solution. Plouffe (1987), used a two-dimensional constant viscosity model to predict the local river ice cover melting due to a side-discharge thermal effluent.

The process of melting of an ice cover caused by the flow of warm water from underneath the ice cover is greatly affected by the turbulent flow characteristics underneath the ice cover, and the heat fluxes across the interfaces of the ice cover. The turbulent flow under an ice cover presents different flow characteristics than those of open water, such that the ice cover increases in the flow resistance, resulting in a reduction of the average flow velocity and an increase in the normal depth. Therefore, the simulation of turbulent flow conditions under an ice cover, for the prediction of ice cover melting is of great importance.

Scope of Research

The present research aims at studying the melting of an ice cover due to added heat under turbulent flow conditions. The study made use of a two-dimensional turbulence model to determine the turbulent flow characteristics, and the temperature distribution affecting the melting of the ice cover.

The model uses: the depth-averaged two-dimensional St. Venant equations to solve for the velocity field; the two-dimensional heat transport equation to solve for the temperature distribution; the k and ε equations to evaluate the turbulent kinetic energy and the rate of its dissipation; and ice equations to compute the growth and melting of a floating ice cover.

The solution to the hydrodynamic equations was obtained through the application of a Modified version of the MacCormack scheme. The solution to the temperature, turbulent kinetic energy k, and the rate of dissipation of the turbulent kinetic energy ε equations were obtained by the use of the upwind finite difference scheme. The model uses the inlet, outlet, initial and boundary conditions to start the calculations procedure. The solution procedure for evaluating the flow characteristics is described by the following computational steps: velocity field and depth distribution; heat source term; temperature distribution; k and ε distribution; and ice cover melting.

The solution to the hydrodynamic, temperature, and turbulence equations was verified against previous work done by McGuirk and Rodi. Also, the ice cover melting predictions were compared to five laboratory experiments and a set of field data. Results show an overall good performance of the model and excellent agreement with both experimental and field data.

CHAPTER 2.0

GOVERNING EQUATIONS

2.1 Hydrodynamic Equations

The St. Venant shallow water equations are used to calculate the flow field. These equations are obtained by integrating the equations of motion over the depth, using the hydrostatic approximation. The symbol definition is presented in figure 2.1. The unsteady depth-averaged continuity and momentum equations that govern the flow regime for an open channel under ice cover conditions, are expressed as follows:

Continuity

$$[2.1] \quad \frac{\partial h}{\partial t} + \frac{\partial uh}{\partial h} + \frac{\partial vh}{\partial y} = 0$$

Conservation of momentum in x direction:

$$[2.2] \quad \frac{\partial U}{\partial t} + \frac{\partial E}{\partial x} + \frac{\partial F}{\partial y} = \frac{\partial}{\partial x}\left(\frac{\tau_{xx}}{\rho}\right) + \frac{\partial}{\partial y}\left(\frac{\tau_{xy}}{\rho}\right) + \frac{\tau_{sx}}{\rho} - \frac{\tau_{bx}}{\rho} + gh\frac{\partial \Pi}{\partial x}$$

Conservation of momentum in y direction:

$$[2.3] \quad \frac{\partial V}{\partial t} + \frac{\partial G}{\partial x} + \frac{\partial S}{\partial y} = \frac{\partial}{\partial x}\left(\frac{\tau_{yx}}{\rho}\right) + \frac{\partial}{\partial y}\left(\frac{\tau_{yy}}{\rho}\right) + \frac{\tau_{sy}}{\rho} - \frac{\tau_{by}}{\rho} + gh\frac{\partial \Pi}{\partial x}$$

[2.4] $E = u^2h$

[2.5] $F = uvh$

[2.6] $G = v^2h$

[2.7] $\Pi = H + 0.9\,\theta$

where $H=h+Z_b$ is the water surface elevation from the datum; h is the water depth; τ_b is the bottom elevation from datum; θ is the thickness of the ice cover; τ_{sx}, τ_{sy} are surface shear stresses; uh and vh are the unit discharges in the x and y directions respectively; τ_{bx}, and τ_{by} are bottom shear stresses per unit mass in the x and y directions respectively expressed as follows:

[2.8] $$\frac{\tau_{bx}}{\rho} = g\,h\,S_{fx}$$

[2.9] $$\frac{\tau_{by}}{\rho} = g\,h\,S_{fy}$$

such that,

S_{ox} and S_{oy} are the river bed slopes, and S_{fx} and S_{fy} are the friction slopes given by the following equations:

[2.10] $$S_{fx} = \frac{n^2 u q}{R^{4/3}}$$

[2.11] $$S_{fy} = \frac{n^2 v q}{R^{4/3}}$$

where

$$[2.14] \quad q = (u^2 + v^2)^{1/2}$$

h is replaced by R (hydraulic radius) in the friction slope terms, to account for the presence of an ice cover. In other words,

R = h for open water case, wide river assumption.

R = 1/2 h for ice-covered flow case, wide river assumption

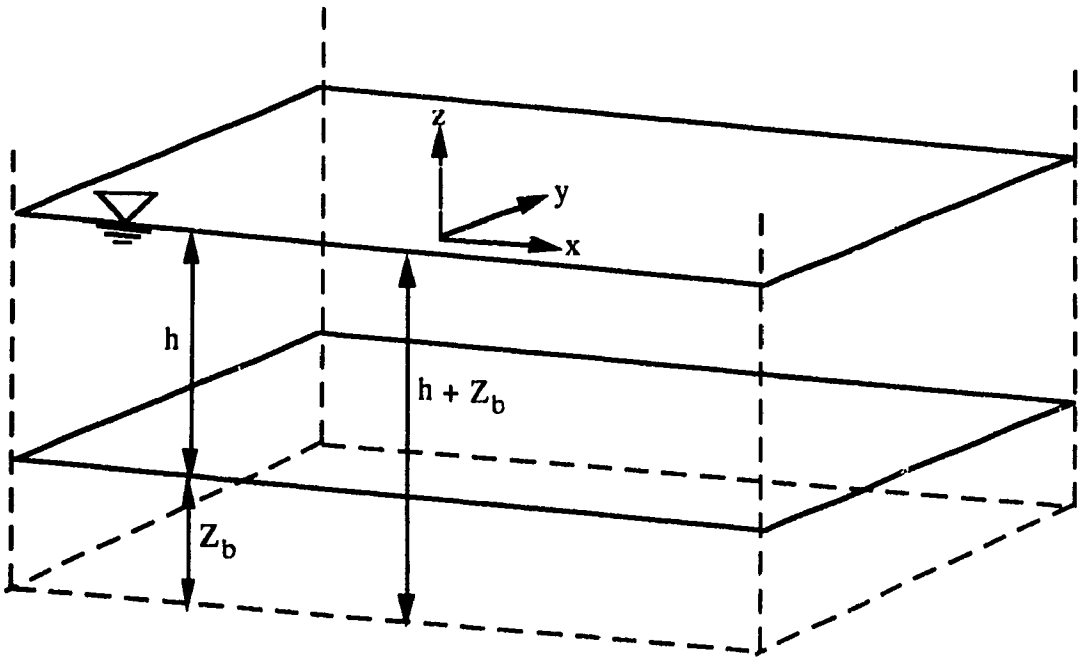

Figure 2.1: Symbol definition

Under ice cover conditions, where the flow is confined the Manning coefficient found in the friction slope terms should relate to the river bed roughness and the underside roughness of the ice cover. The resulting composite Manning coefficient is (Wankiewicz 1984):

$$[2.13] \quad n = \left(\frac{n_b^{3/2} + n_i^{3/2}}{2} \right)^{2/3}$$

where n_b is the bed Manning coefficient and n_i is the ice underside Manning coefficient.

The ice cover also effects the hydrostatic pressure terms in the hydrodynamic equations in which 92% of the ice cover thickness is added to the water depth . The 92% value represent the density ratio between ice and water.

2.2 Shear Stress Computation

Computation of the shear stress terms present in the momentum equations is based on the eddy viscosity concept. The latter is based on the assumption that the turbulent stresses are proportional to the mean velocity gradient. The depth-averaged turbulent stresses can then be represented by the following expression, using tensor notations (McGuirk and Rodi 1978)

$$[2.14]\quad \frac{\tau_{ij}}{\rho} = \nu_t h \left[\frac{\partial u_i}{\partial x_j} + \frac{\partial u_j}{\partial x_i}\right] - \frac{2}{3} k h \delta_{ij}$$

δ_{ij}: Kroneker symbol

$$\text{if } i = j \rightarrow \delta_{ij} = 1$$

$$\text{if } i \neq j \rightarrow \delta_{ij} = 0$$

or, in x, y coordinates,

$$[2.15]\quad \frac{\tau_{xx}}{\rho} = \nu_t \left(2\frac{\partial uh}{\partial x}\right) - \frac{2}{3} kh$$

$$[2.16]\quad \frac{\tau_{xy}}{\rho} = \frac{\tau_{yx}}{\rho} = \nu_t \left(\frac{\partial uh}{\partial y} + \frac{\partial vh}{\partial x}\right)$$

$$[2.17]\quad \frac{\tau_{yy}}{\rho} = \nu_t \left(2\,\frac{\partial vh}{\partial y}\right) - \frac{2}{3}\,kh$$

where ν_t represents the turbulent or eddy viscosity as a function of the state of turbulence at various points in the flow domain, k is the turbulent kinetic energy, and ε is the rate of dissipation of k.

The distribution of the turbulent eddy viscosity is approximated by assuming that the turbulent viscosity is proportional to the characteristic velocity and the length scale of turbulence (macroscale of turbulence, which is a measure of the size of the energy containing eddies) and expressed as follows:

$$[2.18] \quad \nu_t \alpha k^{1/2} l$$

where l is the length scale of turbulence and k is the turbulent kinetic energy.

The estimation of the rate of dissipation of energy ε is obtained by assuming that the input rate of energy at the large scale of turbulence balances with the dissipation rate at the small scale of turbulence (the amount of energy dissipation at the small scales of turbulence equals the rate of supply at the large scales). Using the characteristic velocity and the length scales (Tennekes and Lumsley 1974),

$$[2.19] \quad \varepsilon \alpha \frac{k^{3/2}}{l}$$

Substituting equation [2.19] into equation [2.18] for the length scale l provides an expression for the turbulent eddy viscosity in terms of the turbulence kinetic energy k, and its rate of dissipation ε.

$$[2.20] \quad \nu_t = C_\mu \frac{k^2}{\varepsilon}$$

where C_μ is an empirical constant given in Table 2.1, k is the turbulent kinetic energy and ε is its rate of dissipation. k and ε are calculated from the relevant transport equations (Rodi 1980) described in chapter 5.

2.3 Temperature Equation

The temperature distribution of the flow field is calculated by solving the energy transport equation. The latter is based on the principal of conservation of heat, convected and diffused by the flow, and expressed as a function of the flow properties. An increase in the river water temperature due to an added heat that imposes the melting of an ice cover is simulated by this equation. The distribution of the depth-averaged temperature is given by the following equation:

$$[2.21] \quad \frac{\partial Th}{\partial t} + \frac{\partial u_i h T}{\partial x_i} = \frac{\partial}{\partial x_i}\left[\Gamma_T h \frac{\partial T}{\partial x}\right] + \Phi$$

where T is the temperature; and i represent the two-dimensional vectorial sum.

The turbulent heat diffusion coefficient Γ_T contained in the energy equation is determined over the flow domain by the following relation:

$$[2.22] \quad \Gamma_T = \frac{\nu_t}{\sigma_T}$$

where σ_T is an empirical constant whose value is given in table 2.1, and ν_t is the turbulent viscosity. The source term in the energy equation [2.21] Φ, takes into account the solar radiation components and meteorological conditions that have an added effect on the calculation of the temperature. These components will be defined in chapter 3.0. The heat source term is evaluated from the combination of the heat flux components as follows:

$$[2.23] \quad \Phi = \frac{\phi}{C_p \rho}$$

In the case of ice covered river

$$[2.24] \quad \phi = \phi_{sp} - \phi_{wi}$$

and for open channels

$$[2.25] \quad \phi = \phi_s - \phi_b - \phi_e - \phi_c - \phi_{wa}$$

where ϕ_s is the solar radiation; ϕ_{sp} is the penetrating shortwave radiation; ϕ_b is the longwave radiation; ϕ_e is the evapo-condensation heat flux; ϕ_c is the conductive heat transfer; ϕ_{wi} is the heat flux across the water-ice interface; and ϕ_{wa} is the heat flux across the water-air interface. (Ashton 1979)

The model is also programmed to consider the constant viscosity concept in which the dispersion constants are determined from the following equations [Ashton 1979] :

$$[2.26] \quad \Gamma_x = k_x U^* R$$

$$[2.27] \quad \Gamma_y = k_y V^* R$$

where k_x is the dispersion constant in the x-direction; k_y is the dispersion constant in the y-direction; U^* and V^* are the shear velocity in the longitudinal and transversal directions respectively, given by :

$$[2.28] \quad U^* = \sqrt{S_{fx} g R}$$

$$[2.29] \quad V^* = \sqrt{S_{fy} g R}$$

where S_{fx} and S_{fy} are previously defined.

2.4 k and ε Equations

The depth averaged k - ε turbulence model adopted in this work is based on the Boussinesq eddy viscosity concept, and presented by McGuirk and Rodi, (1978). The depth-averaged turbulent stresses τ_{xx}, τ_{xy}, τ_{yx}, and τ_{yy}, contained in the momentum equations, need to be determined over the flow domain through the application of a turbulence model. The k-ε turbulence model chatacterizes the local state of turbulence by the turbulent kinetic energy k that originates from the turbulent flow, and the rate of its dissipation ε.

The distribution of the depth-averaged turbulence properties can be represented by the following transport equations, where in conservative form are expressed as follows, using tensor notations:

$$[2.30]\quad \frac{\partial \psi h}{\partial t} + \frac{\partial u_i h \psi}{\partial x_i} = \frac{\partial}{\partial x_i}\left(\Gamma_j\, h\, \frac{\partial \psi}{\partial x}\right) + \Phi_j$$

where ψ is a variable that can represent either the turbulent kinetic energy k or its rate of dissipation ε; j is also a variable being either k, or ε; Φ is a source term; and i represents the two-dimensional vectorial sum.

for ψ=k; then j expresses the turbulent kinetic energy k as follows:

$$[2.31]\quad \Gamma_k = \frac{\nu_t}{\sigma_k}$$

and

[2.32] $\Phi_k = G + P_{kv} - \varepsilon h$

for $\psi=\varepsilon$; then j expresses the turbulent kinetic energy rate of dissipation ε, as follows:

[2.33] $\Gamma_\varepsilon = \frac{\nu_t}{\sigma_\varepsilon}$

and

[2.34] $\Phi_\varepsilon = C_1 \frac{\varepsilon}{k} G + P_{\varepsilon v} - C_2 \frac{\varepsilon^2 h}{k}$

where

[2.35] $G = \frac{\nu_t}{h}\left[2\left(\frac{\partial uh}{\partial x}\right)^2 + 2\left(\frac{\partial vh}{\partial y}\right)^2 + \left(\frac{\partial uh}{\partial y} + \frac{\partial vh}{\partial x}\right)^2 \right]$

represents the production of turbulent kinetic energy in the horizontal directions due to interactions of turbulent stresses with horizontal mean velocity gradients; and σ_k, σ_ε, C_1, and C_2 are empirical constants whose values are shown in table 2.1. These empirical constants were determined by Launder and Spalding 1974, who considered various types of flows such as those in pipes, channels, mixing layer, jets and wakes.

Table 2.1: Empirical Constants used in the k-ε model.

(Launder and Spalding 1974)

C_μ	σ_k	σ_ε	σ_T	C_1	C_2
0.09	1.0	1.3	0.5	1.43	1.92

In addition to the turbulent production G, bed and ice bottom roughness contributes significantly to vertical velocity gradients, which by interaction with large turbulent shear stresses, produce turbulence energy in the vertical direction. This vertical turbulence production of energy which is strongly dependent on the top and bottom roughness is absorbed in the P_{kv} and $P_{\varepsilon v}$ terms, which are expressed as follows:

$$[2.36]\quad P_{kv} = \frac{C_f}{h}\, q^4$$

$$[2.37]\quad P_{\varepsilon v} = \frac{C_2\, C_\mu\, C_f^{5/4}}{h^2}$$

where

$$[2.38]\quad q = \sqrt{(u^2 + v^2)}$$

The source term found in the temperature equation is a function of meteorological conditions, solar radiation, and hydrothermal conditions. The evaluation of this term will be discussed in detail in chapter 3.0. The numerical scheme used for the solution to the hydrodynamics , temperature, turbulent kinetic energy, and the rate of dissipation of the turbulent kinetic energy is based on the Modified MacCormack scheme, and will be discussed in chapter 4.0.

The numerical model used for the present work is primarily based on the continuity, momentum, temperature, turbulent kinetic energy, dissipation rate of the turbulent kinetic energy, and ice melting equations. The turbulent kinetic energy and the rate of its dissipation is evaluated through the k-ε equations which are based on the mean velocity. The k and ε are then used to evaluate the turbulent shear stress components in the momentum equations, and the turbulent heat diffusion coefficient found in the temperature balance equation. The velocity distribution is then computed. The heat budget a function of the meteorological conditions, solar radiation,and hydrothermal conditions is then evaluated, therefore estimating a value to the source term in the temperature equation. The temperature is then calculated for the whole flow domain from its corresponding heat balance equation. Finally, the ice cover melting or thickening is then computed through the use of ice cover equations.

CHAPTER 3.0

ICE DECAY AND GROWTH

During the winter season, continuous sub-freezing temperatures which are considerably lower than the temperature of the river or lake, and weak solar radiation, result in a significant amount of heat loss from the river to the atmosphere. These conditions will consequently lead to the cooling of the river or lake and eventual formation and thickening of an ice cover. The ice cover decreases the rate of cooling of the river due to the insulating characteristics of the ice sheet. Afterwards, the water temperature will then stabilise for the remaining part of the winter.

The loss of heat from a river which is not ice covered occur at the water-air interface, while the growing and melting of an ice cover occurs due to the net heat exchange at the water-ice and ice-air interfaces as shown in figure 3.1. The components of the heat exchange at the interfaces are prescribed in terms of shortwave solar radiation, longwave radiation, evapo-condensation heat flux, and convective heat transfer. These components are in turn a function of the, cloud cover, air temperature, wind velocity, and air vapour pressure.

The heat flux across the ice-air interface is usually unsteady and has a transient behaviour due to the continuous fluctuation in the air temperature, such that the ice cover is in a continuous melting or thickening process. However, the heat flux at the water-ice interface is relatively steady and depends only on the river flow conditions. Also, at the bottom surface of the ice cover, the water temperature is assumed to be maintained at the freezing point 0°C.

3.1 Heat Flux Components

The heat flux components that determine the amount of heat being transferred across the interfaces can be best described through figure 3.2. These components which are a function of the meteorological conditions are expressed as follows:

3.1.1 Shortwave Radiation

The amount of incident shortwave radiation ϕ_{cl} is estimated as follows:

[3.1] $\phi_{cl} = \phi_{ri} [0.35 + 0.061 (10-C)]$

where C is the cloudiness expressed in tenths (i.e. C=0 is clear skies, and C=10 is complete cloud cover), and ϕ_{ri} is the incoming shortwave radiation for cloudless skies in cal m^{-2} day^{-1}. The incoming shortwave radiation ϕ_{ri} at the air-ice or air-water interface is expressed by the following formula:

[3.2] $\phi_{ri} = [a-b (\phi_{lat} - 50)] (1 - 0.0065 c^2)$

where a and b are constants that represent annual variations of the solar radiation intensity under clear skies.

Since a portion of the shortwave radiation is reflected back into the atmosphere, the difference between the incident shortwave radiation and the reflected shortwave radiation will determine the energy that is actually absorbed. The amount of reflected shortwave radiation ϕ_{rs} is expressed by the following formula as reported by Dingman et al. 1967,

[3.3] $\phi_{rs} = (0.108\ \phi_{ri} - 6.766*10^{-5}\ \phi_{ri}^2)$

Therefore the amount of energy absorbed by the water is calculated by

[3.4] $\phi_{ea} = \phi_{cl} - \phi_{rs}$

and the net shortwave solar radiation can be written as

[3.5] $\phi_s = (1-\alpha)\ \phi_{ri}$

where α is the surface albedo conveying the mount of reflection or absorption by the water surface, which is approximately equal to 0.1 for the water surface. For the ice surface, the albedo depends on the ice cover material behaviour and for uneven surfaces, the albedo varies with the solar latitude. Table 3.1 provides a set of reported albedo values for various ice conditions.

Table 3.1: Albedo Values for the Great Lakes Ice (shen & chiang 1984)

Ice Identification	Surface Albedo (%)
Clear lake ice (snow free)	10
Refrozen pankace (snow free)	31
Slush ice (snow free)	41
Brash ice (snow between blocks)	41
Snow ice (snow free)	46

The other part of the shortwave radiation that penetrates into the water underneath the ice cover is expressed by the following formula:

[3.6] $\phi_{sp} = \beta_i \phi_s e^{-\tau i \theta}$

where β_i is the fraction of the absorbed solar radiation that penetrates through the ice-water interface; and τ_i is the bulk extinction coefficient, which varies between 0.004 m^{-1} and 0.007 m^{-1} . The penetration of shortwave radiation into the ice cover can be considered as an internal heat source.

3.1.2 Long-wave Radiation

The net loss of heat by the exchange of long-wave radiation with the atmosphere is the difference between the incoming longwave atmospheric radiation received and the back radiation emitted by the water surface. The longwave radiation emitted from the water surface or the ice cover is expressed by the following formula:

[3.7] $\phi_{bs} = \varepsilon_w \alpha T_w^4$

where T_w is the water temperature in ^oK; σ is the Stephan-Boltzman constant equal to $1.171*10^{-1}$cal. m^{-2} day^{-1} $^oK^{-4}$; and ε_w is the emissivity of the water equal to 0.970 which has been established by Anderson (1954) for Lake Hefner.

The incoming longwave atmospheric radiation, ϕ_{ba}, is not measured, but can be related empirically to air temperature, vapour pressure and cloud conditions

(Anderson 1954). Therefore, under clear skies the atmospheric radiation is determined by a relation initially suggested by Brunt (Paily et al.):

$$[3.8] \quad \phi_{ba} = (C + d\sqrt{e_a})\,\sigma T_a^4$$

where T_a is the air temperature in ^oK, e_a is the air vapour pressure in mb, C and d are empirical constants such that Brunt uses 0.55 and 0.052, while Anderson uses 0.68 and 0.036 for the values of C and d respectively.

Under cloudy skies, a different expression for the atmospheric radiation should be used due to the emittion of additional radiation from water and ice particles from underneath the clouds. Therefore, using Boltz's formula, the atmospheric longwave radiation is represented by :

$$[3.9] \quad \phi_{ba} = \sigma T_a^4\ (c + d\sqrt{e_a}\ )(1 + k_c C^2)$$

where k_c is an empirical constant equal to 0.0017. However, Dingman et al suggested a different expression given as follows:

$$[3.10] \quad \phi_{ba} = (a + b\, e_a)\,\sigma T_a^4$$

where

$$[3.11] \quad a = 0.74 + 0.025C \exp[(-1.92)(10^{-4})H]$$

$$[3.12] \quad b = (4.9)(10^{-3}) - (5.4)(10^{-4})C \exp[(-1.97)(10^{-4})H]$$

and 500<=H<=infinity

In the last expression, H is the cloud height, in m. If the clouds are below 500m in height, the cloud height is taken as a constant at 500 m as suggested by Anderson (1954). Due to the 0.97 value of the emissivity of water, its longwave reflectivity is 0.03 such that

[3.13] $\phi_{br} = 0.03\ \phi_{ba}$

is the reflected longwave atmospheric radiation. Therefore, the net lost from the water surface as longwave radiation, ϕ_b (the effective back radiation) can then be calculated:

[3.14] $\phi_b = \phi_{bs} + \phi_{br} - \phi_{ba}$

but from equation [3.21], the effective back radiation becomes

[3.15] $\phi_b = \phi_{bs} - 0.97\phi_{ba}$

substituting in the previously given expression for ϕ_{bs} and ϕ_{ba} gives the following formula for the net heat lost or the effective back radiation:

[3.16] $\phi_b = 1.1358*10^{-7}[\ T_w^4 - (1+k_cC^2)(C+d(e_a)^{1/2})\ T_w^4\ ]$

where ϕ_b is in calories per cm^2 day.

3.1.3 Evapo-condensation and Conductive Heat Flux

Two approaches have been attempted to calculate the evapo-condensation heat flux. The first approach calculates the heat lost due to evaporation through a daily evaporation rate formula given by the following expression:

$$[3.17]\quad E = (0.525*10^{-2} + 1.007*10^{-2}\,Va)\,(e_{sw} - e_a)$$

where E is the evaporation rate in m per day; Va is the average wind velocity at 4m above the water surface in meters per second; e_{sw} is the saturation vapor pressure at the water surface in mb; and e_a is the vapor pressure of the air at a 2m level above the water surface in mb. Saturation vapor pressure may be calculated by:

$$[3.18]\quad \log e_s = -7.90298\left(\frac{373.16}{T_{sk}} - 1\right) + 5.02808\log\left(\frac{373.16}{T_{sk}}\right) - 1.3816 \times 10^{-3}\left(10^{-3.39149\left(\frac{373.16}{T_{sk}} - 1\right)} - 1\right) + 8.1328 \times 10^{-3}\left(10^{3.39149\left(\frac{373.16}{T_{sk}} - 1\right)} - 1\right) + \log(1013.246)$$

The daily evaporation rate is multiplied by suitable constants thus allowing the heat lost as a result of evaporation to be calculated as follows:

$$[3.19]\quad \phi_e = (3.135 + 6.011Va)\,(e_{sw} - e_a)$$

where ϕ_e is in cal per m^2 day.

With the calculation of ϕ_e, the Bowen ratio is then used to calculate the conductive heat transfer ϕ_c. The Bowen ratio is defined as follows:

[3.20] $R = \phi_c / \phi_e$

where R is calculated from

[3.21] $$R = (6.1 * 10^{-4})\ P \left(\frac{T_w - T_a}{e_{sw} - e_a} \right)$$

such that P is the atmospheric pressure in mb.

Assuming that for equation [3.21] 2m wind velocities are used and that P=1000mb, its multiplication by the Bowen ratio gives:

[3.22] $\phi_c = (1.91 + 3.67\ Va)\ (T_w - T_a)$

however, if a 4m level wind velocity is assumed, equations [3.25], [3.27] and [3.30] take the following expressions:

[3.23] $E = (0.525*10^{-2} + 1.229*10^{-2}\ Va)\ (e_{sw} - e_a)$

[3.24] $\phi_e = (3.135 + 7.33Va)\ (e_{sw} - e_a)$

[3.25] $\phi_c = (1.91 + 4.47\ Va)\ (T_w - T_a)$

(Dingman et al, 1967)

The second approach for determining the heat loss due to evaporation and conduction is estimated by using the Rimsha and Donchenko (1957) equations:

[3.26] $\phi_c = (Kn + 3.9\ Va)\ (T_w - T_a)$

[3.27] $\phi_e = (1.56Kn + 6.08\ Va)\ (e_s - e_a)$

where

[3.28] $K_n = 8.0 + 0.35\ (T_w - T_a)$

is a coefficient which represents the portion of heat transfer due to free convection, Va is the wind velocity in meters per second at 2 m above water surface.

It is interesting to note that the wind coefficient in equation [3.27] is very close to that found by Kohler (1954, eq.3.19) . Thus equation [3.19] is a special case of equation [3.35] which is appropriate for $(T_w - T_a) < 1^oC$ (Dingman et al, 1967). The existence of an ice cover over a river tends to suppress evaporation, therefore the heat flux from the ice surface will be a fraction (C_e, C_c) of that calculated before. The evapo-condensation and conductive heat transfer become (Chen & Chiang 1984).

[3.29] $\phi_e = C_e(1.56Kn + 6.08\ Va)\ (e_s - e_a)$

[3.30] $\phi_c = C_c(Kn + 3.9\ Va)\ (T_w - T_a)$

In this study, the evapocondensation heat flux was calculated through the use of the Rimsha Donchenko equations, because the principal difference in the two approaches lies in the fact that the constant in the wind function was found by Rimsha and Donchenko to vary with $(T_w - T_a)$ (Dingman et al, 1967).

3.2 Ice Cover Equations

An ice covered river consists of a relatively stable ice slab with a certain ice thickness. The behaviour of the ice cover is characterised by the pattern at which it changes in thickness through melting and growing. This behaviour is attributed to the heat lost or gained to and from the atmosphere and the underside water body, across the ice-air and the water-ice interfaces. At the ice-air interface, the heat exchange occurs with the atmosphere, while at the water-ice interface, the heat exchange occurs with the river flow.

A snow cover over the ice slab is not included, however with the ice edge washed free of snow due to the wave action. Also, the ice slab is assumed to be well drained such that there is no surface water during thawing season.

The melting and thickening is evaluated at the top and bottom of the ice cover such that the one-dimensional heat equation governs the heat transfer across the ice cover, the temperature at the surface of the ice cover is calculated from the heat exchange components and meteorological conditions, and the temperature at the bottom surface of the ice cover is set to the freezing point temperature.

3.2.1 Top Surface Melting

The heat fluxes at the top surface of the ice cover are dependent on: the prevailing meteorological conditions, namely the air temperature, and wind velocity; the heat exchange components, basically the shortwave solar radiation, longwave radiation, evapocondensation heat flux, and conductive heat transfer; and the top surface ice cover which is evaluated by the heat transfer processes occurring at the ice-air interface.

$$[3.26] \quad K_i \frac{\partial T}{\partial z} + \Sigma \phi_i = 0$$

where

$$[3.27] \quad \Sigma\phi_i = \phi_s - \phi_{sp} - \phi_b - \phi_e - \phi_c$$

is the net heat flux at the ice-air interface which includes the net solar radiation (ϕ_s), the penetrating shortwave radiation (ϕ_{sp}), the longwave radiation (ϕ_b), the evapo-condensation heat flux (ϕ_e), and the conductive heat transfer (ϕ_c); K_i is the ice thermal conductivity; z is the distance across the ice cover; and ∂T is the difference between the freezing temperature imposed at the bottom surface of the ice cover and the temperature at the top surface of the cover. Therefore the change in temperature across the ice cover, between the two interfaces is linear and expressed as follows (Shen & Chiang 1984):

$$[3.28] \quad \frac{\partial T}{\partial z} = \frac{T_f - T_s}{\theta}$$

Where T_f is the freezing point temperature which is 0°C for fresh water, and T_s is the top surface temperature of the ice cover. Equations [3.27] is used to obtain the heat balance at this interface for the calculation of the top surface melting or growing. The top surface melting is computed only if the top surface temperature is calculated to be above 0°C, which is the melting point of ice. Under that condition, the ice cover top surface temperature is set to 0°C for the calculations. The heat balance equation is then used for the calculation of the melting or growing of the ice cover top surface which is expressed as follows:

$$[3.29]\quad \Sigma \phi_i + K_i \frac{T_f - T_s}{\theta} = -\rho_i L_i \frac{d\theta}{dt}$$

where $\Sigma\phi_i$ is the sum of the heat exchange components ϕ_b, ϕ_e, ϕ_c, ϕ_s, and ϕ_{sp}.

The heat exchange components represented in figure 3.1 are the net solar radiation (ϕ_S), the penetrating shortwave radiation (ϕ_{sp}), the longwave radiation (ϕ_b), the evapo-condensation heat flux (ϕ_e), and the conductive heat transfer (ϕ_c) respectively.

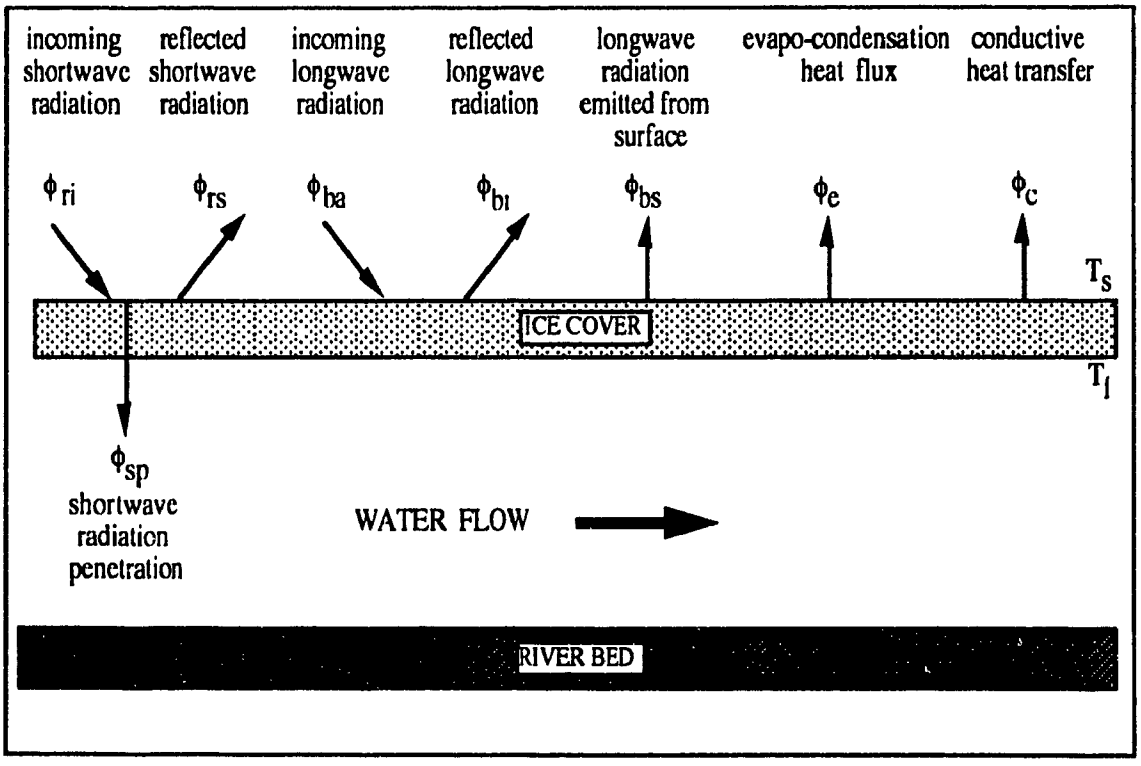

Figure 3.1: Heat transfer processes over an ice cover

3.2.2 Bottom Surface Melting

Melting at the bottom surface of the ice cover occurs due to the heat transfer from the water body to the ice cover. The turbulent heat transfer from the water to the ice cover depends on the heat transfer coefficient at the underside of the ice cover, the water temperature and the freezing point temperature at the underside of the ice cover. Figure 3.2 shows the heat tranfer processes occuring at the water-air interface for open water conditions and at the water-ice and ice-air interfaces for ice covered channels.

These heat exchange processes, in addition to the meteorological conditions, play important roles in determining the amount of heat the water body absorbs or emits and the amount of ice that forms or melts at the bottom of the ice cover. The melting and thickening at the bottom surface of the ice cover is governed by the energy balance at this surface and expressed as follows:

$$[3.30] \qquad \phi_i - \phi_{wi} = \rho_i L_i \frac{\Delta\theta}{\Delta t}$$

where

$$[3.31] \qquad \phi_i = K_i \frac{T_f - T_s}{\theta}$$

is the heat transfer across the ice cover, a function of the ice cover top surface temperature T_f, the freezing point temperature T_s, and the ice cover thickness θ.

$$[3.32] \qquad \phi_{wi} = h_{wi} (T_w - T_f)$$

is the heat flux from the water to the ice cover, in which

$$[3.33] \qquad h_{wi} = C_{wi} \frac{U^{0.8}}{D^{0.2}}$$

is a heat transfer coefficient; U is the average water velocity in m s^{-1}; D is the flow depth in m; ρ_i is the density of ice in Kg m^{-3}; L_i is the heat of fusion in j Kg^{-1}; T_w is the water temperature; and $\Delta\theta/\Delta t$ is the rate of change of the thickness of the ice. C_{wi} =1622 $Ws^{0.8}m^{-2.6}\,{}^{o}C^{-1}$ is a coefficient obtained from the closed conduit turbulent heat transfer correlations.(Ashton 1979)

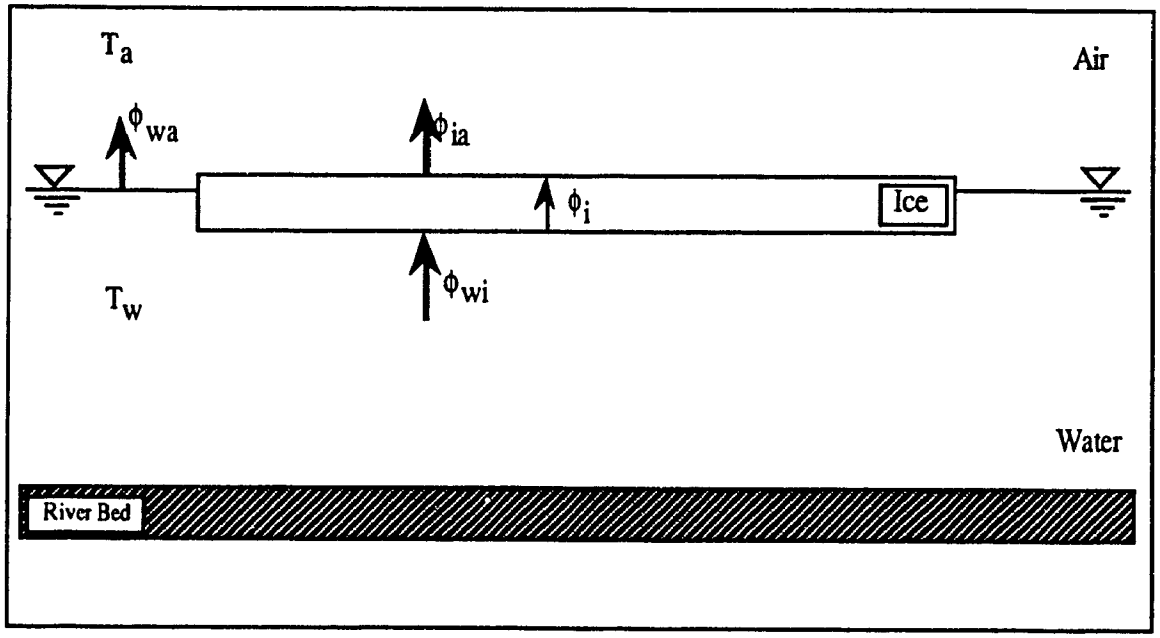

Figure 3.2. Heat flux at air-water, air-ice, and water-ice interfaces.

CHAPTER 4.0

NUMERICAL SCHEME

4.1 The MacCormack Scheme

The solution of the depth-averaged St. Venant equations is obtained by applying an explicit finite difference method based on the modified MacCormack time splitting scheme. The scheme is forward time, central space differencing, which involves the splitting of a two-dimensional calculation into a sequence of two one-dimensional operations such that, each operator is further split into a predictor-corrector sequence.

The two-dimensional finite difference operator, $L(\Delta t)$ is split into a sequence of one-dimensional operators as follows.

$$[4.1] \qquad L(\Delta t) = L_x(\Delta t_x)\, L_y(\Delta t_y)\, L_y(\Delta t_y)\, L_x(\Delta t_x)$$

where L_x and L_y are the one dimensional finite-difference operators and $\Delta t_x = \Delta t_y = 1/2\Delta t$ is the time increment. The L_x and L_y operators calculate the derivatives in the x and y directions respectively. Both, the x and y derivatives are then split into two half-time steps. Therefore, the solution at time $(n + 1)\,\Delta t$ for the cell coordinates (i, j) is obtained by applying the operator as follows:

$$[4.2] \qquad V_{i,j}^{n+1} = L_x(\Delta t_x) L_y(\Delta t_y) L_y(\Delta t_y) L_x(\Delta t_x) V_{i,j}^{n}$$

where $V_{i,j}^{n+1} = V(i\Delta x, j\Delta y, (n+1)\Delta t)$ is the new value calculated from $V_{i,j}^{n}$ values which are either initially known or have been previously calculated.

Consequently, each operator executes a combination of backward and forward differencing operations. Therefore, each operator, L_x and L_y, consist of a predictor which discretizes the space derivatives using the backward differences and a corrector which discretizes the space derivatives using the forward differences. As an example, consider $\partial u/\partial t$,

L_x operator

Predictor-backward differencing

$$[4.3] \quad \frac{u_{i,j}^{P_{n+1/2}} - u_{i,j}^{P_n}}{\Delta t_x} = -\left(\frac{E_{i,j} - E_{i-1,j}}{\Delta x}\right)$$

$$[4.4] \quad (u_{i,j}^{P_{n+1/2}})_B = u_{i,j}^{P_n} - \frac{\Delta t_x}{\Delta x}(E_{i,j} - E_{i-1,j})$$

corrector - forward differencing

$$[4.5] \quad \frac{u_{i,j}^{C_{n+1/2}} - u_{i,}^{C_n}}{\Delta t_x} = -\left(\frac{E_{i+i,j}^{P_n} - E_{i,j}^{P_n}}{\Delta x}\right)$$

$$[4.6] \quad \left(u_{i,j}^{C_{n+1/2}}\right)_F = u_{i,j}^{C_n} - \frac{\Delta t_x}{\Delta x}(E_{i+1,j}^{P_n} - E_{i,j}^{P_n})$$

L_y operator

Predictor-backward differencing

$$[4.7] \quad (u_{i,j}^{P_{n+1/2}})_B = u_{i,j}^{P_n} - \frac{\Delta t_y}{\Delta y}(F_{i,j} - F_{i,j-1})$$

corrector - forward differencing

$$[4.8] \quad (u_{i,j}^{C_{n+1/2}})_F = u_{i,j}^{C_n} - \frac{\Delta t_y}{\Delta y}(F_{i,j+1}^{P_n} - F_{i,j}^{P_n})$$

The superscript P signifies the values calculated at the predictor stage while the superscript C means that the values are obtained from the corrector stage. The subscript B and F imply backward and forward differencing respectively. The corrector sequence use the value of u obtained in the predictor step to calculate F(u).

In the L_x operator, the solution is advanced by a time step Δt_x, as if the derivatives in the y-direction were absent, and then in the L_y operator by a time step Δt_y, omitting the derivatives in the x-direction. Also, in both operators, backward differences are used for the predictor and forward differences for the corrector. (Garcia et al , 1986)

However, the sequence of operators should be performed in the following manners so that to eliminate any discontinuities (Garcia 1983):

First	L_x operator	Predictor:	backward differencing
		Corrector:	forward differencing
	L_y operator	Predictor:	backward differencing
		Corrector:	forward differencing
Second	L'_y operator	Predictor:	forward differencing
		Corrector:	backward differencing
	L'_x operator	Predictor:	forward differencing
		Corrector:	backward differencing

The step that follows the predictor-corrector sequence is the averaging of the value of $(u_{i,j})^{n+1/2}$ obtained from the previous two steps and located in the corrector sequence after the evaluation of $(u_{i,j})^{Cn+1/2}$.

$$[4.9] \qquad u_{i,j}^{n+1/2} = \frac{(u_{i,j}^{P_{n+1/2}})_B + (u_{i,j}^{C_{n+1/2}})_F}{2}$$

As a result, the decomposition of the partial differential equation is then re-termed into the following sequence (Garcia 1983):

$$[4.10] \quad [L_x\, L_y\, Ly'L_x']$$

This sequence is not a standard one. Many combinations of L_x and L_y can be and have been used before. An example is the treatment of compressible flow problems using the

[4.11] $$\left[L_x(\frac{\Delta t}{2}) \cdot L_y(\Delta t) \cdot L_x(\frac{\Delta t}{2}) \right]$$

sequences.

It is obvious that with this sequence there exists a critical factor called "preferred direction" in which the order of operator sequence used can affect the final solution. For example $[L_X L_Y L_X]$ and $[L_Y L_X L_Y]$ were found to give slightly different results for the same problem.

On the other hand, the sequence $[L_X L_Y L'_Y L'_X]$ eliminates the "preferred direction" concept and provides symmetrical solutions which in turn allows for second order accuracy in space and time (Garcia 1983).

The stability of the finite difference scheme is very important. The stability conditions are determined by the Courent-Freidrich-Levy criterion which states that the maximum time step that can be used in the standard MacCormack scheme is the ***minimum*** value of the following two terms:

[4.12] $$\Delta t \le \frac{\Delta x}{u + \sqrt{gh}}$$

or

$$\Delta t \le \frac{\Delta y}{v + \sqrt{gh}}$$

4.2 Discretization of The MacCormack Scheme

To show the discretized form of the continuity and momentum equations using the MacCormack scheme, consider the continuity, x-momentum, y-momentum equations.

Lx operator: calculation of derivatives in the x-direction.

- continuity

$$[4.13] \quad \frac{\partial h}{\partial t} + \frac{\partial uh}{\partial x} = 0$$

- momentum x-direction

$$[4.14] \quad \frac{\partial uh}{\partial t} + \frac{\partial}{\partial x} u^2 h = \frac{\partial}{\partial x} \left(\frac{\tau_{xx}}{\rho} \right) - gh \frac{\partial}{\partial x} (H + 0.9\theta) - \frac{\tau_{bx}}{\rho}$$

- momentum y-direction

$$[4.15] \quad \frac{\partial vh}{\partial t} + \frac{\partial uvh}{\partial x} = \frac{\partial}{\partial x} \left(\frac{\tau_{yx}}{\rho} \right)$$

Discretization of the Lx operator:

Predictor Sequence : Backward Difference

$$[4.16] \quad H^{P}_{i,j} = H^{o}_{i,j} - \frac{\Delta t_x}{\Delta x}\left(u^{o}_{i,j}\, h^{o}_{i,j} - u^{o}_{i-1,j}\, h^{o}_{i-1,j}\right)$$

$$[4.17] \quad U^{P}_{i,j} = U^{o}_{i,j} - \frac{\Delta t_x}{\Delta x}\left(u^{o^2}_{i,j}\, h^{o}_{i,j} - u^{o^2}_{i-1,j}\, h^{o}_{i-1,j}\right) +$$

$$\frac{\Delta t_x}{\Delta x}\left[\frac{\tau_{xx}}{\rho}\Big|_{i,j} - \frac{\tau_{xx}}{\rho}\Big|_{i-1,j}\right] - gh\,\frac{\Delta t_x}{\Delta x}\left[(H^{o}_{i,j} + 0.9\theta_{i,j}) - (H^{o}_{i-1,j} + 0.9\theta_{i,j})\right] -$$

$$\Delta t_x\left(\frac{\tau_{bx}}{\rho}\Big|_{i,j}\right)$$

$$[4.18] \quad V^{P}_{i,j} = v^{o}_{i,j}\, h^{o}_{i,j} - \frac{\Delta t_x}{\Delta_x}\left(u^{o}_{i,j}\, v^{o}_{i,j}\, h^{o}_{i,j} - u^{o}_{i-1,j}\, v^{o}_{i-1,j}\, h^{o}_{i-1,j}\right)$$

$$+ \frac{\Delta t_x}{\Delta_x}\left(\frac{\tau_{yx}}{\rho}\Big|_{i,j} - \frac{\tau_{yx}}{\rho}\Big|_{i-1,j}\right)$$

Corrector Sequence Forward Differences :

$$[4.19] \quad H^{c}_{i,j} = H^{p}_{i,j} - \frac{\Delta tx}{\Delta x}\left(u^{p}_{i+1,j} h^{p}_{i+1,j} - u^{p}_{i,j}\quad H^{p}_{i,j}\right)$$

$$[4.20] \quad U^{c}_{i,j} = U^{p}_{i,j} - \frac{\Delta t_x}{\Delta x}\left(u^{p^2}_{i+1,j}\, h^{p}_{i+1,j} - u^{p^2}_{i,j}\, H^{p}_{i,j}\right) +$$

$$\frac{\Delta t_x}{\Delta x}\left[\frac{\tau_{xx}}{\rho}\Big|_{i+1,j} - \frac{\tau_{xx}}{\rho}\Big|_{i,j}\right] - gh\,\frac{\Delta t_x}{\Delta x}\left[(H^{p}_{i+1,j} + 0.9\theta_{i+1,j}) - (H^{p}_{i,j} + 0.9\theta_{i,j})\right] -$$

$$\Delta t_x\left(\frac{\tau_{bx}}{\rho}\Big|_{i,j}\right)$$

$$[4.21] \quad V^c_{i,j} = v^p_{i,j}\ h^p_{i,j} - \frac{\Delta t_x}{\Delta_x}\left(u^p_{i+1,j}\ v^p_{i+1,j}\ h^p_{i+1,j} - u^p_{i,j}\ v^p_{i,j}\ h^p_{i,j}\right)$$

$$+ \frac{\Delta t_x}{\Delta_x}\left(\frac{\tau_{yx}}{\rho}\Big|_{i+1,j} - \frac{\tau_{yx}}{\rho}\Big|_{i,j}\right)$$

and therefore,

$$[4.22] \quad H^1_{i,j} = \frac{1}{2}\left(H^C_{i,j} + H^P_{i,j}\right)$$

<u>L_y operator: calculation of derivatives in the y-direction.</u>

- continuity

$$[4.23] \quad \frac{\partial h}{\partial t} + \frac{\partial v h}{\partial y} = 0$$

- momentum x-direction

$$[4.24] \quad \frac{\partial uh}{\partial t} + \frac{\partial}{\partial y} u v h = \frac{\partial}{\partial y}\left(\frac{\tau_{xy}}{\rho}\right)$$

- momentum y-direction

$$[4.25] \quad \frac{\partial vh}{\partial t} + \frac{\partial}{\partial y} v^2 h = \frac{\partial}{\partial y}\left(\frac{\tau_{yy}}{\rho}\right) - gh\frac{\partial}{\partial y}(H + 0.9\theta) - \frac{\tau_{by}}{\rho}$$

Discretization of L_y operator :

Predictor Sequence : Backward Difference

$$[4.26] \quad H^{P}_{i,j} = H^{o}_{i,j} - \frac{\Delta t_y}{\Delta y}\left(v^{o}_{i,j}\, h^{o}_{i,j} - v^{o}_{i,j-1}\, h^{o}_{i,j-1}\right)$$

$$[4.27] \quad V^{P}_{i,j} = V^{o}_{i,j} - \frac{\Delta t_y}{\Delta y}\left(v^{o^2}_{i,j}\, h^{o}_{i,j} - v^{o^2}_{i,j-1}\, h^{o}_{i,j-1}\right) +$$

$$\frac{\Delta t_y}{\Delta y}\left[\frac{\tau_{yy}}{\rho}\Big|_{i,j} - \frac{\tau_{yy}}{\rho}\Big|_{i,j-1}\right] - gh\,\frac{\Delta t_y}{\Delta y}\left[(H^{o}_{i,j} + 0.9\theta_{i,j}) - (H^{o}_{i,j-1} + 0.9\theta_{i,j-1})\right] -$$

$$\Delta t_y\left(\frac{\tau_{by}}{\rho}\Big|_{i,j}\right)$$

$$[4.28] \quad U^{P}_{i,j} = u^{o}_{i,j}\, h^{o}_{i,j} - \frac{\Delta t_y}{\Delta_y}\left(u^{o}_{i,j}\, v^{o}_{i,j}\, h^{o}_{i,j} - u^{o}_{i,j-1}\, v^{o}_{i,j-1}\, h^{o}_{i,j-1}\right)$$

$$+ \frac{\Delta t_y}{\Delta_y}\left(\frac{\tau_{xy}}{\rho}\Big|_{i,j} - \frac{\tau_{xy}}{\rho}\Big|_{i,j-1}\right)$$

Corrector Sequence : Forward Difference

$$[4.29] \quad H^{c}_{i,j} = H^{p}_{i,j} - \frac{\Delta t_y}{\Delta y}\left(v^{p}_{i,j+1}\, h^{p}_{i,j+1} - u^{p}_{i,j} h^{p}_{i,j}\right)$$

$$[4.30] \quad V^{c}_{i,j} = V^{p}_{i,j} - \frac{\Delta t_y}{\Delta y}\left(u^{p^2}_{i,j+1}\, h^{p}_{i,j+1} - u^{p^2}_{i,j}\, h^{p}_{i,j}\right) +$$

$$\frac{\Delta t_y}{\Delta y}\left[\frac{\tau_{yy}}{\rho}\Big|_{i,j+1} - \frac{\tau_{yy}}{\rho}\Big|_{i,j}\right] - gh\,\frac{\Delta t_y}{\Delta y}\left[(H^{p}_{i,j+1} + 0.9\theta_{i,j+1}) - (H^{p}_{i,j} + 0.9\theta_{i,j})\right] -$$

$$\Delta t_y\left(\frac{\tau_{by}}{\rho}\Big|_{i,j}\right)$$

$$[4.31]\quad U^{c}_{i,j} = u^{p}_{i,j}\, h^{p}_{i,j} - \frac{\Delta t_x}{\Delta_x}\left(u^{p}_{i,j+1}\, v^{p}_{i,j+1}\, h^{p}_{i,j+1} - u^{p}_{i,j}\, v^{p}_{i,j}\, h^{p}_{i,j}\right)$$

$$+ \frac{\Delta t_y}{\Delta_y}\left(\frac{\tau_{xy}}{\rho}\Big|_{i,j+1} - \frac{\tau_{xy}}{\rho}\Big|_{i,j}\right)$$

4.3 The Upwind Scheme

The upwind scheme is a numerical procedure that is applied to the transport of species equation, in which it takes into account the difficulties encountered by the use of other schemes such as the central-differencing scheme and the hybrid scheme. Some of the difficulties encountered in the other schemes is unrealistic results due to the instability of the scheme used under specific cases and the introduction of numerical round off errors in the discritization of the equation.

The upwind-difference scheme is used as a remedy to the difficulties and weaknesses found in the formulation of the other numerical schemes. Instead of assuming that the convected property ϕ_e at the interface is the average of ϕ_E and ϕ_P as shown in figure 4.1, the upwind scheme states a different approach. The scheme used for the solution of the diffusion terms in the transport equations is left unchanged, however the value of the convective property assumes the value of the same property of the grid point on the upwind side of the face as follows (Patankar 1980):

$$\phi_e = \phi_P \quad \text{if} \quad U_e > 0$$

$$\phi_e = \phi_E \quad \text{if} \quad U_e < 0$$

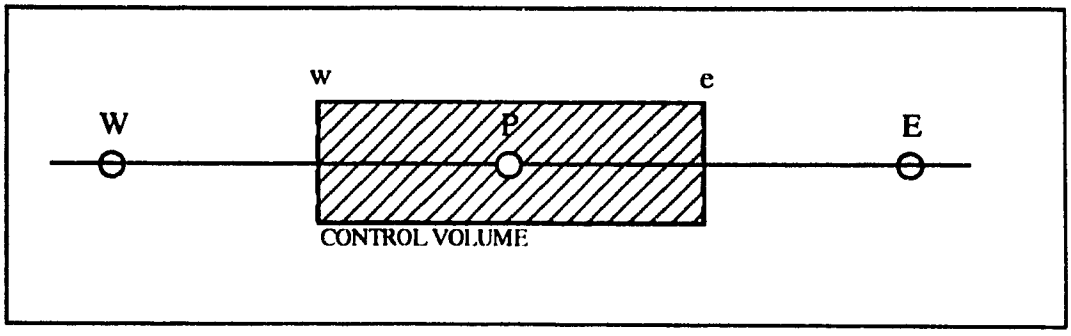

Figure 4.1. Typical Control Volume Grid Cluster. (Patankar 1980)

Therefore, in the present study, the scheme used for the solution of the diffusion terms in the temperature, k, and ε equations is left unchanged, however the solution to the convective terms is obtained through the use of the upwind scheme, such that the value of the temperature, turbulent kinetic energy, and the rate of its dissipation assume the value of the same property of the grid point on the upwind side of the face.

The use of the upwind scheme may be visuallized by a set of stirred tanks connected in series by tubes, know as the "tank-and-tube" model. This scheme serves to represent the finite difference cells used in the computational mesh. Heat is transferred from the upstream tank to the next downstream tank through the tubes (convection) and the tank walls (diffusion). Fluid flowing from one tank to the next is at the temperature that prevails in the tank on the upstream side. The fluid in the tube carries the flow characteristics of the tank from which it has come.

In computational terms, the value of the temperature at an interface is equal to the value of the temperature at the grid point on the upwind side of the face. Therefore, the use of a central difference scheme is therefore appropriate for the dispersion term (Patankar 1980). Also, the use of upwind scheme for the calculation of the temperature field is acceptable when near steady conditions are dominant and no strong cross flow gradients are present. Therefore, with little variation in the flow velocity and negligible cross flow gradients, the use of an upwind scheme can be justified (Raithby 1976).

CHAPTER 5.0

BOUNDARY CONDITIONS

In Chapter 2.0 a closed set of equations are presented, such that with known values for the empirical constants and computed value for the source terms, these equations can be solved for u, v, k, ε, h, T, ν_t, and θ. However, boundary conditions for the above mentioned parameters should be specified at solid surfaces, inlets and exits of the channel.

At inflow boundaries, a transversal velocity distribution, and a constant temperature is imposed. At outflow boundaries, the water depth is imposed, taking into account for the case where an ice cover is present, and if so, the decrease and increase in the water depth due to the changes of the ice cover thickness. At solid boundaries, u, v, k, ε, h, T, and ν_t should be specified, however special attention is required due to the nature of the problem that is involved.

The specification of the boundary conditions at solid surfaces such as the river banks, require the specification of fictitious points outside of the computational grid system, as shown in figure 5.1. The normal gradient of the velocity parallel to the solid wall U is set to zero, and the velocity V normal to the wall is set equal to the magnetude of the velocity of the inside cell, but opposite in direction, as shown in figure 5.2.

The temperature gradients are also zero since negligible heat transfer through the wall is assumed in most hydraulic problems. The walls are assumed to be adiabatic walls, where the heat and concentration flux are taken as zero. Therefore, the temperature at the fictitious cell outside of the flow domain is set equal to the temperature of the inside cell.

Similarly, the normal gradient of the water level, ice cover thickness, bottom elevation and hydraulic radius across the solid surfaces were set to zero.

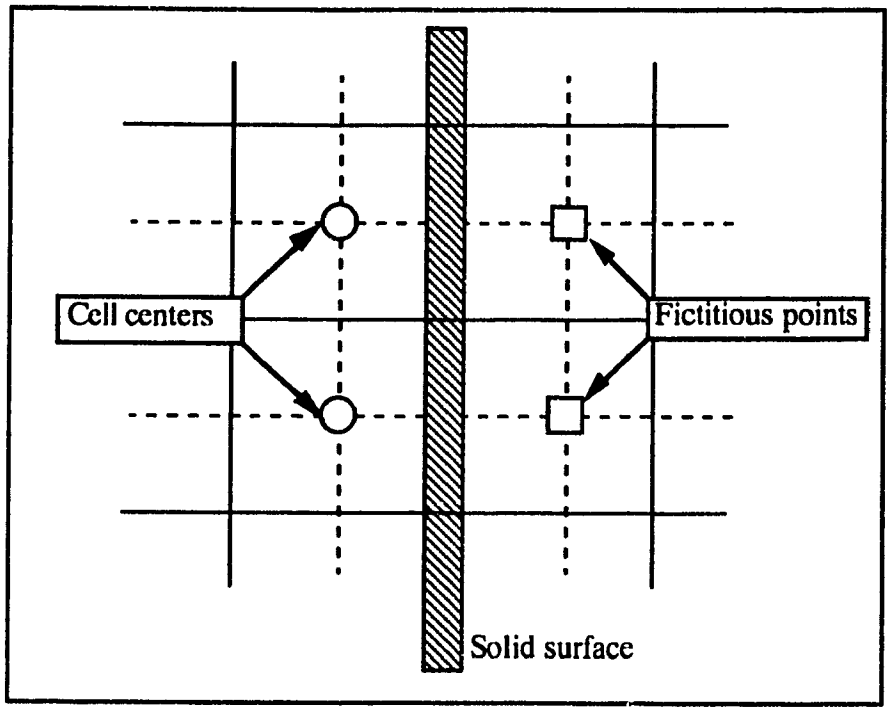

Figure 5.1: External fictitious points

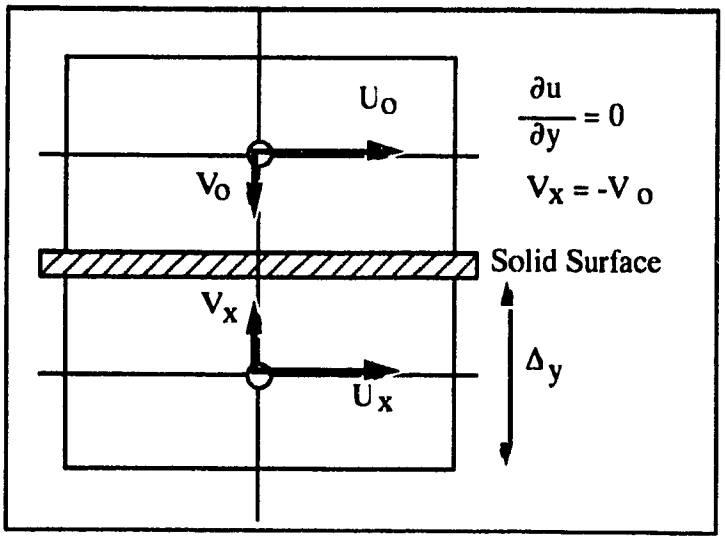

Figure 5.2: Solid Wall Boundary Conditions.

The boundary conditions at solid surfaces for k, ε, and ν_t used in the present calculations are a modified version of those used by Rastogi and Rodi 1978. Therfore, in this chapter, the derivation of the boundary conditions at solid surfaces for k, ε, and ν_t is presented.

At a solid boundary the calculation of k, ε, and ν_t for the cell nearest to the wall require special attention, since the dissipation rate of the turbulent kinetic energy ε at the solid surface is finite, in contrast to the zero mean and fluctuating velocities.Therefore, to determine the value of ε for the cell nearest to the wall requires the integration of the equations through the viscous sublayer. For practical purposes, this is undesirable since steep gradients and viscous effects present in the viscous sublayer, require the use of a very fine grid in the near-wall region to be able to obtain reasonable resolution. Therefore, the cost of computer time increases drastically, and this approach becomes impractical. However, empirical laws of acceptable generality can be used to describe k, ε, and ν_t for the cells nearest to solid boundaries and the integration over the viscous sublayer becomes unnecessary.

Near a solid wall, the flow is greatly affected by the kinematic viscosity. The region in the vicinity of a solid wall where the viscous effects cannot be neglected, is thin relative to the size of the turbulent flow field. Satisfying the correct boundary conditions at solid surface is practically impossible. Therefore, a reasonable approach for the treatment of boundary conditions for a computational cell nearest to a solid surface originates from the concept of relating the flow behaviour in the near-wall region with the local mean flow parameters.

In regions close to solid walls, the Reynolds number is very small, and viscous effects are predominant. Therefore for the flow in the near-wall region it is assumed that (Rodi 1980)

1. convection and diffusion are negligible
2. the turbulence energy production and the kinetic energy dissipation rate are in local equilibrium
3. the turbulent shear stress is nearly constant and equal to the wall shear stress.
4. the law of the wall applies.

Under these conditions, k, and ε in the near-wall region can be derived. Consider for example, the two points W and P shown in figure 5.3. W is the point at the solid surface and P is the point at a distance y_w from the wall. The longitudinal velocity component near a solid boundary obeys the universal law of the wall described as follows (Chapman 1982):

$$[5.1] \quad \frac{U}{U_*} = \frac{1}{\kappa} \ln \frac{\Delta y/2}{Z_0}$$

where U is the velocity component parallel to the wall; U_* is the resultant friction velocity; κ is the von karman constant; $\Delta y/2$ is half the grid spacing; and Z_0 is the channel roughness height.

Rearranging the terms, an expression describing the resultant friction velocity can be obtained

$$[5.2] \qquad U_* = \frac{\kappa\ U}{\ln \frac{\Delta y/2}{Z_0}}$$

Differentiating Eq. 5.1 with respect to y gives:

$$[5.3] \qquad \frac{\partial U}{\partial y} = \frac{U_*}{\kappa\, y_w}$$

where y_w is the distance from the wall to the center of the nearest cell (half the grid spacing).

From the assumption that energy production is in balance with energy dissipation rate, and convection and diffusion is negligible in the near-wall region, therefore,

$$[5.4] \qquad \varepsilon = \nu_t \left(\frac{\partial U}{\partial y} \right)^2$$

substituting Eqs. 2.22 and 5.3 into Eq. 5.4 yields

$$[5.5] \qquad \varepsilon = \frac{C_\mu^{1/2} k\ U_*}{\kappa\, y_w}$$

Using Eq. 2.16, and substituting for ν_t and $\partial u/\partial y$, the following expression is obtained:

$$[5.6] \qquad \frac{\tau}{\rho} = C_\mu^{1/2} k$$

by definition

$$[5.7] \qquad \frac{\tau}{\rho} = U_*^2$$

therefore

$$[5.8] \qquad U_* = C_\mu^{1/4} k^{1/2}$$

and

$$[5.9] \qquad \left(\frac{\tau}{\rho}\right)_w = \frac{U_* \kappa U_w}{\left[\ln \frac{y_w}{Z_0}\right]^2}$$

substituting equation [5.2] into equation [5.9] and solving for k, the value for k_w in the near-wall region can be expressed as follows:

$$[5.10] \qquad k_w = \frac{\kappa^2 U^2}{\left[\ln \frac{y_w}{Z_0}\right]^2 C_\mu^{1/2}}$$

also from equation [5.5] substituting for U_*, the boundary value for ε_w in the near-wall region can be determined

$$[5.11] \qquad \varepsilon_w = \frac{U_*^3}{\kappa y_w}$$

In the present work, the turbulent kinetic energy k_w at the cell nearest to the wall is calculated from its corressponding k-transport equation, however with the expression given in Eq.5.12 to be used for the ε term. Eq. 5.12 represents the finite value of the dissipation rate of k at a solid surface. The velocity component U is computed from the momentum equation, however using the derived wall shear stress expression, Eq.5.9. The dissipation rate of the turbulent kinetic energy k is evaluated from Eq.5.5.

$$[5.12] \qquad \varepsilon = \frac{U_*^3}{\kappa y_w} \ln (\Delta y / Z_o)$$

Modification to the ε-term in the k-equation is to account for the large increase in dissipation rate in the near-wall region. The grid system used involves the alignement of the cell faces rather than the cell centers along the solid boundaries.

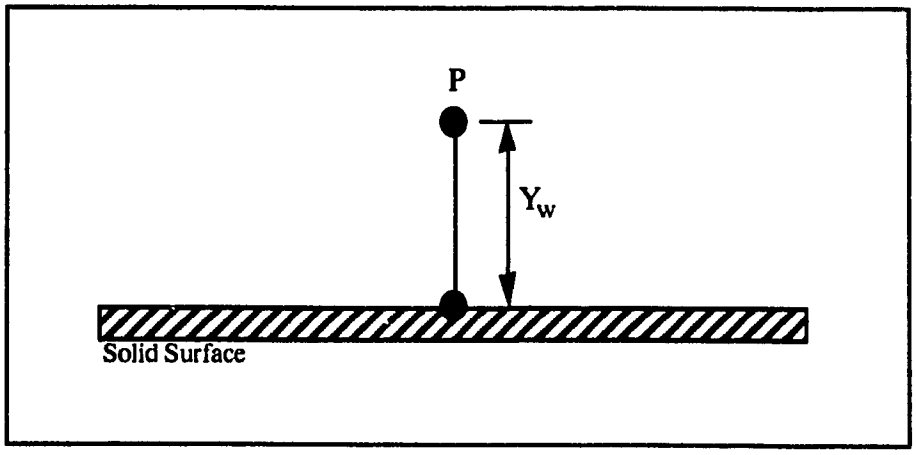

Figure 5.3: A Point Close to a Solid Surface(Launder and Spalding 1974)

Following the definition of the boundary conditions specifications, initial conditions should be imposed for U, V, k, ε, h, T, ν_t, and θ. The water velocity components are set equal to the mean flow velocity components over the whole flow domain. The inflow velocities are increased in a stepwise fashion untill their corressponding steady state value is attained. The water surface elevation is initialized at a specified close to bottom slope. Temperature at all points in the flow domain is set equal to the inlet temperature of the channel. The ice cover thickness is set to the average prevailing local thickness present over the reach for the computational mesh points that lie in that same reach, such that for certain cases, if data is available, the ice cover could vary in thicknesses.

CHAPTER 6.0

COMPUTATIONS RESULTS AND DISCUSSION

In order to predict ice cover melting characteristics a function of the hydrodynamics, hydrothermal, and meteorological conditions, it is necessary to solve the governing equations, and consequently the ice cover formulations. The numerical model used in this study solves for the above mentioned conditions and evaluates the ice cover melting pattern. The solution procedure and assumptions adopted in the formulation of the numerical model are tested against previous similar work, laboratory experiments, and a field case study.

Five sets of tests have been performed using the k-ε turbulence model, for the investigation of the melting of an ice cover under variable meteorological and water temperature conditions. The first set of tests is performed to verify the authenticity of the simulation under open channel conditions and a comparison with previous modelling works done by McGuirk and Rodi 1977, as well as with experimental investigations done by Carter 1969, and other by Michael 1975, is carried out.

The second set of tests shows the effects of hydrodynamic and thermal conditions on ice cover melting using a k-ε model and accompanied with a constant viscosity model. The third set of tests presents a series of results showing the variation in the melting pattern of an ice cover caused by varying meteorological and hydrodynamic conditions. The fourth set of tests is concerned with the reproduction of three experiments performed by Hewlett, 1976, and other three experiments by Marco, A.R. Gallardo, 1974. The final set of tests include a simulation of a real life situation with comparison to collected field data.

6.1 Model Verification

Ice Free Conditions

The accurate prediction of the hydrodynamic conditions is essential for the simulation of ice cover melting, since the hydrothermal characteristics of the flow regime is governed by it. Therefore, in this set of tests, the performance of the model in evaluating the hydrodynamic and hydrothermal characteristics of open channel flow under various inflow conditions is investigated.

The configuration of a side discharge over the full water depth was used. Figure 6.1.1 shows the channel configuration used for this set of computation tests. The channel has a flat bed with a Manning roughness coefficient of 0.03, and a water depth of 5.0 meters. The side-discharge is imposed in the near bank. A side-discharge to channel width ratio is b/B of 0.10. The flow field is fitted with a rectangular uniform grid of 120 X 20 cells. The cell size is taken as 2.5 m by 2.5 m. The time step is set according to the CFL stability criterion and taken as 0.05 seconds.When the ice cover is imposed, the initial ice thickness was set to 0.1 meters with a Manning roughness of 0.02 at the underside of the ice cover.

Verification of Hydrodynamic and Hydrothermal Computations

The side discharge being at right angles to the mean channel flow direction, is deflected by the channel cross flow, thus forcing the main flow to bend towards the far bank. A recirculation region with a low pressure and a decreased surface elevation develops just downstream of the jet. The parameters that influence the flow regime are:

the discharge to channel width ratio (b/B); discharge to main channel velocity ratio (R); and the channel bottom roughness. Buoyancy effects are considered negligible and only the longitudinal and transversal variations are considered.

Hydrodynamic computations were performed for different side-discharge to main channel flow velocity, in order to investigate the behaviour of the flow pattern, jet trajectories of the warm water discharge, dilution of the warm water along the jet trajectory, and reattachment length.

Fig. 6.1.2 shows the effect of the side-discharge on the main flow of the channel, where three regions can be identified. In the region upstream of the outfall, the water surface level rises, due to the blockage effect of the side-discharge inflow. In the downstream region, the disturbance of the flow field by the side effluent can still be felt, owing to the prevailing low pressure in the recirculation region below the outfall, where the maximum change in surface elevation occurs. This low pressure in the recirculation region provokes the bending and reattachment of the side-discharge. The performance of the present model compares favourably with previous works done involving the use of the k-ε model.

The computed jet trajectories of warm water discharges shown in Fig. 6.1.3, 6.1.4, and 6.1.5, are compared with predictions obtained by McGuirk and Rodi (1978) for three velocity ratios R (= V_d / U_r) of 2, 5 and 10 respectively, where V_d is the velocity of the side-discharge and U_r is the main channel flow velocity. A jet trajectory is defined as the locus of maximum jet temperature represented by the path it follows downstream and, identified by its location from the near bank. The calculated jet trajectory agree with that obtained by McGuirk and Rodi for all three velocity ratios,

as shown in figures 6.1.3 to 6.1.5. The present model calculations are slightly overpredicted for R=2 and R=5, and underpredicted for R=10, however, in good agreement with the experimental data, for all velocity ratios. The change in magnetude of the jet trajectories with respect to the velocity ratio decreases, while the change in the computed jet trajectory with respect to R for the values obtained by McGuirk and Rodi remain constant.

When results from both, present and McGuirks model, are compared to experimental data performed by Carter 1969, the present results show better agreement for velocity ratio equal to 2 and 5, as shown in fig.6.1.3 and 6.1.4 respectively. McGuirks prediction at the jet trajectories are underestimated for R=2 and 5. However, at a high velocity ratio (R=10), the present model underestimate the jet trajectory, while McGuirks model overestimate the jet trajectory. The reason can be attributed to the possible effect of the far bank wall which might not be far enough.The discrepancy in the results can be related to the fact that Carter has used low densimetric Froude number (defined as $V_d / [gh (\rho_r - \rho_d) / \rho_r]^{1/2}$), thus resulting in some buoyancy effects in the experiments which the present and McGuirk and Rodis model cannot account for. Consequently, stratification might render temperature measurements which may not be truly representative of the depth-averaged temperature predicted by the model. (McGuirk and Rodi 1978)

In McGuirk and Rodi 1978, the increased jet trajectory penetration was attributed to the effects of buoyancy. The latter tends to make the warm water surface layer spread further away from the outfall due to buoyancy-induced pressure gradients at which would be the strongest at low froude numbers. Turbulence production is thus expected to increase mixing and loss of momentum would result. Figs. 6.1.3 and 6.1.4

show slightly overestimated jet trajectories, while Fig. 6.1.5 reveals the effect of the increased turbulence caused by buoyancy on the estimation of the present jet trajectory. Keeping in mind the previous discussions, comparisons between the predicted and measured data are of acceptable agreement. However, the model correctly predicted the increase in jet penetration with increasing velocity ratio, and the location of the reattachment of the maximum temperature line to the near bank.

Figs. 6.1.6, and 6.1.7 present the computed isotherms for the velocity ratio cases R=2, and 10 respectively, compared to the experimental findings of Carter (1969), and McGuirk and Rodis' numerical predictions. The general behaviour of the isotherm pattern is analysed. At low velocity ratio, the warm water is carried far downstream of the channel close to the near bank. However, at high velocity ratio, the warm water is diluted much faster, and lower temperatures are observed downstream. Therefore, the general behaviour of the isotherms and the extent of thermal dispersion are predicted correctly in both transversal and longitudinal directions.

The dilution of warm water along the jet trajectory, described as the ratio of the maximum temperature excess over the river temperature (T_{CL} - T_c) and discharge temperature excess over the river temperature (T_d - T_c), is compared in Figs. 6.1.8, 6.1.9 and 6.1.10 for velocity ratios 2, 5, and 10 respectively. These figures represent the dilution of the warm water measured along the jet trajectory. Comparisons with other k-ε work performed by McGuirk and Rodi, is shown in figure 6.1.8 for a low velocity ratio, R=2. Figs. 6.1.8 and 6.1.9 show that with an increase of velocity ratio less dilution is predicted in the present model compared to McGuirk and Rodi's investigations. A maximum difference of 30% is observed. Figs. 6.1.8 to 6.1.10 show that an increase in velocity ratio results in a reduction of predicted dilution along the

centre-line trajectory. Present computations indicate that the rate of dilution decreases with the velocity ratio, contrary to the findings of McGuirk and Rodi 1978, where their predictions indicate an increase in the rate of dilution with an increase of velocity ratio at least in the far downstream region.

Although previous work indicate little influence of velocity ratio on the dilution, the present study shows otherwise. An increase in velocity ratio results in an increase in turbulent kinetic energy thus increasing the turbulent production and consequently the mixing. Therefore, if smaller temperature gradients are present, less dilution will result. The influence of the velocity ratio on dilution varies approximately 27% between R=2 and R=5 and 8% between R=5 and R=10. Consequently, as the velocity ratio increases, the change in the dilution decreases.

The reattachment length calculated by the present model compares well with McGuirk and Rodis' 1978 predictions as shown in figure 6.1.11. The calculated values are slightly higher than the values obtained by McGuirk and Rodi, such that a 5% difference exists at a low velocity ratio R=2. The difference increases gradually to 26% with an increase in the velocity ratio to R=10. Fig. 6.1.11 also shows the results obtained by Mickail et al 1975. Both, present, and McGuirks and Rodis' calculations underestimate the eddy length, with the present calculations showing better agreement with the experimental results.

Comparison of Computations With Another Model

The effects of the hydrodynamic and hydrothermal conditions, computed by the numerical model used in this work, on the melting characteristics of an ice cover,

are evaluated by comparing the model with another constant viscosity model. An analysis of centre-line trajectories obtained from the constant viscosity model indicate 45% less jet penetration into the channel , as shown in Figs. 6.1.12, 6.1.13, and 6.1.14. The largest difference between the two models in the penetration of the jet trajectory occurs at the level of the side discharge and is reduced along the downstream direction until a distance x/R = 16, where both model predictions agree to less than one percent difference. A further jet penetration into the channel, as given by the k-ε turbulence model implies a larger ice free opening in the transversal direction.

Isotherm patterns for velocity ratio R=2, is shown in figs. 6.1.15, and 6.1.16 for the eddy viscosity and constant viscosity models, respectively. Two regions are identified where the isotherms pattern is different. In the near field region, higher temperatures are injected in the transversal direction, and in the far field region, more mixing is computed, by the k-ε model. Also, More dispersion is predicted by the present k-ε model, in the downstream direction. This increase in dispersion and in the heat entrainment causes an increase in the near field open water width and in the transversal ice free opening in the downstream direction.

The dilution along the centre-line trajectory is compared in Figs. 6.1.17, 6.1.18 and 6.1.19 with the constant viscosity model, for velocity ratio R=2,5 and 10 respectively. Less dilution is predicted by the constant viscosity model. Quarter way downstream of the outfall, the dilution reaches a constant value which is attained for the remaining part of the channel. On the other hand, the dilution calculated by the k-ε model is larger by about 53% for R=2 and 27% for R=5. Therefore, more melting is expected to occur with the k-ε model as compared to a constant viscosity model. The difference in the computed dilution along the centre-line trajectory between the two

models is significantly influenced by the velocity ratio R, such that the difference decreases with increasing R.

The reattachment length is compared with the results obtained from the constant viscosity model in fig. 6.1.20. The results are obtained for three velocity ratio cases with a constant outfall to main cha nel width ratio b/B=0.1. Fig. 6.1.20 shows that the constant viscosity model predicts smaller eddy sizes by about 43%, and at low velocity ratios there is practically no recirculation predicted in the downstream side of the outfall. This underprediction of the recirculation length by the constant viscosity model, decreases the temperature mixing extent in the transversal direction, thereby reducing the extent of the ice cover melting.

Simulation tests using different values for the turbulent viscosity coefficient in the hydrodynamic equations found in the constant viscosity model, were performed. Doubling the value of the turbulent viscosity coefficient, under same conditions, caused only a slight effect on the melting of the ice cover(Plouffe 1987). However, the turbulent viscosity calculated from the k-ε model was 100 to 3,000,000 times larger than the laminar viscosity ν, depending on the velocity ratio and the position in the flow domain. This certainly accentuates the melting of an ice cover. McGuirk and Rodi 1977, carried out a few runs in which a uniform ν_t over the whole flow domain was assumed to be 200 times the laminar kinematic viscosity ν. The constant value of the turbulent viscosity ν_t gave very poor agreement with the experimental hydrodynamic parameters, for low moment flux ratios, R^2 b/B. This indicated that constant turbulent viscosity is too crude an assumption to use in a general model for the near field of side discharges.

Investigation of Ice Cover Melting Under Turbulent Flow Conditions

The model has also been tested for a number of different hydrodynamic situations under ice covered conditions, to illustrate the behaviour of the melting pattern of an ice cover and the width of the near field ice free zone. Various thermal effluent characteristics, combinations of side-discharge temperatures, side-discharge to main flow velocity ratios R, and air temperatures were employed in these tests. Flow characteristics and ice cover melting pattern were simulated and compared for the cases of constant viscocity and k-ε eddy-viscosity models. For ice covered flow, the k-ε model parameters were adopted after an open channel heat dispersion model. In all cases, similar initial conditions are assumed and the main channel flow rate was maintained constant throughout the calculations.

Results obtained from a series of tests performed on a rectangular channel, and adopted after McGuirk and Rodi 1978 are presented. These results illustrate the behaviour of the melting pattern of an ice cover under combinations of different meteorological conditions. These combinations were selected by holding two variables constant while varying the third. An example test run could be holding a velocity ratio R=2, an effluent temperature of 5°C and varying the air temperature from -20°C, to -5°C. In this series of tests, the results were obtained by using the hydrodynamic equations to establish the steady-state flow field. The k-ε model used to calculate the turbulent shear stresses was then introduced.

Results of hydrodynamic computations indicated an increase in the flow depth of the channel, in regions of ice melting. This increase in flow depth was roughly equal to 92% of the decrease in ice cover thickness. A slight reduction in the ice cover

thickness occurs upstream of the point of discharge. At the far bank, the ice cover increases in thickness of about 10% of its original value. An increasing effluent temperature or air temperature results in a wider opening in the ice cover. The temperature gradient in the longitudinal direction is less than the temperature gradient in the transverse direction, thereby implying a smaller rate of ice cover melting in the longitudinal direction. Such a temperature distribution can describe the behaviour of the melting of an ice cover due to a thermal discharge, such that the ice cover will melt first in the transversal direction therefore creating a leading edge, then progress in the downstream direction.

The incorporation of a k-ε turbulence model, leads to a change in the temperature distribution computed over the flow domain. Due to the turbulent diffusion and the propagation of the side-discharge in the main channel, the water temperature increased over a short distance upstream of the side-discharge along the near-wall.

The increase in velocity ratio caused an increase in the length of the transversal ice free reach as shown in Fig. 6.1.21. A non-linear relationship was found to exist between the width of the ice free reach and the velocity ratio (R). Fig. 6.1.22 presents the ice free width at steady state conditions for R=2,5,10 at air temperature of -20°C. For an increase in velocity ratio, the ice edge location is expected to move towards the far bank at a certain rate, however this rate reduces due to the reduced turbulent heat concentrations dispersion.

Figure 6.1.23 shows a relationship between the air temperature in degrees celsius and the ice free width. An effluent temperature of -20°C and an air temperature of -5°C provoke approximately 46 meters in width of ice free waters in the vicinity of

the thermal effluent and 300 m downstream of the side-discharge.

Turbulent flow hydrodynamics and heat budget conditions are evaluated using a k-ε turbulence model. The incorporation of a complete heat budget provided the capability of studying the effect of different hydrothermal and meteorological conditions on the melting pattern of an ice cover. An increase in air temperature or in side-discharge temperature, results in a non-linear increase in open water width as a function of the velocity ratio R.

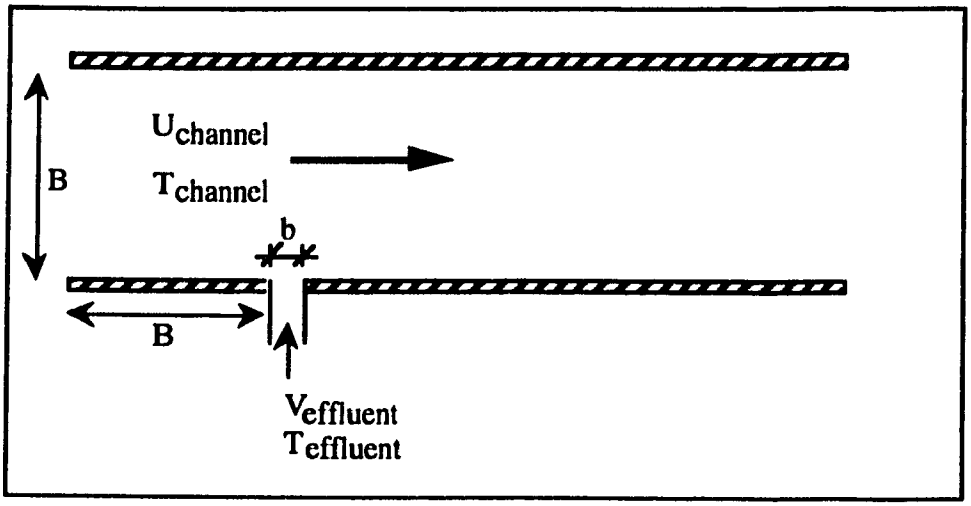

Figure 6.1.1: Test Channel Configuration.

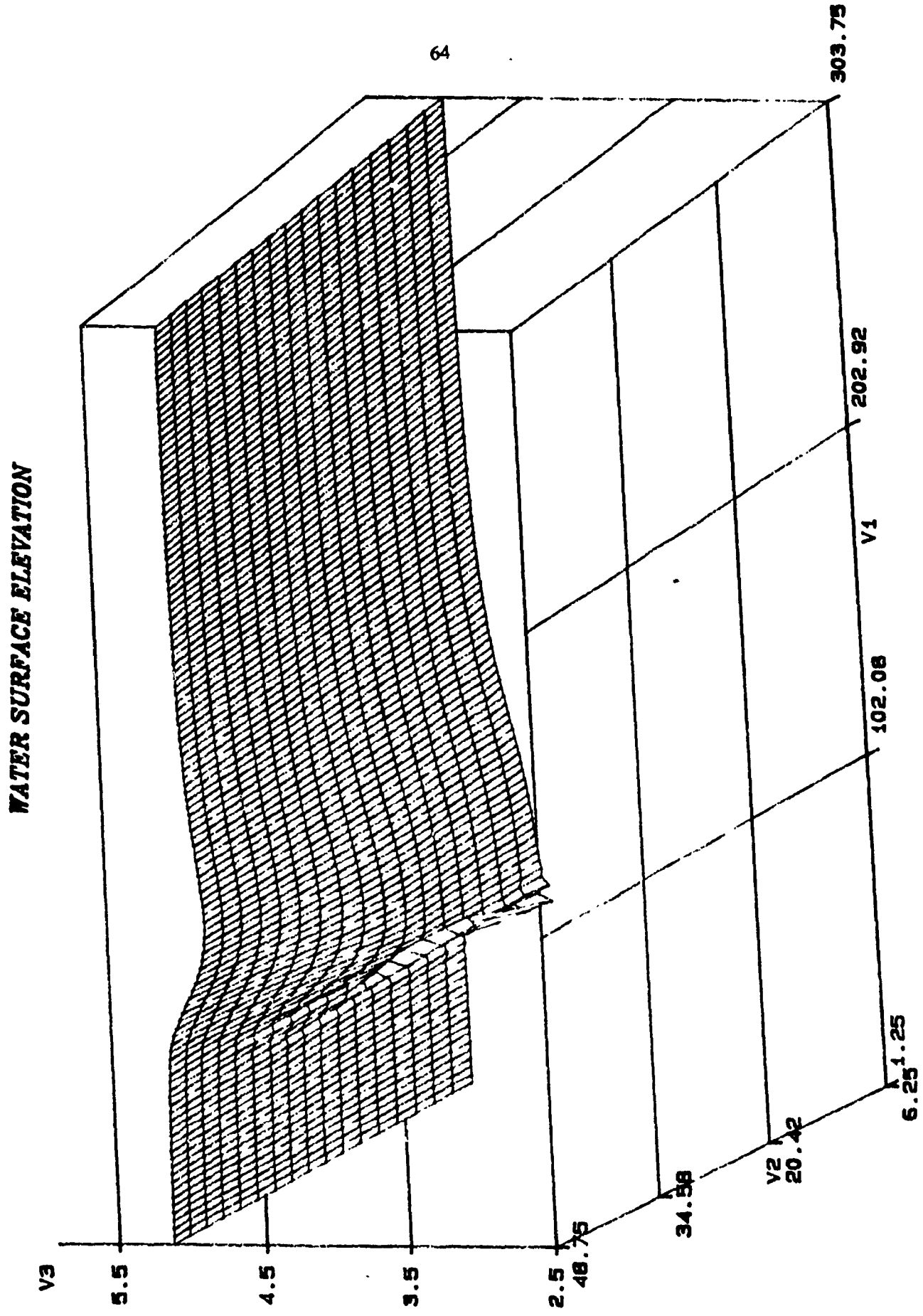

Figure 6.1.2: Effect of jet on main flow

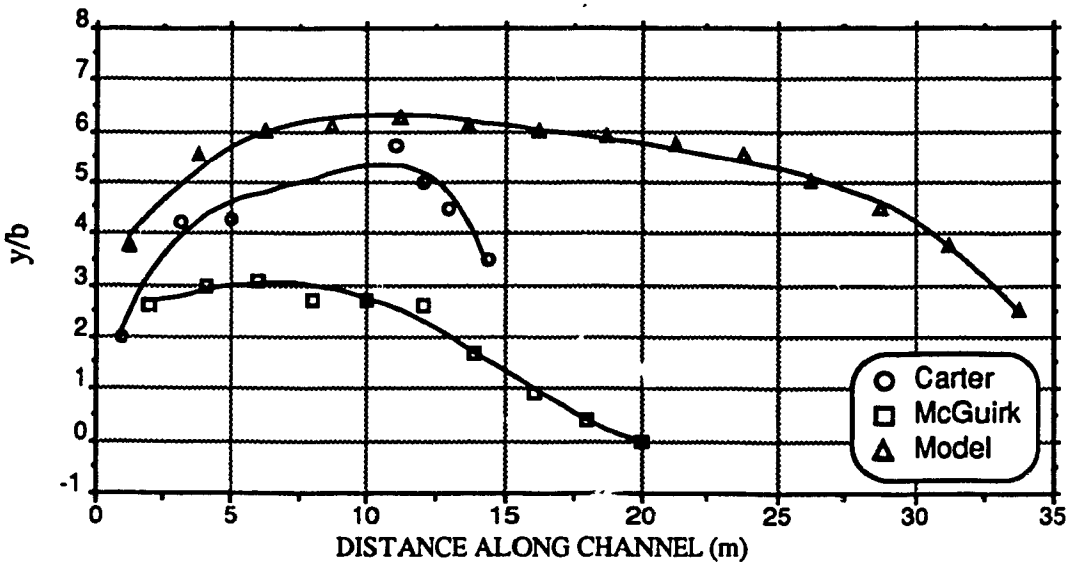

Figure 6.1.3: Jet trajectories of warm water discharges for R=2

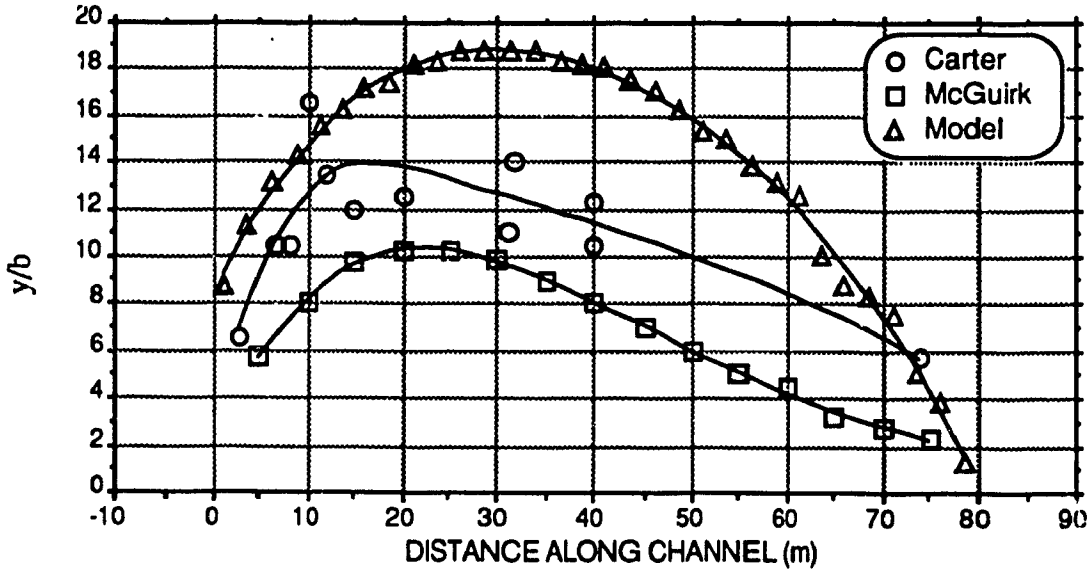

Figure 6.1.4: Jet trajectories of warm water discharges for R=5

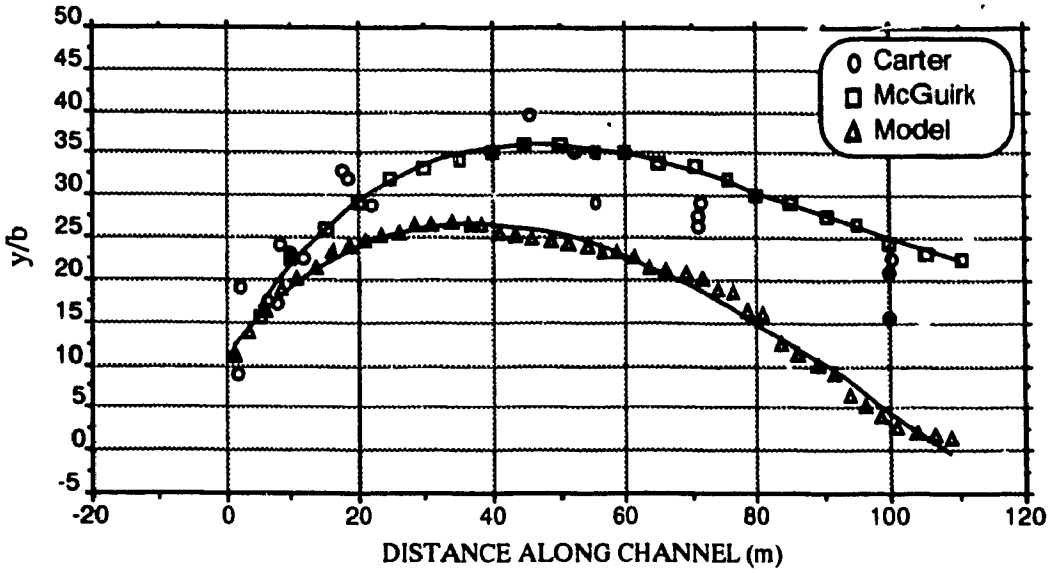

Figure 6.1.5: Jet trajectories of warm water discharges for R=10

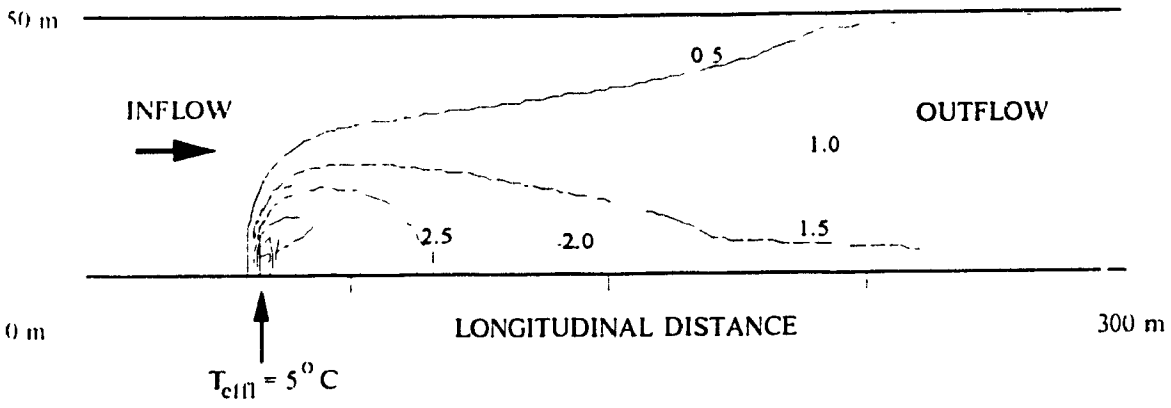

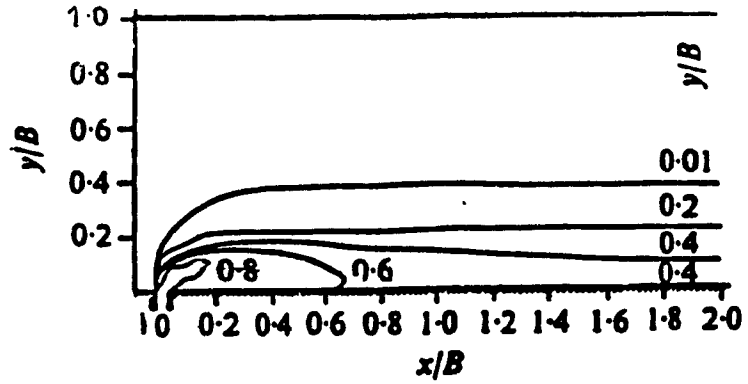

MCGUIRK AND RODI PREDICTIONS (1978)

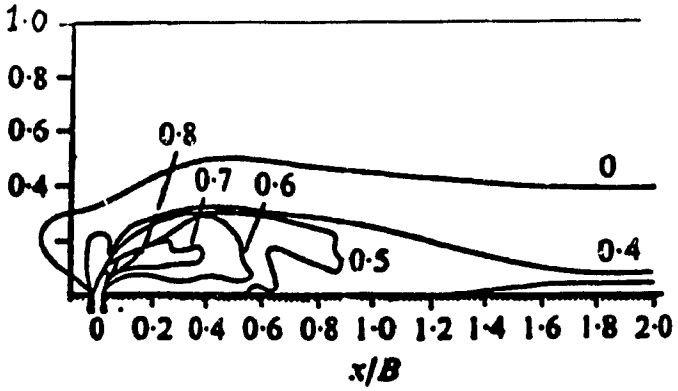

EXPERIMENT OF CARTER (1969)

Figure 6.1.6: Isotherms under ice free conditions for R=2

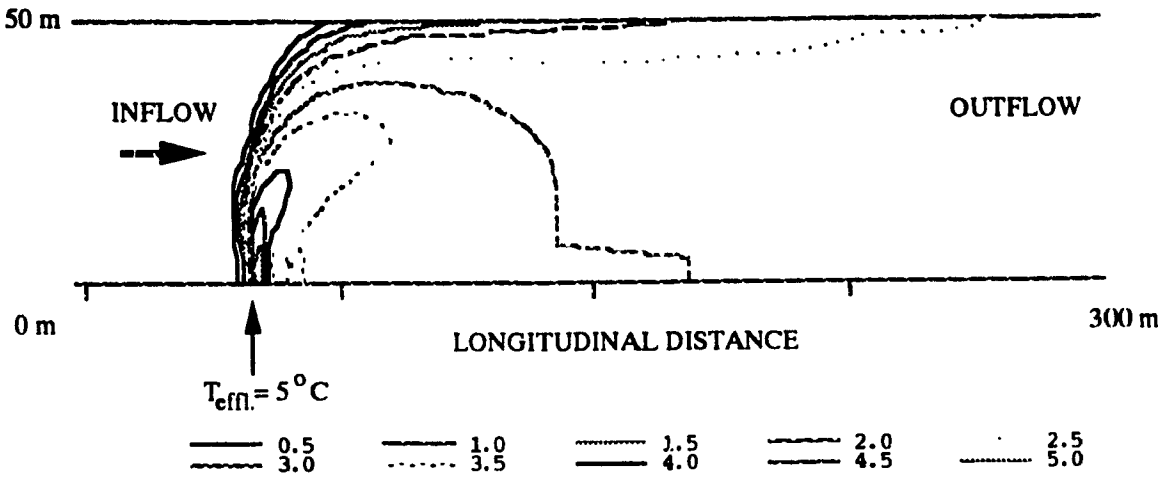

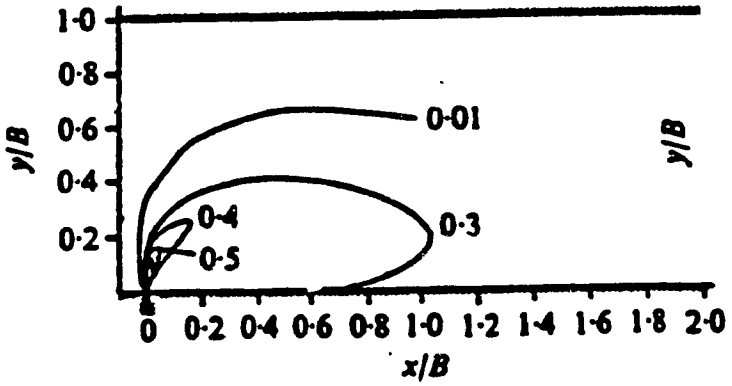

MCGUIRK AND RODI PREDICTIONS (1978)

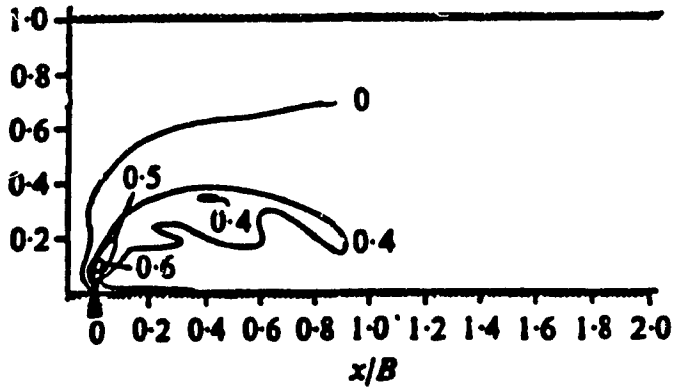

EXPERIMENT OF CARTER (1969)

Figure 6.1.7: Isotherms under ice free conditions for R=10

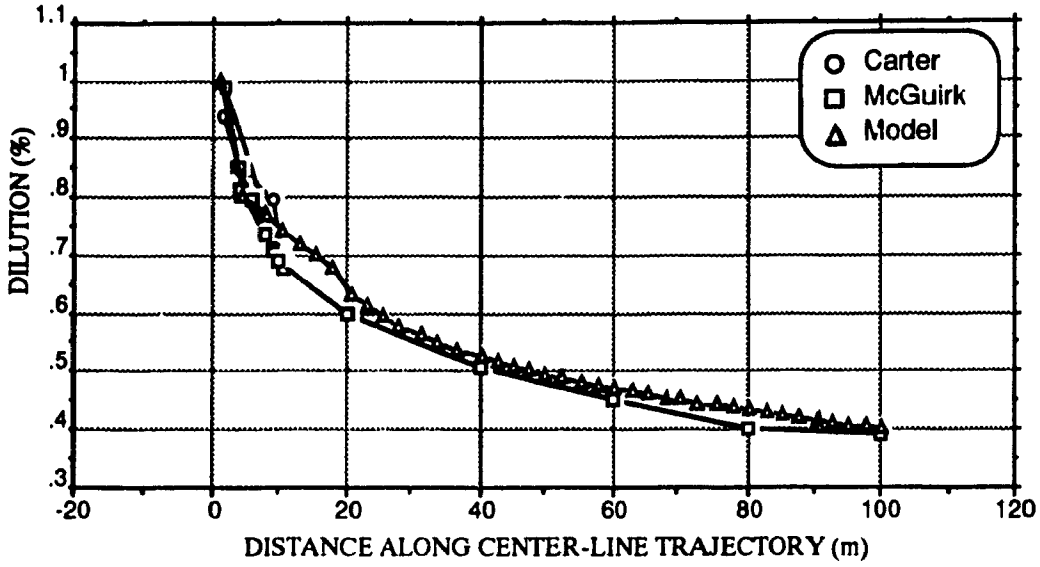

Figure 6.1.8: Dilution along centre-line trajectory for R=2

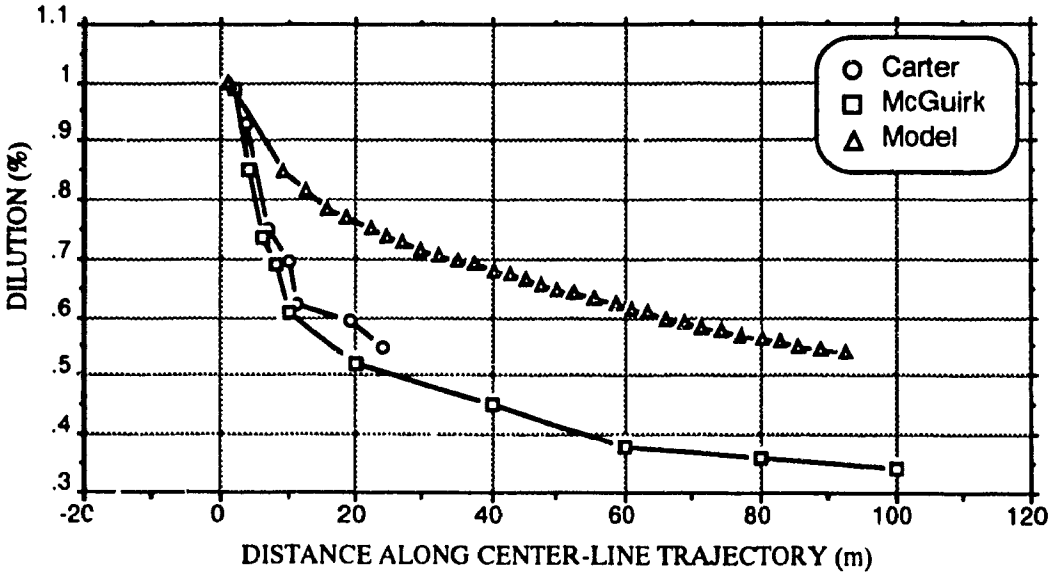

Figure 6.1.9: Dilution along centre-line trajectory for R=5

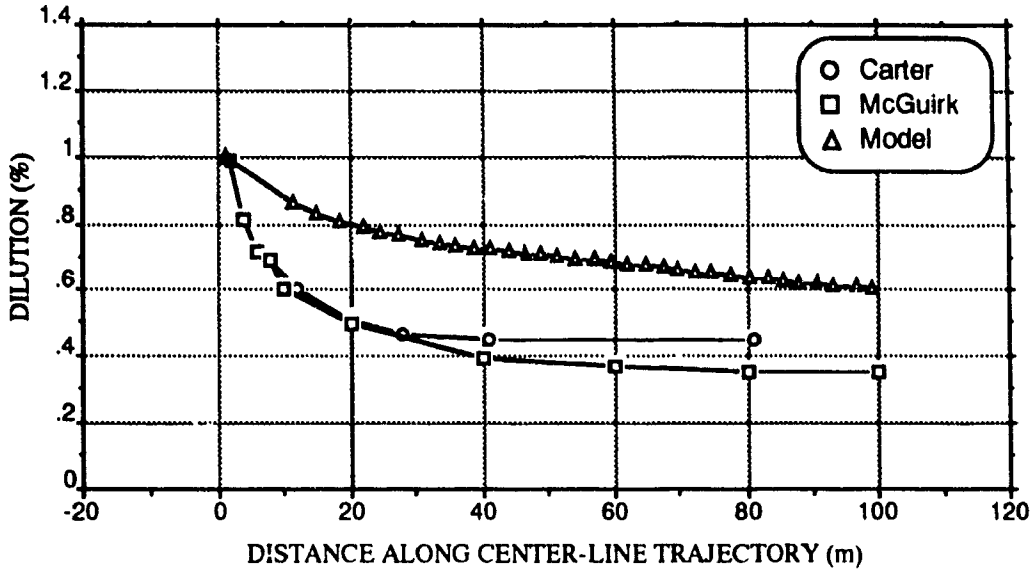

Figure 6.1.10: Dilution along centre-line trajectory for R=10

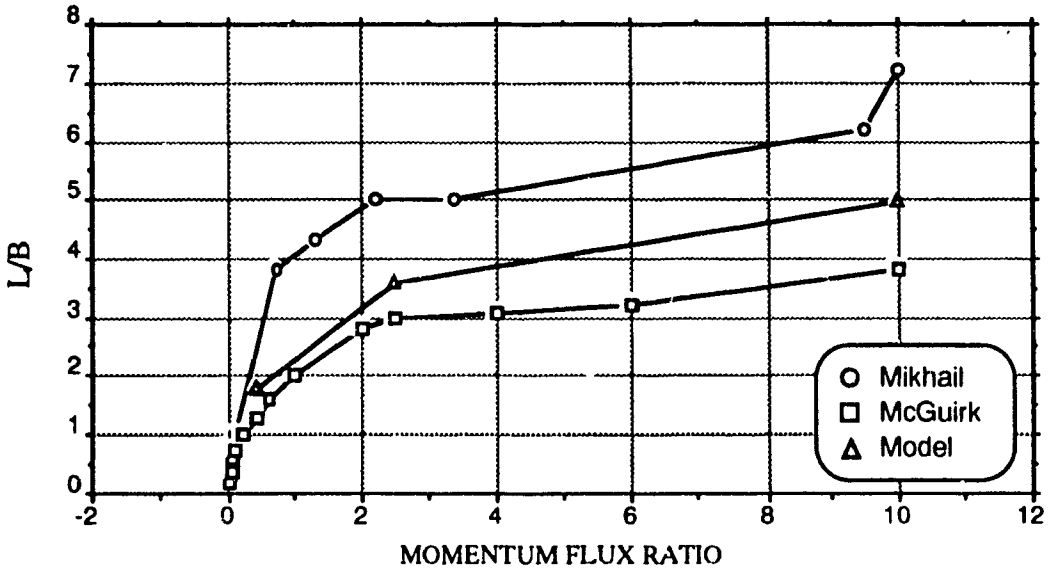

Figure 6.1.11: Reattachment to main channel width ratio L/B length of two models

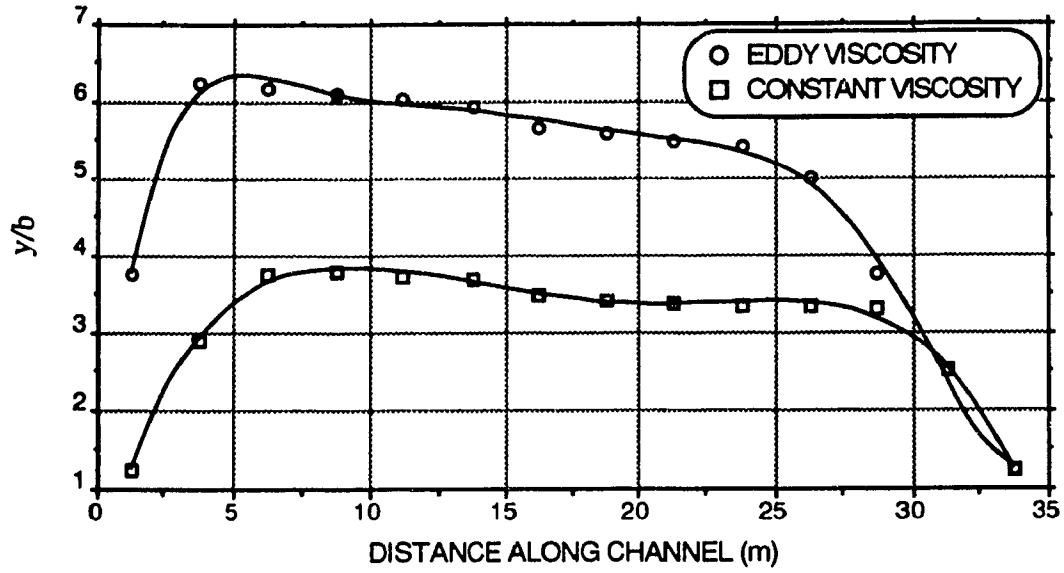

Figure 6.1.12: Warm water jet trajectory of two models, R=2

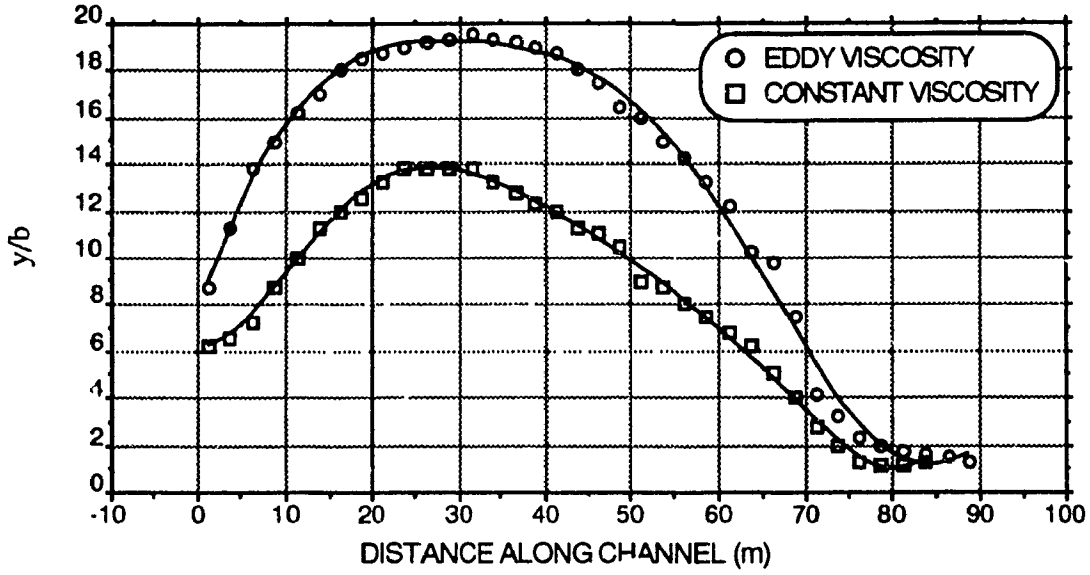

Figure 6.1.13: Warm water jet trajectory of two models, R=5

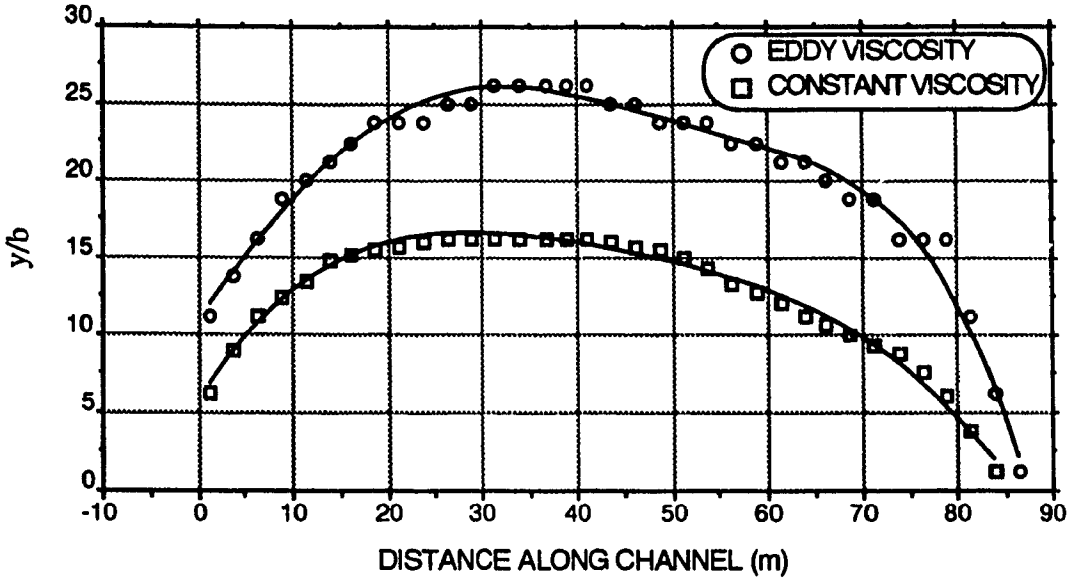

Figure 6.1.14: Warm water jet trajectory of two models, R=10

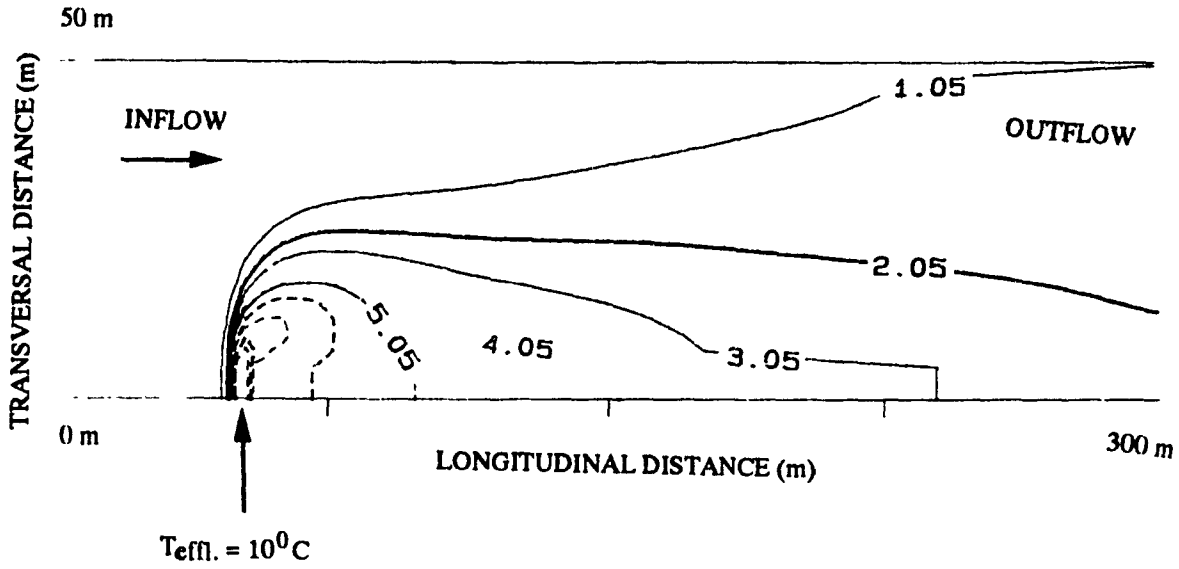

Figure 6.1.15: Isotherms under ice cover for k-ε, R=2

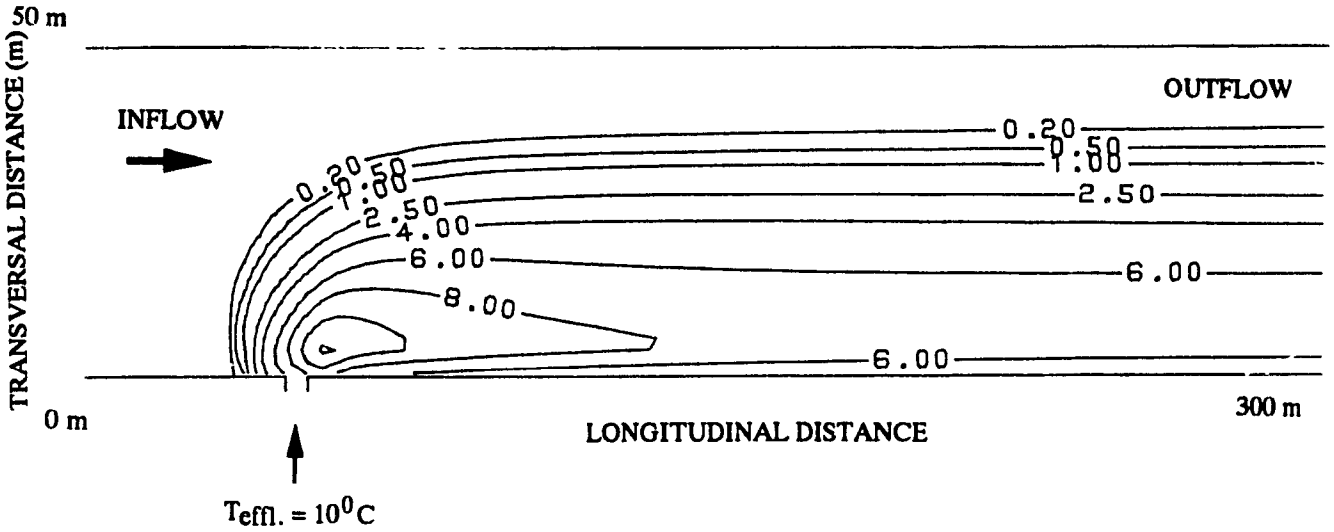

Figure 6.1.16: Isotherms under ice cover for constant viscosity model, R=2

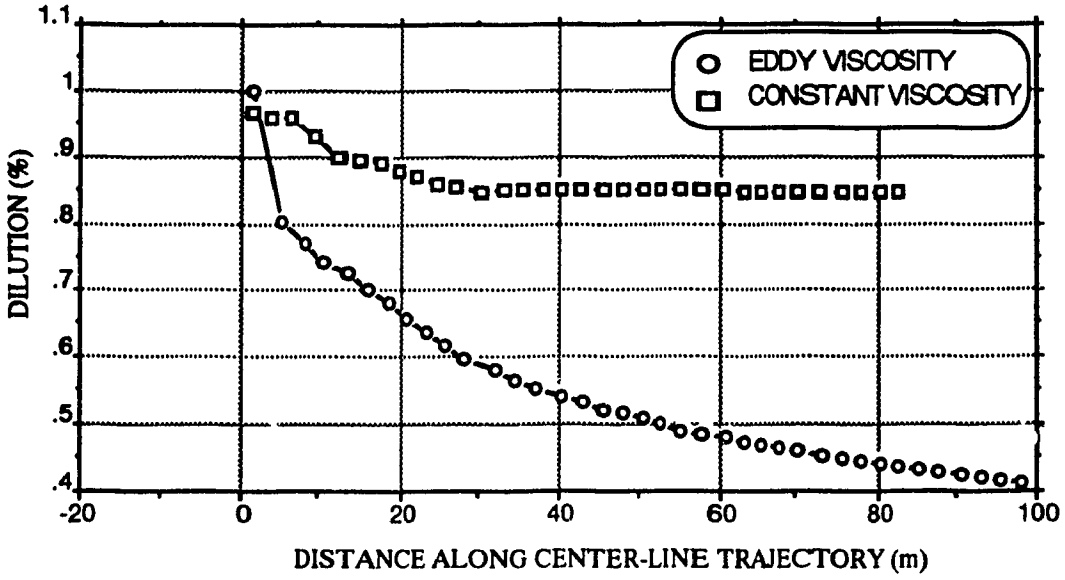

Figure 6.1.17: Dilution along centre-line trajectory of two models, R=2

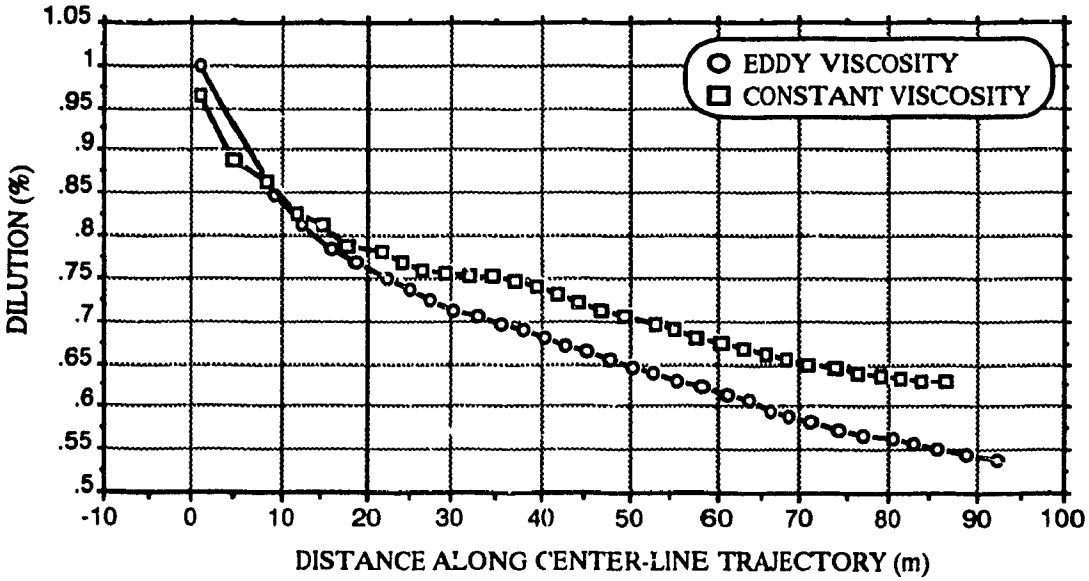

Figure 6.1.18: Dilution along centre-line trajectory of two models, R=5

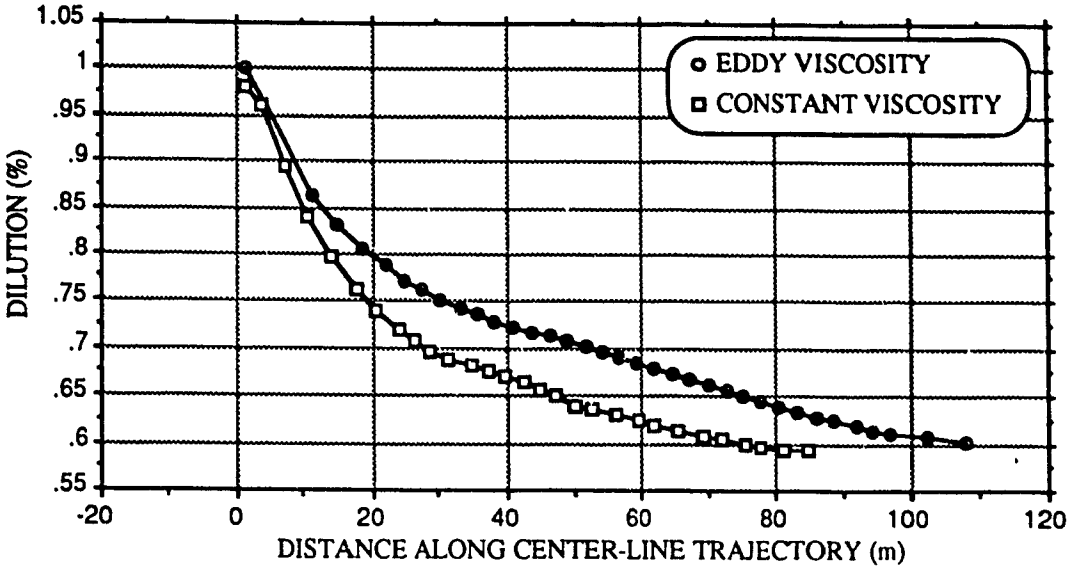

Figure 6.1.19: Dilution along centre-line trajectory of two models, R=10

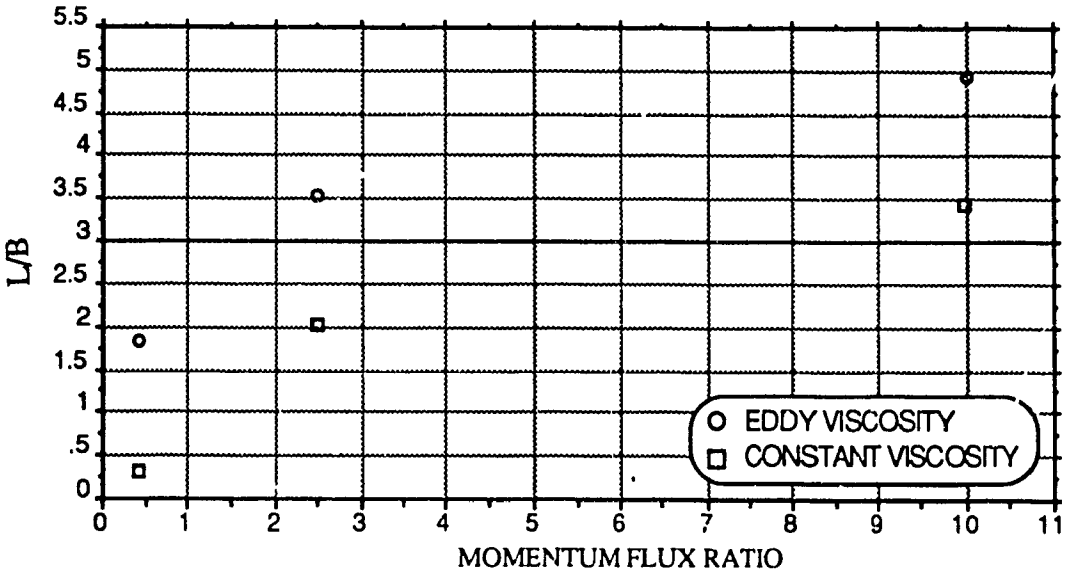

Figure 6.1.20: Reattachment to main channel width ratio L/B length of two models

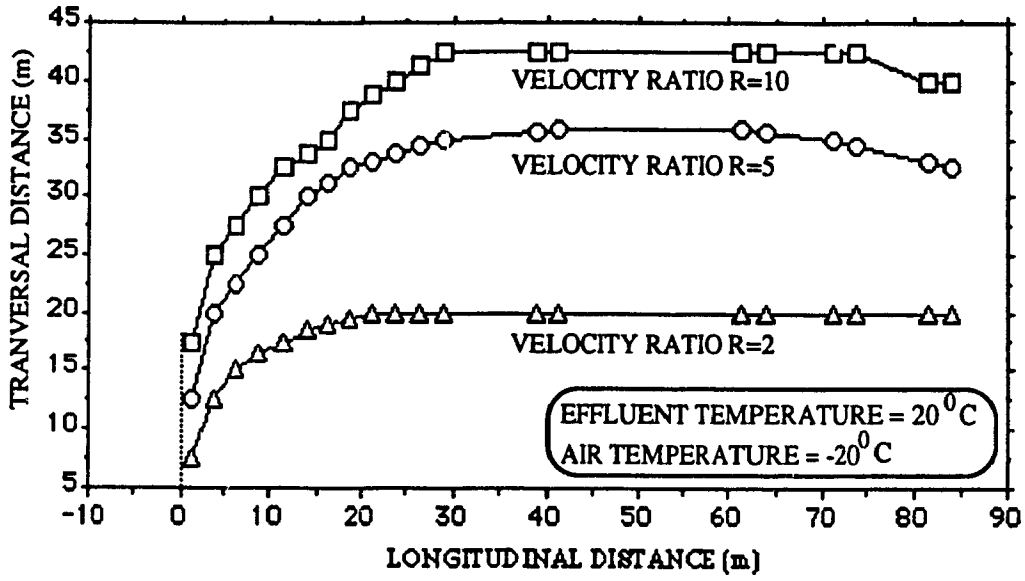

Figure 6.1.21: Open water extent for velocity ratio R=2, 5, and 10

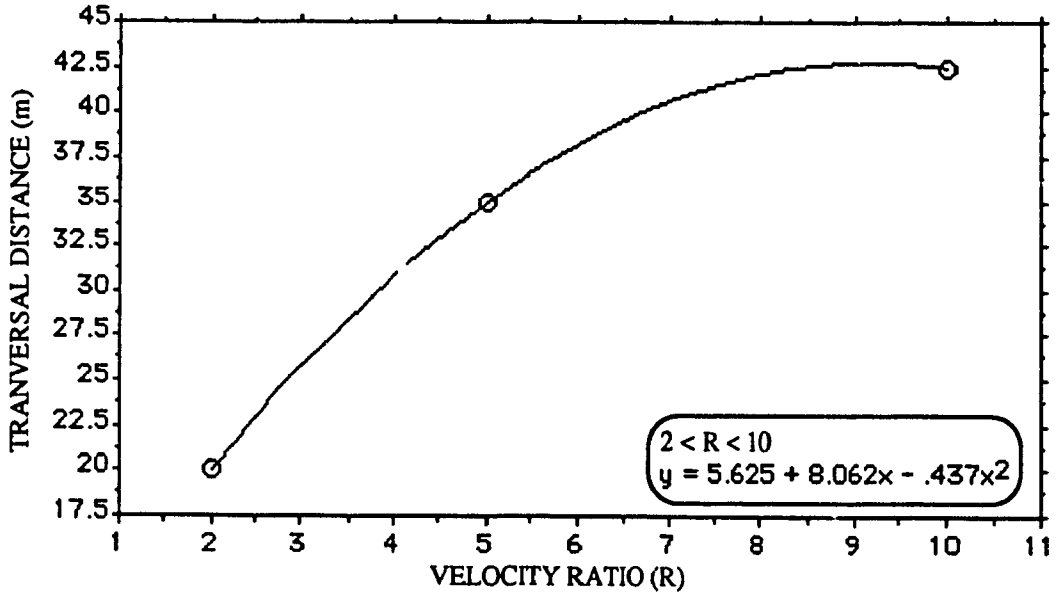

Figure 6.1.22: Influence of the velocity ratio on the near field ice free opening

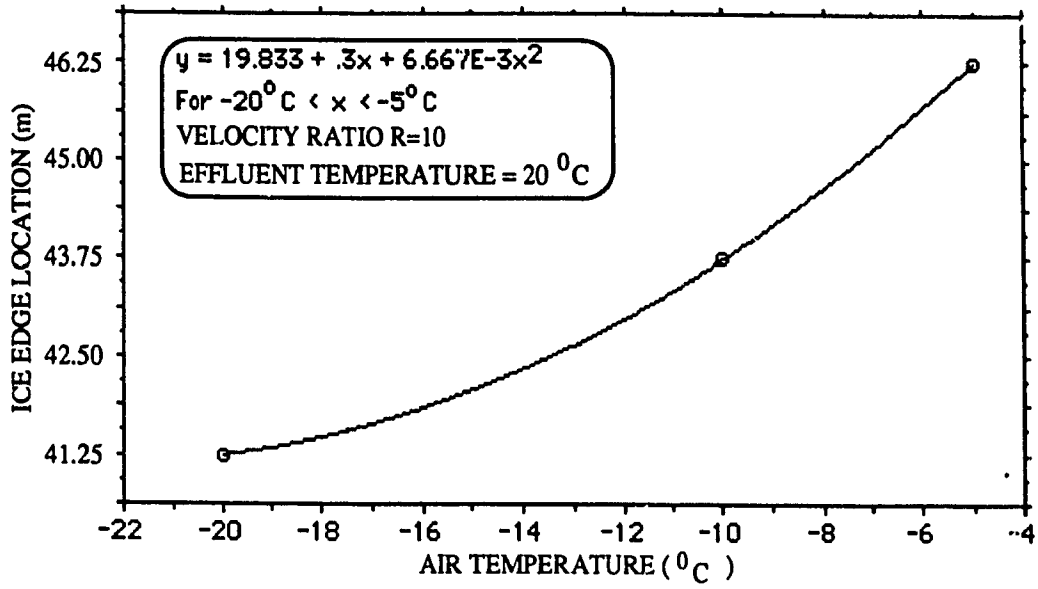

Figure 6.1.23: Near field ice free opening as a function of air temperature

6.2 Modelling of Ice Cover Melting

Modelling ice cover melting under turbulent flow conditions is the next step in the verification process of the performance of the numerical model. In the previous section the k-ε model was verified for its capability in evaluating the turbulent flow characteristics, under different inflow conditions. It is appropriate at this point to test the model against laboratory experiments for its capability in predicting the melting of an ice cover due to an added heat source.

Comparison With Hewletts' Experiments

Experimental and Numerical Set-up

Hewlett 1976, performed a series of experiments where an ice cover was artificially grown on the water surface in a laboratory flume located in a temperature controlled room. After the ice cover attained a desired and acceptable uniform thickness, the water temperature was increased slightly above 0°C to induce melting. Then the ice cover thicknesses were measured at various points along the length of the cover and at different times. The objective of this series of numerical tests is to examine the model predictions against experimental investigations.

Fig. 6.2.1 shows the geometrical configuration of the channel and ice cover considered in Hewlett's experiments. The channel consists of an upstream open water portion, ice covered middle portion and another open water downstream portion. The upstream water portion extends over 210 cm in length, the middle portion includes 820 cm of ice cover, and the downstream section extends 170 cm ice free. Water flow of 1ft was considered. The channel is rectangular in shape having a width of 60 cm. The

test flume shown in Fig. 6.2.1 has a 40-foot working section, and a variable slope. The flow in the channel changes from free surface to ice covered edge and again to open water conditions.

The inlet temperature is maintained at a value higher than 0°C. The air temperature is set 0°C, a value which ensures that the net heat flux to the ice cover is positive (upward). The ice cover thickness was not fully uniform because of flume wall irregularities and the instability of the freezing process. The discharge per unit width was kept roughly at a constant value of 2.23 m^2/min and the upstream water temperature at 1°C.

Out of seven experiments performed by Hewlett, only three experiments 1, 6, and 7 were successful. The other experiments were dropped because of equipment or experiment malfunction.These experiments are all performed under similar hydrodynamic, hydrothermal, and laboratory conditions. The only difference that exists between them is the initial planar thicknesses of the ice cover which vary from from one experiment to the other. This variation in the ice cover thicknesses is attributed to the inaccuracy of the method used for growing the ice cover.

In the experimental set-up, the flow rate, water temperature, and air temperature were first set to the desired level. Cool water was pumped into the flume at a rate of 0.2 cfs, until a depth of 25 cm. The room temperature then was lowered to 5°F. The ice cover was allowed to form to an average thickness of 5cm. The ice cover then was cut at the inlet and outlet perpendicular to the flume, leaving an 820 cm long ice cover. The room temperature was then raised to 0 °C, and ice cover profiles and thicknesses were measured afterwards at different time levels.

A duplication of the experimental procedure was made in setting up the numerical model. The geometry of the channel was fitted into a uniform rectangular grid system of 0.2m by 0.03 m cell size, and initial boundary conditions were imposed. Initial values of the parameters are not of major influence on the steady-state solution, however care must be taken for the selection of these values to ensure the proper convergence of the solution. Such care could be the proper choice of the turbulent kinetic energy k and the rate of its dissipation ε. The velocity field was set to a constant value of 0.186 m sec^{-1} and the temperature distribution over the entire domain was initialised to 1°C.

The model was run until steady-state was achieved for the hydrodynamic and temperature equations. The k-ε turbulence model was then introduced and run again until steady-state is reached. At this stage, the ice cover was imposed with exact initial ice thicknesses as specified by the experimental studies. In order to account to this sudden imposition of the ice cover, 92% of the average ice cover thickness was added to the water depth in the open water portions. The program was then run without ice melting until steady-state conditions were re-established again.

Ice cover profiles - Expts. 1, 6, & 7

Figs. 6.2.2 and 6.2.3 present a comparison between measured and implemented temperature and discharge profiles as a function of time, respectively. The atmospheric conditions required by the model for the calculation of ice cover melting, such as, the cloud cover, air temperature, wind velocity and barometric pressure have to be specified. The air temperature is clearly defined at 0°C; the wind velocity was set to a value slightly above zero to account for the circulation produced

by the cooling system; the cloud cover was set to nine tenths; and the barometric pressure to 0.7547m of Hg. Table 6.2.1 summarises the experimental and the corresponding numerical model parameters. Tables 6.2.2, and 6.2.3 show the distribution of the probes over the length of the span and the corresponding ice cover thicknesses measured in the laboratory and used in the numerical model respectively.

A list of the Figures representing comparisons between measured and predicted ice cover thicknesses over the entire length of the flume together with their corresponding times of measurement, for experiments 1, 6, and 7 is given in table 6.2.4. The time in all the Figs., represent the elapsed time after the beginning of the melting process.

Figures 6.2.4, 6.2.5, and 6.2.6 present a comparison between computed and measured ice cover thickness longitudinal profiles, for experiment 1, 6, and 7 respectively, and at 100, 200, and 300 minutes from the start of melting. The difference between measured and computed ice cover melting pattern is investigated in two regions in the ice field. The first region is located near the ice cover leading edge, while the second region extends over the rest of the downstream portion of the ice cover. In the leading edge region, experiment 1 reveals that the predicted longitudinal ice cover thickness profile, after 100 min of the commencement of the melting process, compares very favourably to the measured profile. However, beyond 100 min, the difference between predicted and measured ice cover thicknesses increase, as shown in Fig. 6.2.4 at 200 min and 300 min, where the predicted ice cover thickness was less than the measured one.

On the other hand, the difference between the measured and computed ice cover thickness profiles for experiment 6 is quite small, as shown in Fig. 6.2.5. Also, the melting pattern of the ice cover is simulated accurately at the leading edge as well as at the downstream region of the ice cover. Experiment 7, results in a relatively larger difference between measured and computed ice cover thickness profiles, as shown in Fig. 6.2.6. The extent of ice cover melting is underpredicted by the model over the entire ice cover domain. Also, the behaviour in the melting characteristics of the ice cover between measured and computed, is different from that of experiment 1. In experiment 1, the model underpredicts the melting of the ice cover at the leading edge and slightly overpredicts it downstream of the leading edge, while in experiment 7, the melting is underpredicted over the entire domain of the ice cover.

This change of behaviour between the measured and computed ice cover thicknesses from one experiment to the other can be attributed to the difficulty in duplicating laboratory experiments. The numerical model on the other hand, requires little if no changes for performing repeatedly similar experiments.

Fig. 6.2.2 depicts the inflow temperature fluctuations as recorded over the time of experiment 1. In this Fig., the temperature input used in the numerical model approximate very closely the actual water temperature recorded and therefore the computed ice thickness profile shows very close reproduction of the experimental findings. However, to allow for further verification of the model, the experimental inlet temperature was approximated by an average value of 1°C. This renders the inlet temperature imposed in the model to be about 0.1°C higher than the average measured water temperature, which may explain the slight increase in melting predicted by the computational model.

In the region of the leading edge, the melting process described by the laboratory experiments is quite different from the one shown by the computations of the k-ε model. The difference between measured and predicted ice cover thicknesses as a function of time, for the upstream end of the leading edge region, and the downstream region, are shown in Fig. 6.2.7. The rate of melting of the ice cover in the downstream region is found to be linear, while for the leading edge region, this rate varies non-linearly in time. From a global point of view the difference between measured and computed ice cover melting is at a maximum at the leading edge. From that point on, this difference reduces gradually along the downstream end of the ice cover, up to a certain point 'C' where the measured and computed ice cover thicknesses coincide. Beyond that point the rate of change between the measured and predicted ice cover thickness slightly increases until a constant value is maintained, but with predicted ice cover thicknesses lower than the measured ones.

Temporal variations - Expt. 1

Figs. 6.2.8 to 6.2.10, present the ice cover thicknesses for experiment 1, at approximately 60 cm, 190 cm, 400 cm, and 800 cm from the leading edge as a function of time. It is shown in Fig. 6.2.8 that at about 75 min after the commencement of the melting process, the predicted ice cover thicknesses matches perfectly the measured values. Beyond that time, the computational procedure underestimate the measured values with, however a maximum percentage difference of less than 5%. The measured and predicted ice cover melting rate at 190 cm and 400 cm downstream from the leading edge, are approximately equal, with a maximum percentage difference of less than 3%. At about 800 cm downstream from the leading edge, Fig. 6.2.10 shows that more melting is reported by the numerical predictions than in the experimental measurements.

Additional simulations have been performed for experiment 1, to study the effect of the bottom slope on the extent of melting of the ice cover subjected to the same initial conditions. The results are depicted in Figs. 6.2.11 to 6.2.13. Fig. 6.2.11 presents measured and predicted longitudinal profiles of the ice cover thickness at 100 min, 200 min, and 300 min respectively, for the cases of a horizontal bed and a slope of 0.001. The obtained results indicate that more melting had been predicted in the sloped bed case than that of both the experiment and the horizontal bed case.

No appreciable difference between the two numerical and experimental cases, in the ice cover thickness profiles, is observed at the leading edge region between the measured and computed runs, at 100 min. However, a slight difference in ice cover melting pattern in the leading region begins to take place at later stage in time, as shown in Figs. 6.2.11. At 200 minutes, the measured ice thicknesses were found to be less than the predicted values for the sloped bed case at approximately 98 cm from the leading edge and for the horizontal bed case at about 120 cm from the leading edge. After these two points, predicted values of the ice thicknesses for both cases are less, of about 4% for the sloped bed case than the horizontal case at 160 cm from the leading edge and 1.5% at 800 cm.

At 300 minutes, Fig. 6.2.11 reveals an increasing trend in the rate of change of the ice cover thickness profile in the leading edge region. There is an approximately 165% increase in the difference of the rate of change of ice cover thickness between the sloped channel case predictions and the experimental measurements, near the leading edge region. However, near the end of the ice cover, the difference in the rate of change of the ice cover thickness is reduced by about 20%. Also, comparing the sloped channel and the horizontal channel predictions, the

difference in the rate of change of ice cover thickness in the leading edge region reaches a maximum reduction of 8.3%, and converges to the same values beyond 675 cm downstream from the leading edge.

Fig. 6.2.12 presents the measured and computed ice cover thickness profiles as a function of time, for both horizontal and sloped bed runs, of experiment 1. These figures reinforce the results previously discussed. Further examination of Fig. 6.2.12, shows that the simulation of a channel with a sloped bottom compared to a horizontal channel, produces better results in the leading edge region since more melting is predicted. On the other hand, beyond the leading edge region, the model overestimates the ice cover thicknesses for a channel with a sloped compared to a horizontal bed channel.

The increase in melting of the ice cover due to the sloping of the bottom of the channel can be attributed to the effect of the bottom slope on the velocity field as compared to a horizontal bottom. Longitudinal velocity profiles for both sloped and horizontal channels are presented in Fig. 6.2.13. In the sloped channel bottom case, flow velocity increases in the upstream uncovered region and underneath the ice cover. An increase of 5.7% of velocity is computed in the upstream open water region, 10% near the leading edge and 0.5 % at the toe of the ice cover. The velocity in the downstream uncovered section was practically of the same magnetude for both cases. This change in the longitudinal velocity distribution reduces the water level in the upstream open water and ice covered region in a much of a similar order. The hydrodynamic changes induced by the sloping of the channel bottom reduces the temperature dispersion in the longitudinal direction, thereby increasing the rate of melting of the ice cover.

Temporal variation - Expt. 6 & 7

Similar behaviour of ice cover melting is experienced in the simulation of experiment 7, with small exception at the trailing edge of the ice cover. Figs. 6.2.14 and 6.2.15, present comparisons between measured and predicted ice cover thickness variation as a function of time, for experiment 7, at 60 cm, and 800 cm from the leading edge. These Figs. show a acceptable difference between computed and measured ice cover thicknesses with the predicted values almost always larger than the measured one. The behaviour of the computed ice cover melting rate in experiment 7 is almost always underestimated as opposed to the computed ice cover melting rate in experiment 1. Fig. 6.2.16 shows this difference between the two experiments.

Simulation of experiment 6, reconfirm the behaviour of the ice cover melting computations, and prove the accuracy of the numerical model. Figs. 6.2.17 and 6.2.18 show the temporal variation of the ice cover thickness at 60 cm, and 800 cm respectively. The predicted ice cover thicknesses compare to the measured ice covered thicknesses, with an excellent agreement even in the leading edge region. This close prediction of the rate of change of the ice cover thickness in the leading edge region may be attributed to the maintain of inflow temperature at a constant value during the experimental investigations. In Figs. 6.2.17 and 6.2.18, the rate of change of the measured ice cover thickness which is represented by the slope of the line, is practically the same as the slope of the computed results. This indicates that the rate of ice cover melting in experiment 6 was less than that in experiment 1. This reduction in turn may be due to reduced temperature concentrations in the leading edge region for experiment 6.

Discussion to the results - Expts. 1, 6, & 7

In spite of the complex, unsteady hydrodynamic and thermal conditions in the experimental setting near the leading edge, as well as the oscillatory behaviour of the rate of ice cover melting in this region, it was found and confirmed numerically that after a certain distance from the leading edge, the ice cover melting as a function of time can be approximated by straight lines. The measured and predicted ice cover thicknesses are compared as shown in Figs. 6.2.19 and 6.2.20 for experiment 1, in Fig. 6.2.21 for experiment 7, and in Figs. 6.2.20 to 6.2.22 for experiment 6.

The curves which can be approximated by straight lines, reflect the difference between measured and predicted ice cover thicknesses. Scattered data represent non-linear behaviour, and lines with a steep slope indicate larger error between measured and predicted data, such as the case in the leading edge region. A positive slope indicates the divergence of measured and predicted ice cover thicknesses, while a negative slope represent the convergence of the measured and predicted ice cover thicknesses. A curve below the zero level indicates that the predicted rate of melting is larger than the measured rate of melting. Fig. 6.2.19, present the curves of the first six probes in experiment. The curves starting with probe 1 are characterised by a steep positive slope and a large scatter of data. The slope is then reduced in each consequent probe for both slope and scatter until the curve is nearly horizontal at probe 6.

In the downstream region, the predicted rate of melting is larger than the measured rate of melting and is shown in Fig. 6.2.20. The slope of the illustrated curves is negative and extends below the zero level. In experiment 7, the same thing has occurred, except that at no location on the ice cover had the predicted rate of

melting exceed the measured rate of melting as shown in Fig. 6.2.21. However, the scatter of the data and the slope of the lines, show similar behaviour for experiment 1. In experiment 6, a higher rate of melting was predicted as represented in Fig. 6.2.22. In the leading edge region, the lines are nearly horizontal indicating accurate predictions. however, along the downstream direction, the difference in the rate of melting increases in time as indicated by the slope of the lines.

From an overall point of view, the total amount of melting of the ice cover is predicted with a good accuracy. The average melting of the ice cover is represented in Figs. 6.2.23 to 6.2.25, for experiments 1, 6, and 7 respectively. The predicted average ice cover thicknesses for experiments 1 and 6 are in very good agreement with the measured ice cover thickness. However, for experiment 7, the computed average ice cover thickness is greater than the measured one, due to the underprediction of the ice cover thicknesses throughout the ice cover.

The predicted melting of the ice cover edge approximate sufficiently well the measured values for the first 150 min of computations. Thereafter, the numerical prediction for the edge melting were underestimated compared to actual observations. In fact, the theory of heat transfer from water to ice applied does not take into effect the turbulent behaviour of water acceleration at the ice cover edge. A study was performed by Weng, Y., Nov. 1989, to test three different methods of computing the heat transfer at the water-ice interface. The heat transfer coefficient calculations used in determining the melting of the ice cover are based on a constant temperature at infinity, variable temperature at infinity, laminar boundary layer, and turbulent flow. The effect of a variable temperature assumption on the results were small and therefore neglected.

The constant temperature assumption yields a percentage difference with experimental results of less than 0.5% at the downstream region and up to a point 'C' from the leading edge, and 52% at the leading edge. In considering an overall performance, the calculation of the heat transfer coefficient in a turbulent flow assumption produced a maximum percentage difference of less than 4% in the downstream region and 12% at the leading edge. Also in Marsh and Prowse 1986, a comparison of four different techniques (Dittus-Boelter equation, Colburn analogy, and Petukhov-Popov equation) for calculating the heat transfer coefficient at the water-ice interface were investigated. Their finding were that the heat transfer coefficients calculated from the Colburn analogy method were in closest agreement to those using a temperature decay approach. The Colburn analogy produced the best results.

Table 6.2.1: Comparisons Between Experimental and Numerical Set-up.

DESCRIPTION	EXPERIMENTAL	NUMERICAL
Length of Channel	12 meters	12 meters
Width of Channel	61 cm	60 cm
Ice-Cover Stretch	820 cm	820 cm
Upstream Uncovered Portion	210 cm	210 cm
Downstream Uncovered Portion	170 cm	170 cm
Average Discharge per Unit Width	2.23 sq. m. per min.	2.23 sq. m. per min.
Average Upstream Temperature	0.9804 Deg. Celcius	1.0 Deg. Celcius
Average Downstream Temperature	0.9346 Deg. Celcius	0.98 Deg. Celcius
Average Ice Thickness	5 cm	5 cm
Water Depth, No Ice Cover	20 cm	20 cm
Water Depth , With Ice Cover	25 cm	24.6 cm
Cloud Cover	Inside the Lab	Nine Tenths
Air Temperature	0 Deg. Celcius	0 Deg. Celcius
Wind Velocity	Inside Lab	5.56 m per sec. (Assumed Wind Due to Cooling System)

Table 6.2.2: Laboratory probe distribution and corresponding ice thicknesses

Experiment # 1			Experiment # 6			Experiment # 7		
Probe	D (cm)	Ice Thickness (cm)	Probe	D (cm)	Ice Thickness (cm)	Probe	D (cm)	Ice Thickness (cm)
1	12.2	5.4	1	60.96	4.2	1	42.67	4.3
2	24.7	4.95	2	73.46	4.3 + T = 1 min.	2	60.96	4.4
3	37.2	5.07	3	85.95	4.5 + T = 2 min	3	91.44	4.8
4	62.2	4.93	4	160.93	5.6 + T = 3 min	4	137.16	4.9
5	87.2	4.74	5	260.91	4.6 + T = 3 min	5	182.88	4.5
6	112.2	4.95	6	360.88	5.2 + T = 4 min	6	228.6	4.6
7	137.2	4.87	7	460.86	5.0 + T = 5 min	7	289.56	4.7
8	162.2	5.12	8	560.83	4.7 + T = 5 min	8	399.29	5.5
9	187.2	5.00	9	661.11	4.6 + T = 6 min	9	502.92	5.5
10	286.2	5.24	10	811.07	4.5 + T = 7 min	10	609.60	4.6
11	393.2	5.24				11	716.28	5.6
12	499.9	5.35				12	822.96	4.4
13	606.6	5.60						
14	713.2	5.50						
15	819.9	5.45						

Table 6.2.3: Numerical probe distribution and corresponding ice cover thicknesses

Experiment # 1			Experiment # 6			Experiment # 7		
From (cm)	To (cm)	Ice Thickness (cm)	From (cm)	To (cm)	Ice Thickness (cm)	From (cm)	To (cm)	Ice Thickness (cm)
220	240	5.4	220	260	4.2	220	280	4.3
240	260	4.95	260	280	4.3 + T = 1 min.	280	300	4.4
260	280	5.07	280	300	4.5 + T = 2 min	300	320	4.8
280	300	4.93	300	400	5.6 + T = 3 min	320	380	4.9
300	320	4.74	400	500	4.6 + T = 3 min	380	420	4.5
320	340	4.95	500	600	5.2 + T = 4 min	420	460	4.6
340	360	4.87	600	700	5.0 + T = 5 min	460	560	4.7
360	400	5.12	700	800	4.7 + T = 5 min	560	660	5.5
400	420	5.0	800	900	4.6 + T = 6 min	660	760	5.5
420	540	5.24	900	920	4.5 + T = 7 min	760	860	4.6
540	640	5.24				860	960	5.6
640	740	5.35				960	1060	4.4
740	840	5.6						
840	960	5.5						
960	1060	5.45						

Table 6.2.4: List of figures used for comparison with Hewletts' experiments

Figure		Experiment #	Description
From	To		
6.2.4	6.2.6	1	Ice Cover Thickness Profiles
6.2.8	6.2.10	1	Ice Cover Melting Variation in Time 60, 190, 400, and 800 cm from L.E.
6.2.11	6.2.11	1	Ice Cover Profile Comparisons Between Horizontal and Sloped Channel
6.2.12	6.2.12	1	Ice Cover Thickness Variation in Time, Slope V.S. no Slope at 60, and 800 cm from L.E.
6.2.14	6.2.15	7	Ice Cover Thickness Variation in Time for Experiment 7, at 60, and 800 cm from the L.E.
6.2.17	6.2.18	6	Ice Cover Thickness Variation in Time for Experiment 6 at 60, and 800 cm from the L.E.
6.2.23	6.2.25	1, 6, 7	Average Ice Cover Thickness as a Function of Time.

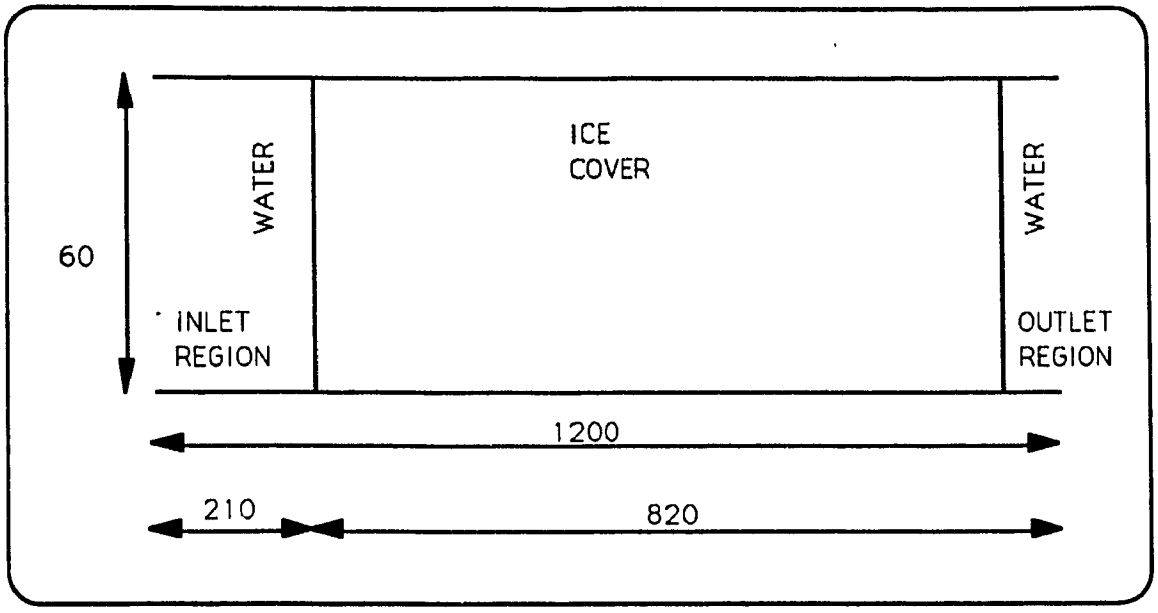

Figure 6.2.1: Channel geometry used in laboratory tests, cm

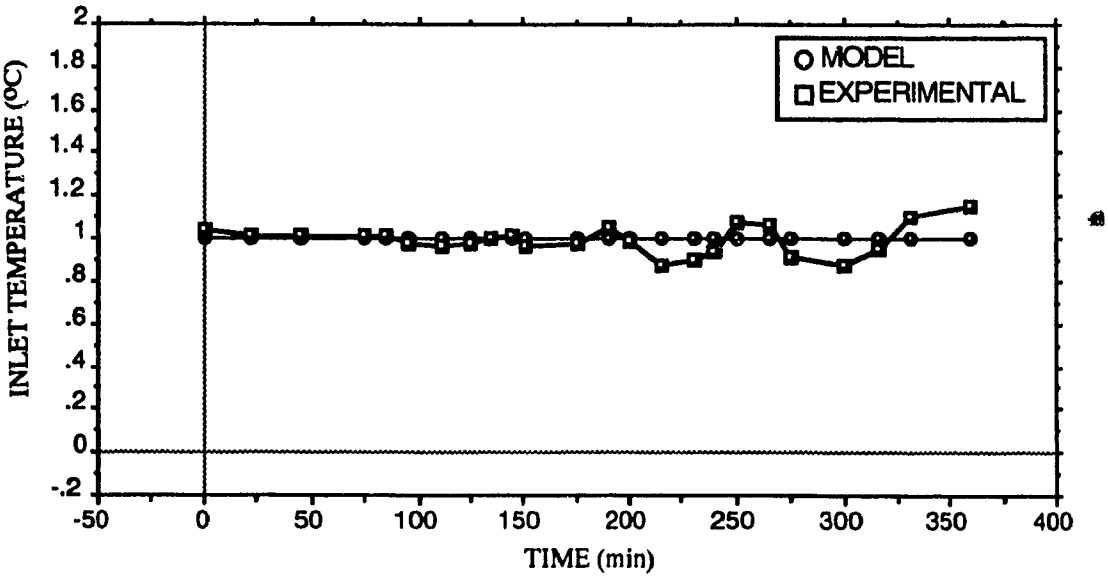

Figure 6.2.2: Experimental and model upstream water temperatures

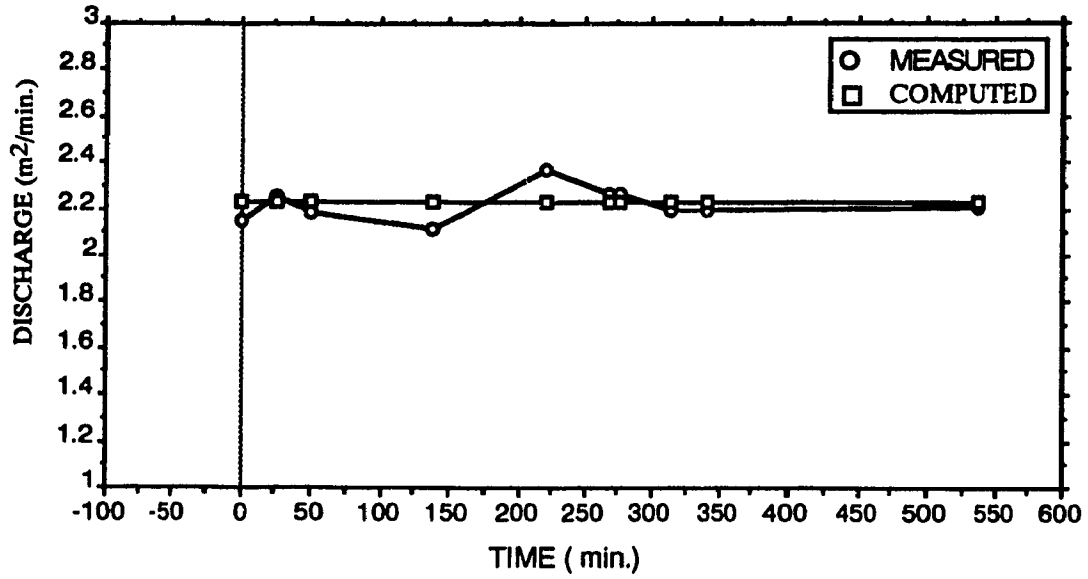

Figure 6.2.3: Experimental and model discharge variations

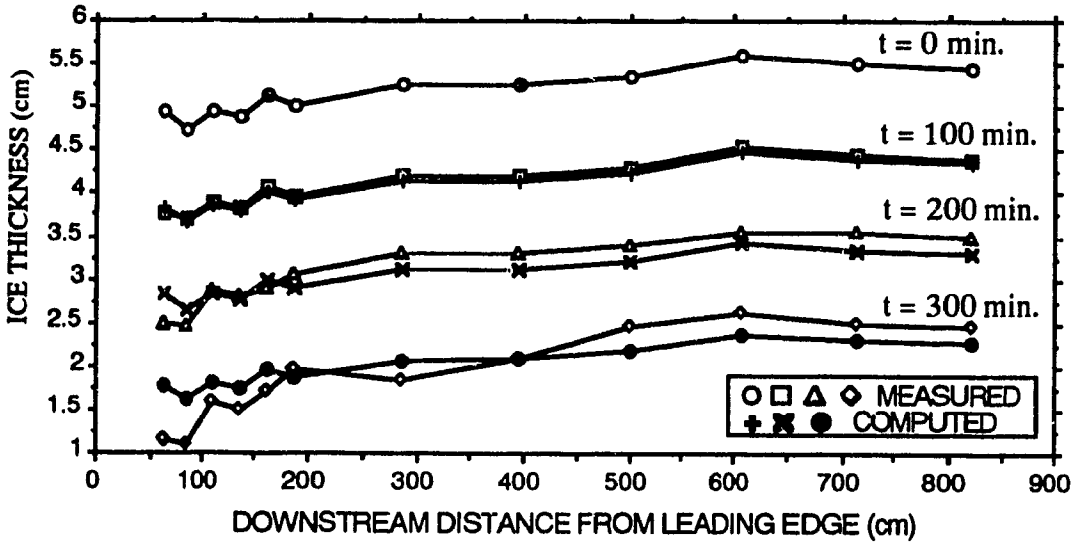

Figure 6.2.4: Longitudinal ice cover thickness profiles for experiment 1

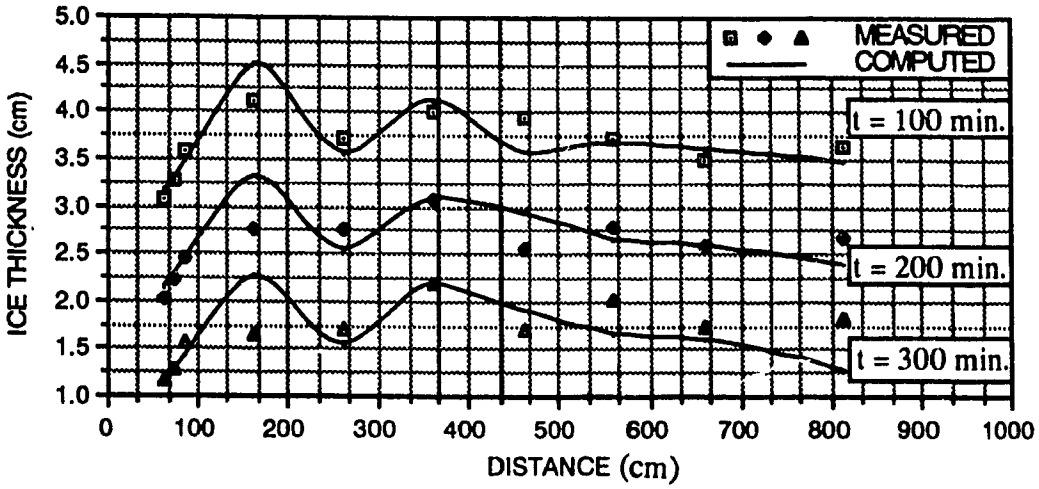

Figure 6.2.5: Longitudinal ice cover thickness profiles for experiment 6

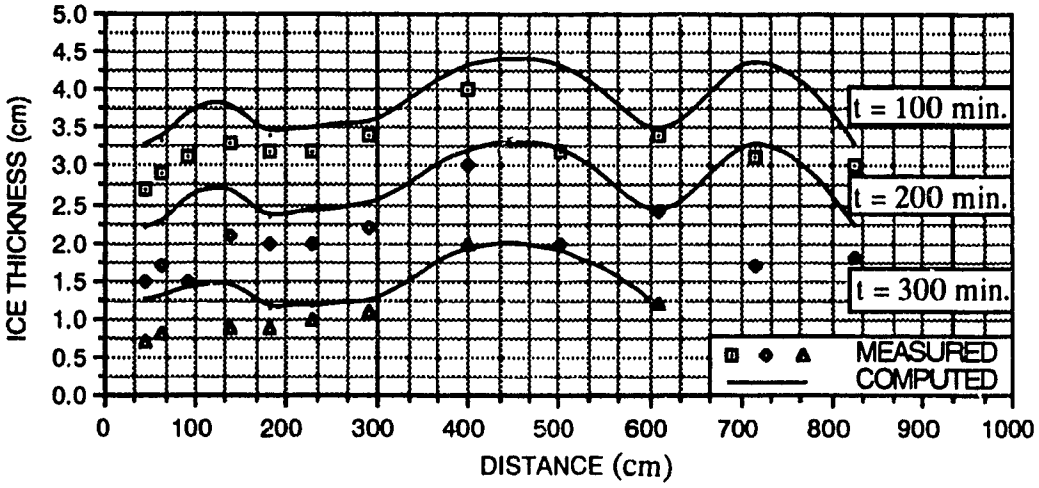

Figure 6.2.6: Longitudinal ice cover thickness profiles for experiment 7

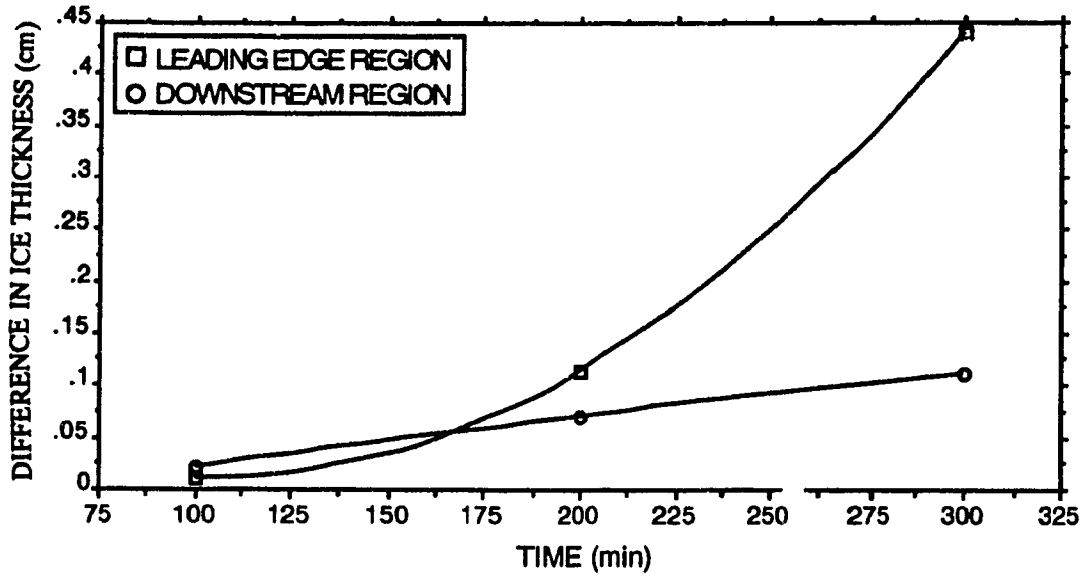

Figure 6.2.7: Difference in the change of ice cover thickness

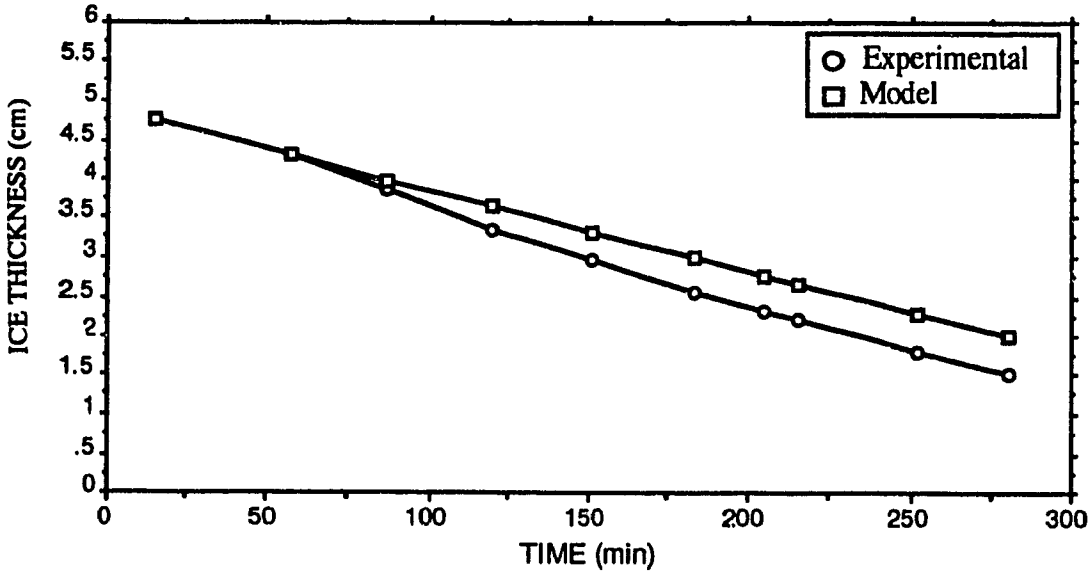

Figure 6.2.8: Ice cover thickness as function of time at 60 cm from leading edge, for experiment 1

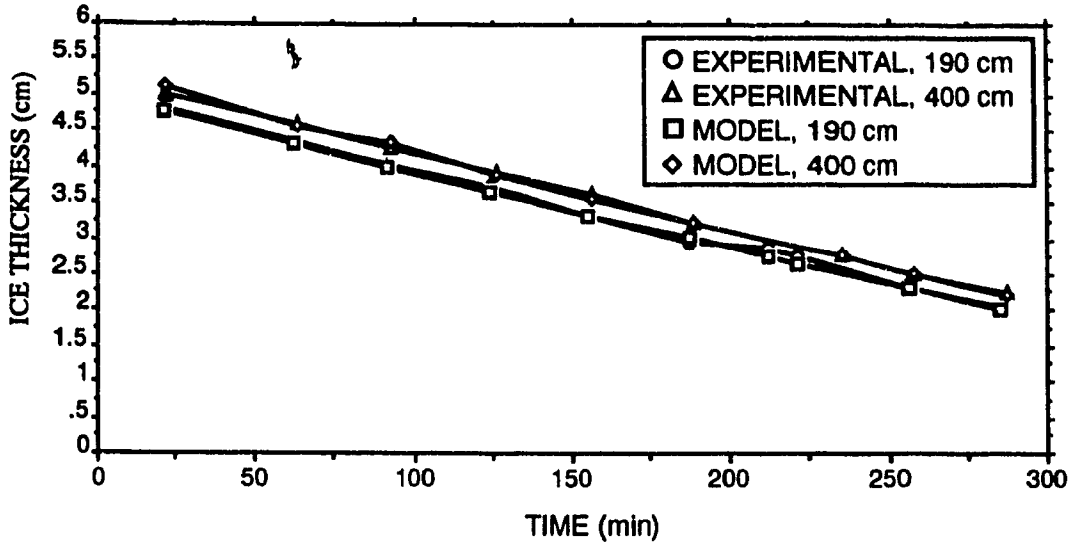

Figure 6.2.9: Ice cover thickness as function of time at 190 cm and 400 cm from leading edge, for experiment 1

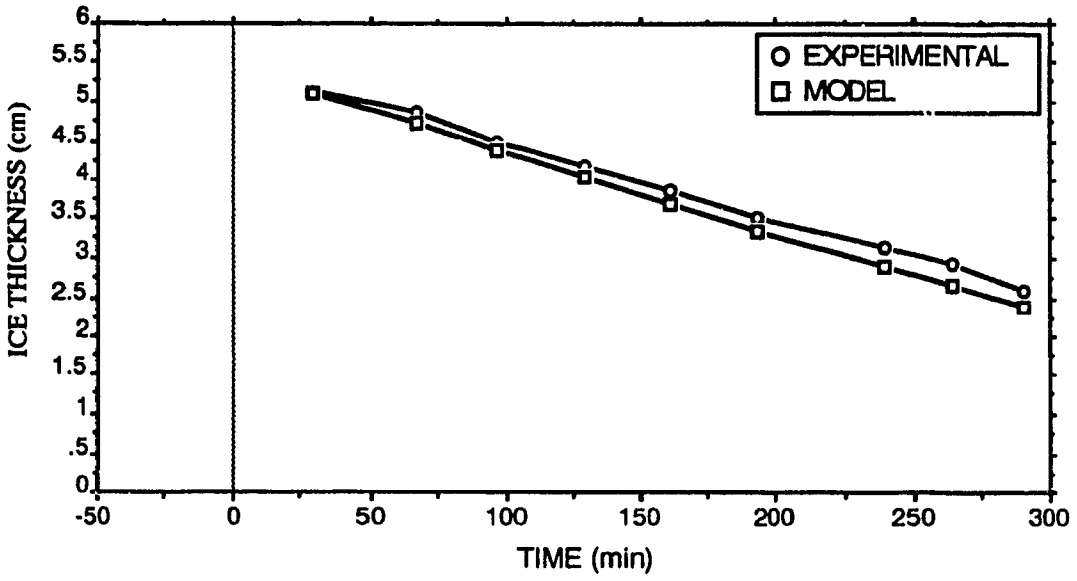

Figure 6.2.10: Ice cover thickness as function of time at 800 cm from leading edge, for experiment 1

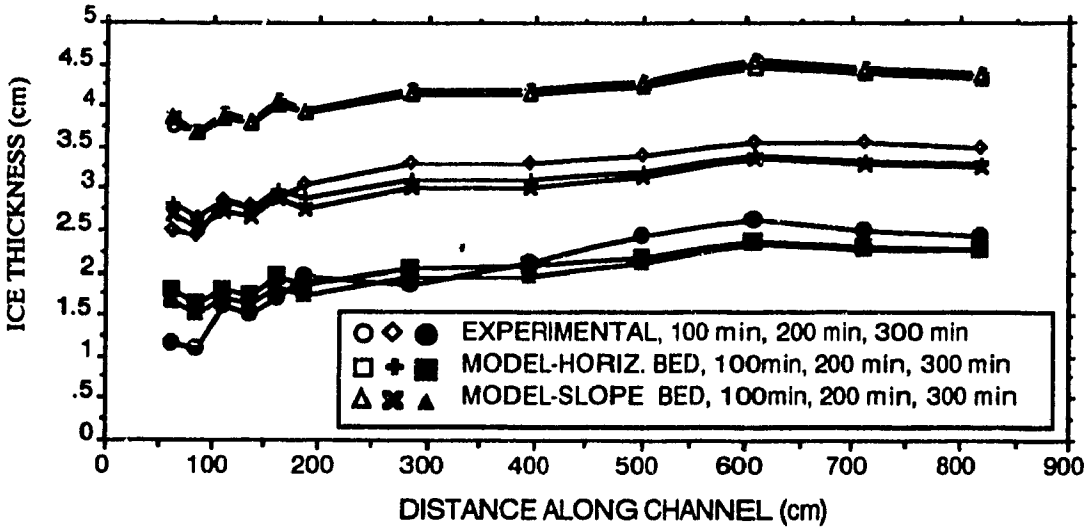

Figure 6.2.11: Experimental and computed ice cover thickness profiles for horizontal and sloped channel beds

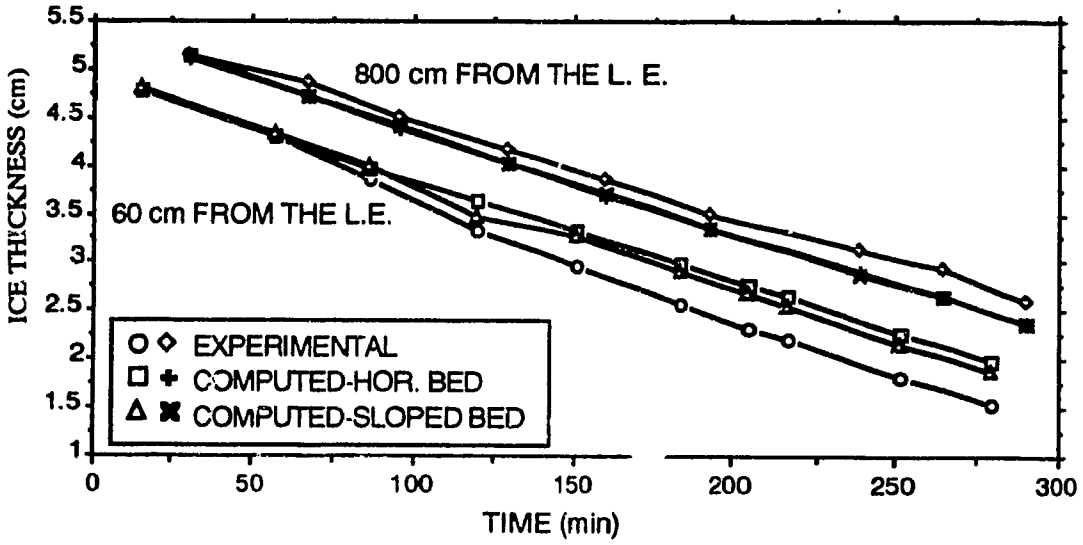

Figure 6.2.12: Experimental and computed ice cover thickness variation for experiment 1 at 60 cm and 800 cm from the leading edge

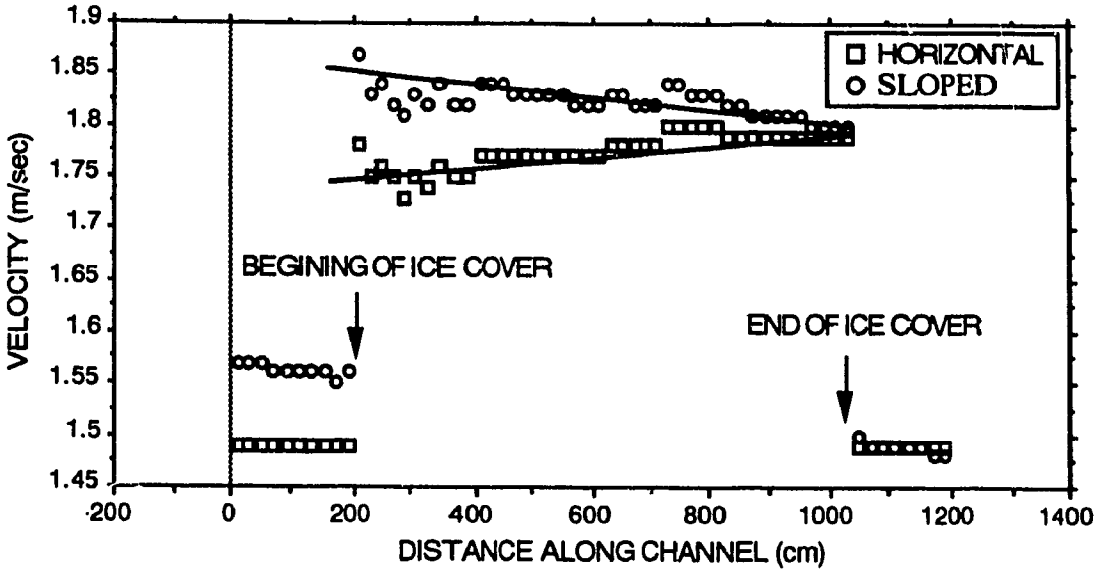

Figure 6.2.13: Longitudinal velocity profile for sloped and horizontal bed channels

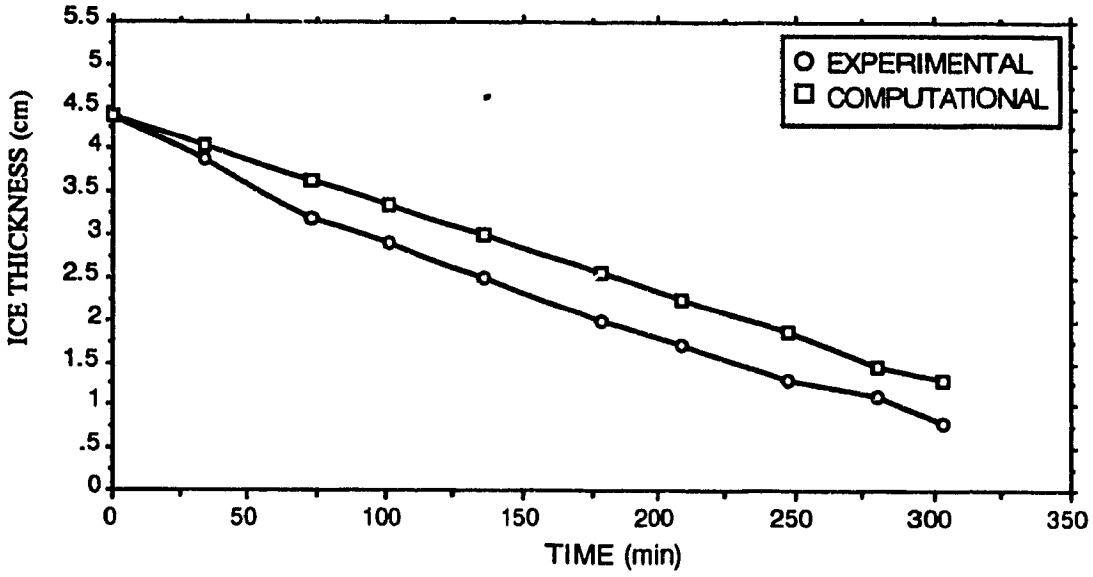

Figure 6.2.14: Ice cover thickness variation at 60 cm from the leading edge for experiment 7

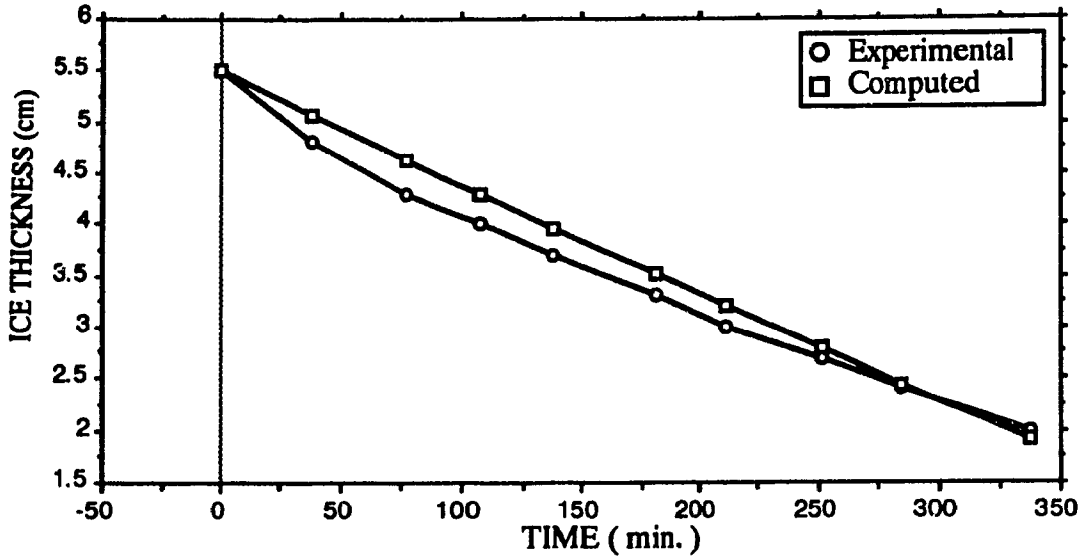

Figure 6.2.15: Ice cover thickness variation at 800 cm from the leading edge for experiment 7

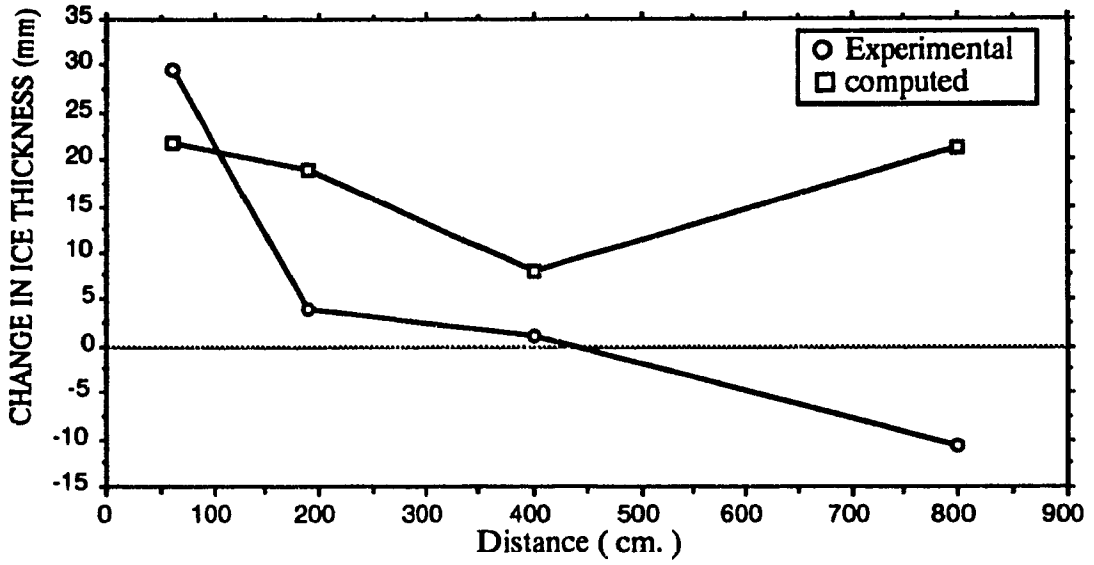

Figure 6.2.16: Maximum difference between the measured and computed thickness of the ice cover for experiments 1 and 7

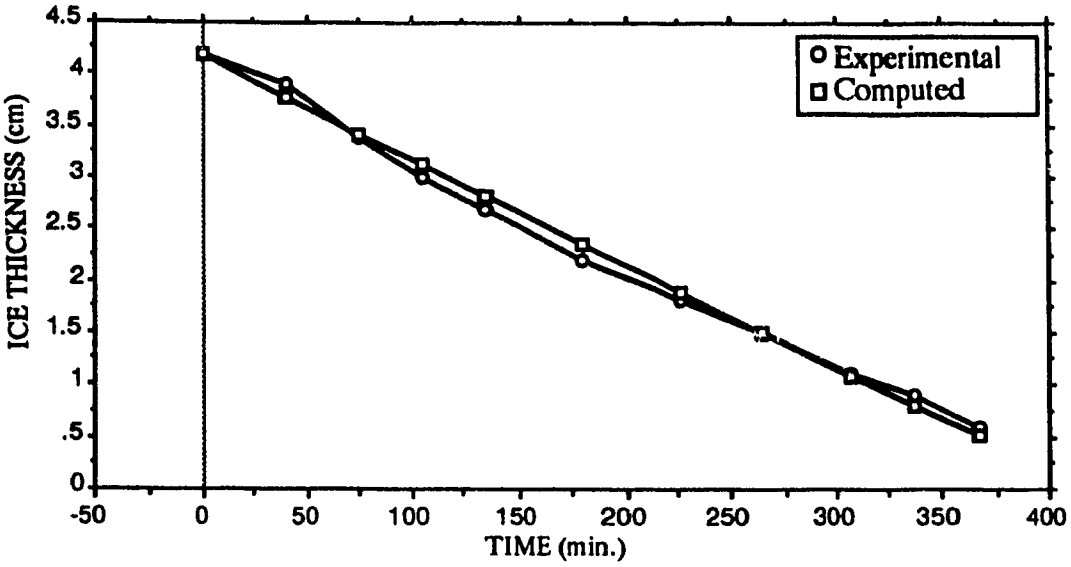

Figure 6.2.17: Ice cover thicknesses variation at 60 cm downstream of the leading edge for experiment 6

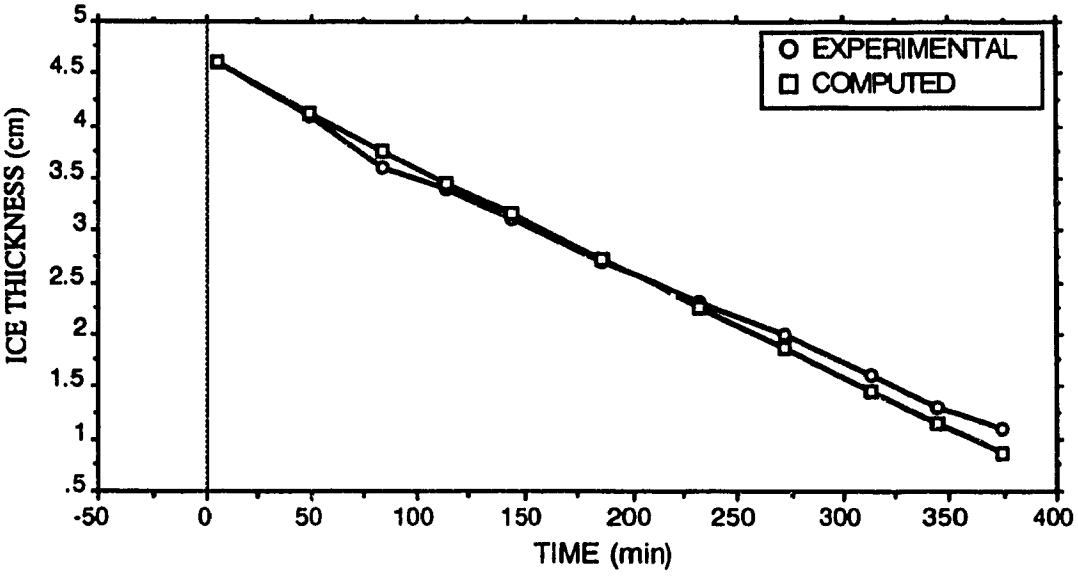

Figure 6.2.18: Ice cover thicknesses variation at 800 cm downstream of the leading edge experiment 6

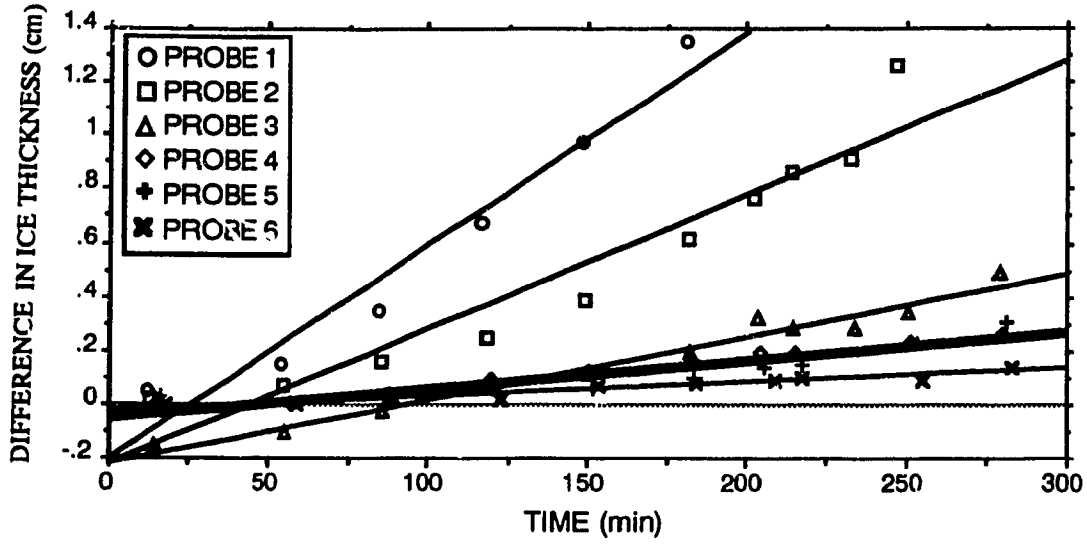

Figure 6.2.19: Difference in ice cover thickness for the first six probes in experiment 1

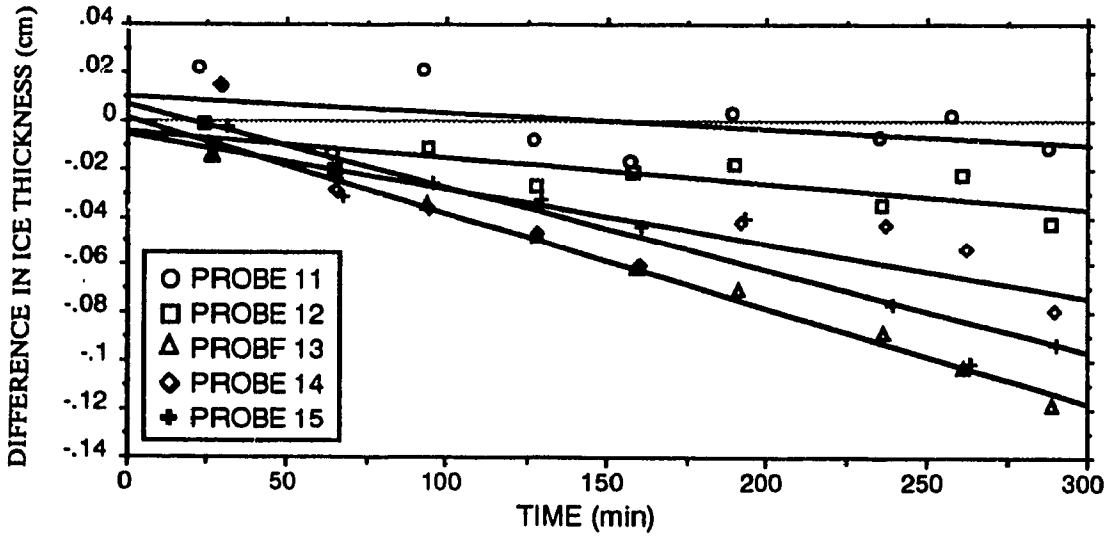

Figure 6.2.20: Difference in ice cover thickness for the last seven probes in experiment 1

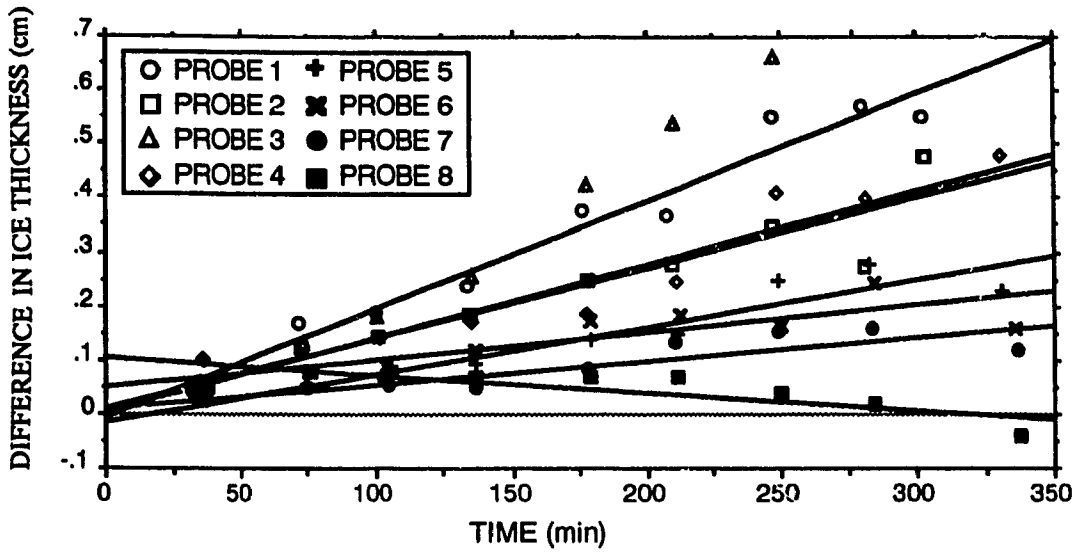

Figure 6.2.21: Difference in ice cover thickness at probe locations in experiment 7

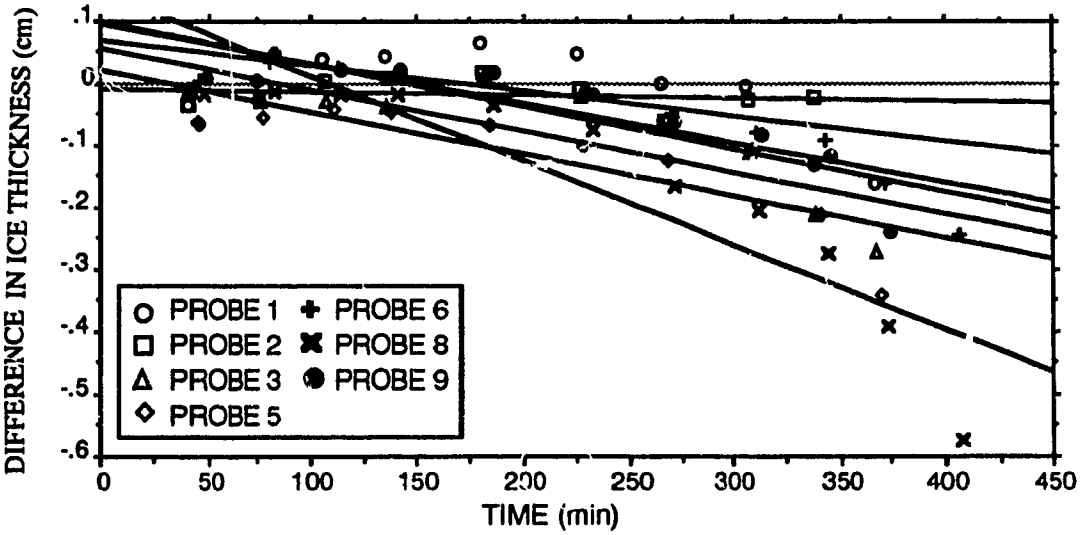

Figure 6.2.22: Difference between experimental and computed ice cover thickness for experiment 6

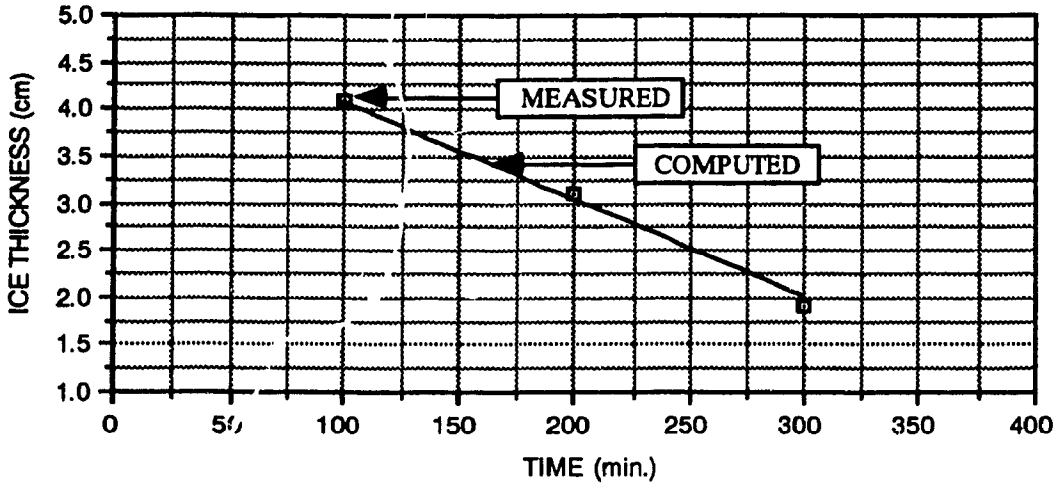

Figure 6.2.23: Average ice cover thickness for experiment 1

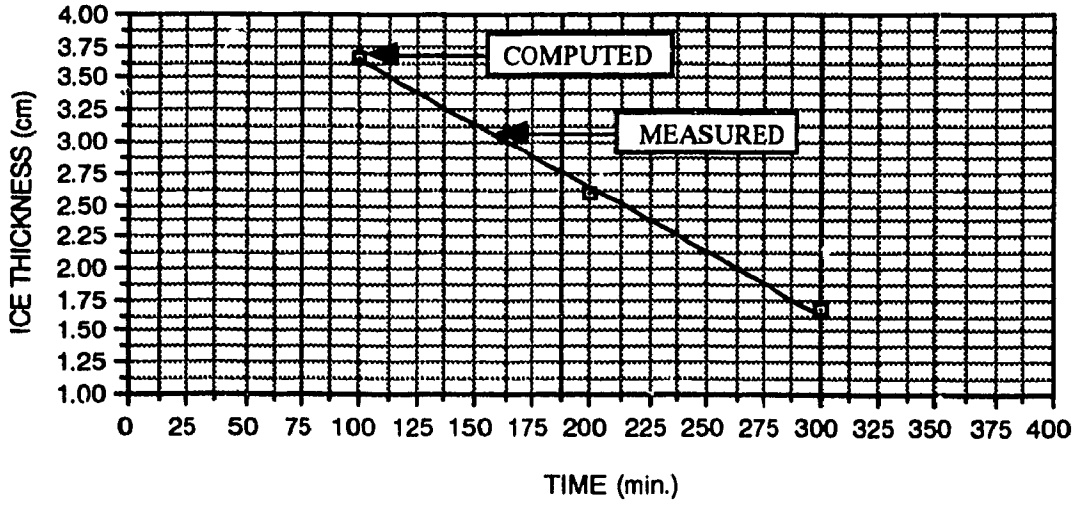

Figure 6.2.24: Average ice cover thickness for experiment 6

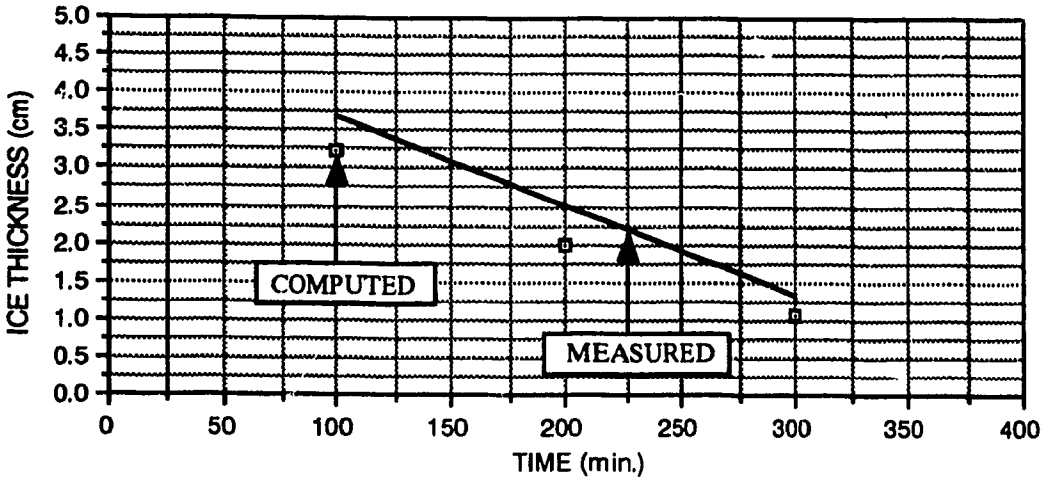

Figure 6.2.25: Average ice cover thickness for experiment 7

Comparison With Gallardos' Experiments

The experiments performed by Gallardo, 1974, were conducted in a flume 40 feet in length, 2 feet in width, and 1 foot in depth. Similar to the set-up used by Hewlett 1976, the channel setting included an uncovered portion in the inlet region, an ice covered portion in the middle of the channel, and another uncovered portion in the outlet region, such that the water flow undergoes a 2 feet free surface conditions, 25 feet ice covered conditions and a 1.5 foot free surface conditions respectively. The thickness of the ice was measured at the centre of 10 sections located along the flume as shown in figure 6.2.26.

The aim of Gallardo experiments, was to study the melting of an ice cover in relation to warm water and air temperature. The hydrodynamic and air temperature conditions for the experiments are shown in table 6.2.5. The water discharge was kept at a constant value of 0.8 cfs for all experiments, the air temperature was varied from 0.55°C to -9.44°C, and the average water temperature was varied from 0.34 °C to 0.41°C.

The experimental set-up was numerically reproduced by fitting the channel geometry and flow domain into a uniform rectangular grid system composed of 62 cells in the longitudinal direction and 12 cells in the transversal direction. The size of the cell was taken to be $\Delta x=0.145$ m and $\Delta y=0.06$ m. Measured air and water temperatures were accurately imposed. A wind velocity of 0.0 ms^{-1} was used for the numerical computations, since the three laboratory experiments that Gallardo carried out were performed without wind action. The cloud cover used was taken equal to nine tenth, in consideration for poor indoor lighting.

During the experimental investigation, an effort was made to achieve uniform distribution of temperature over the cross section, and in time. Uniform vertical temperature conditions were observed with a slight non-uniform temperature distribution over the whole cross section. This was due to the fact that the heat input was not well distributed across the width of the flume. A two-dimensional model based on the assumption of complete vertical mixing can therefore be justified for the use of hydrodynamic and hydrothermal computations under ice covered conditions. A constant temperature is thus imposed at the flume inlet. The experiments were fully reproduced for the flow, ice cover, and boundary conditions, and geometrical configuration.

The two-dimensional model was used to reproduce the laboratory experiments performed by Gallardo to investigate the ice cover melting rate and extent as a function of the water and air temperature. Figs. 6.2.27, 6.2.28, and 6.2.29 present the computed and measured ice cover thicknesses as a function of time at a typical probe, for experiments 2, 4, and 5 respectively. Computed ice cover melting is found to be repeatedly less than the measured values in all three experiments, and the difference between the measured and computed ice cover thickness is shown to be a function of time, water temperature and air temperature.

Fig. 6.2.27 (Tw=0.34°C, Ta=-1.11°C) show a maximum difference between computed and measured ice cover thickness of approximately 7%, while in fig. 6.2.29 (Tw=0.34°C, Ta=-9.44°C), a maximum difference of less than 2% is shown. However, the greatest difference is shown in figure 6.2.28 where the air temperature was -4.44°C and the water temperature was increased from 0.34°C to 0.41°C, where the maximum difference between computed and measured ice cover thicknesses is 20%.

Decreasing the air temperature from -1.11°C (fig.6.2.27) to -9.44°C (fig.6.2.29), but keeping the water temperature unchanged at 0.34°C, result in a more accurate prediction of the ice cover melting. The maximum difference between computed and measured ice cover thicknesses is reduced by approximately 50% from 4.5mm at -1.11°C to 2.2mm at -9.44°C, after 25000s and 32000s from the commencement of the ice cover melting. However, when water temperature is increased by 20% and the air temperature set at -4.44°C, the maximum difference between the measured and computed ice cover melting at approximately 26,500s of computational time, increases by 20% or in the order of 10mm.

This behaviour is also shown in Figs. 6.2.30, 6.2.31, and 6.2.32 which present the measured and computed longitudinal ice cover thickness profiles, at different time steps, for experiments 2, 4 and 5 respectively. The difference between measured and computed ice cover thickness profiles also shows to be increasing as a function of time, and water temperature. Although the difference might increase as a function of time and water temperature, the melting pattern of the computed ice cover thickness profiles are shown to be consistent for the experimental cases.

The results from experiments 2 and 5 show that the magnitude of the heat transfer at the ice-air interface to be significant at low water temperatures and high air temperatures, thus being the dominant factor in the change in thickness of the ice cover in time. However, at slightly higher water temperatures, the heat transfer at the water-ice interface dominates. Excluding the effects of the air temperature, a 17% increase in the water temperature results in a 3.8mm increase of the maximum difference between the measured and computed ice cover thicknesses, while on the other hand, a lowering of the air temperature by 750%, from -1.11°C to -9.44°C with no change in the water temperature, results in a change in the maximum difference between measured and

computed ice cover thickness of 2.3mm.

Therefore, during winter periods where the water temperature is low and the air temperature is at the subfreezing level, the dominant factor for the change in ice cover thickness is the air temperature. The heat gained at the bottom surface of the ice cover due to the water temperature is small compared to the heat lost to the atmosphere at the top surface of the ice cover. Therefore, the decrease of the ice cover thickness at the bottom surface of the ice cover is also small compared to the increase of the ice cover thickness at the top surface of the ice cover. Subject to such conditions, the rate of melting of an ice cover as a function of air temperature can be approximated by a straight line.

However, under different circumstances where the water temperatures is above an approximate value of 0.4°C, the heat flux at the top surface of the ice cover becomes small compared the heat gained at the bottom surface. Therefore, the ice cover melting occurs predominately at the water-ice interface. At air temperatures above the freezing point, the melting of the ice cover at the top surface behaves according to laws which are beyond the scope of this study.

Due to density effects the freshly melted water at the bottom surface of the ice cover should tend to remain in contact with the bottom surface, thereby forming a thin layer of cold water. The computed value of heat transfer at the water-ice interface is underpredicted due to the presence of the thin layer of melted water. which reduces the dispersion of the water temperature, and increases the temperature gradient at the interface. This increase in the temperature gradient, consequently increases the heat transfer across the interface. The difference between the computed and measured ice cover thicknesses as a function of time can therefore be attributed to the heat flux rate

from the water body to the ice cover, which is greater than the value computed using eq. 3.32.

The effect of the water temperature shown to be significant at values above 0.41°C. At water temperatures below that value, the air temperature comes into play to dominate the change in ice cover thickness as a function of time. On the hand, the influence of a 17% increase in the water temperature, result in a 3.8mm change in difference between measured and computed ice cover thicknesses. On the other hand, the influence of a 750% decrease in the air temperature, result in a 2.3mm change in difference between measured and computed ice cover thicknesses. For comparison purposes, a 10% increase in water temperature results in a 2.235mm change in the difference between measured and computed ice cover thicknesses, while a 10% decrease in the air temperature result in 0.031mm change in the difference between measured and computed ice cover thicknesses.

The computed ice cover thicknesses compare very good with measured ice cover thicknesses, at low water and air temperatures. At higher values of water temperatures, the computed ice cover thicknesses compare satisfactorily with the measured results. This can be shown in figs. 6.2.33, 6.2.34, and 6.2.35 which present the average ice cover thickness as a function of time. These figures show the overall behaviour of the ice cover melting in contrast to the typical behaviour at different locations on the ice cover, shown in figures 6.2.27 to 6.2.29. From a global point of view, the difference between the computed and measured average ice cover melting, is approximately 15% at Tw=0.34°C, Ta=-1.11°C (fig.6.2.34), 33% at Tw=0.41°C, Ta=-4.44°C (fig.6.2.35), and 7% at Tw=0.34°C, Ta=-9.44°C (fig.6.2.36). Therefore, in general the ice cover melting is accurately computed at low air temperatures, however, this accuracy is lost when the water temperature is above 0.4°C.

Table 6.2.5: Water and air temperature conditions for three experiments

CONDITIONS / RUN #	AVERAGE WATER TEMPERATURE (DEGREES CELCIUS)	AVERAGE AIR TEMPERATURE (DEGREES CELCIUS)
2	0.34	-1.11
4	0.41	-4.44
5	0.34	-9.44

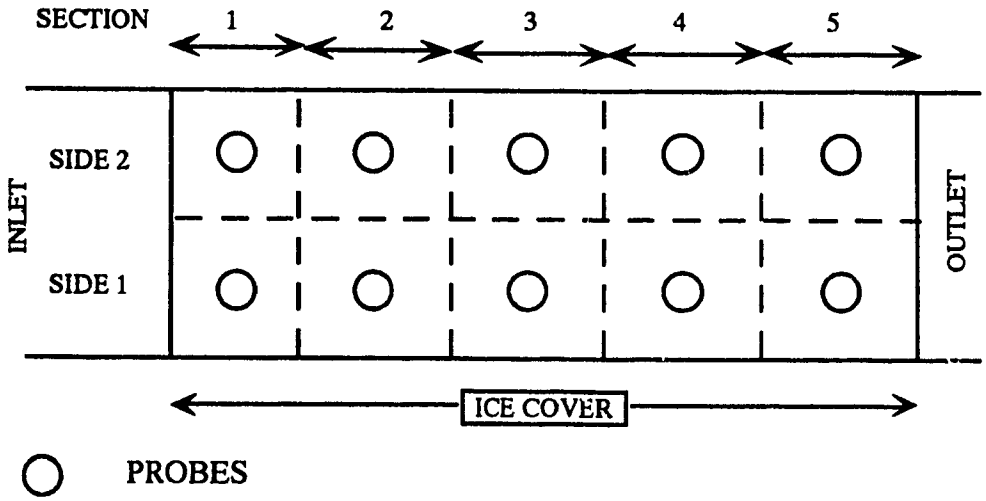

Figure 6.2.26: Channel Configuration Used by Gallardo

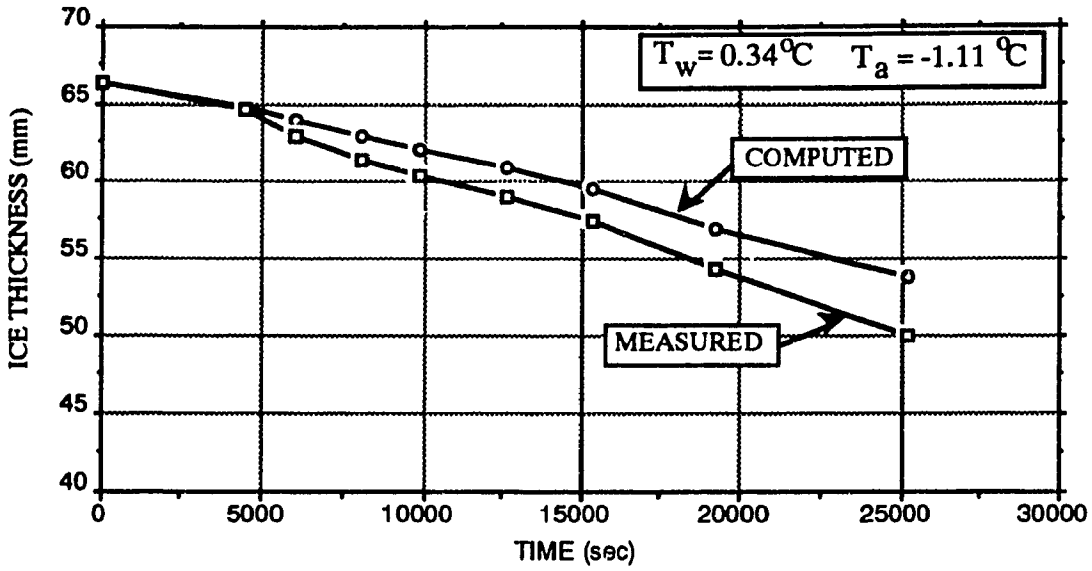

Figure 6.2.27: Ice Cover Thickness as a Function of Time for Experiment 2

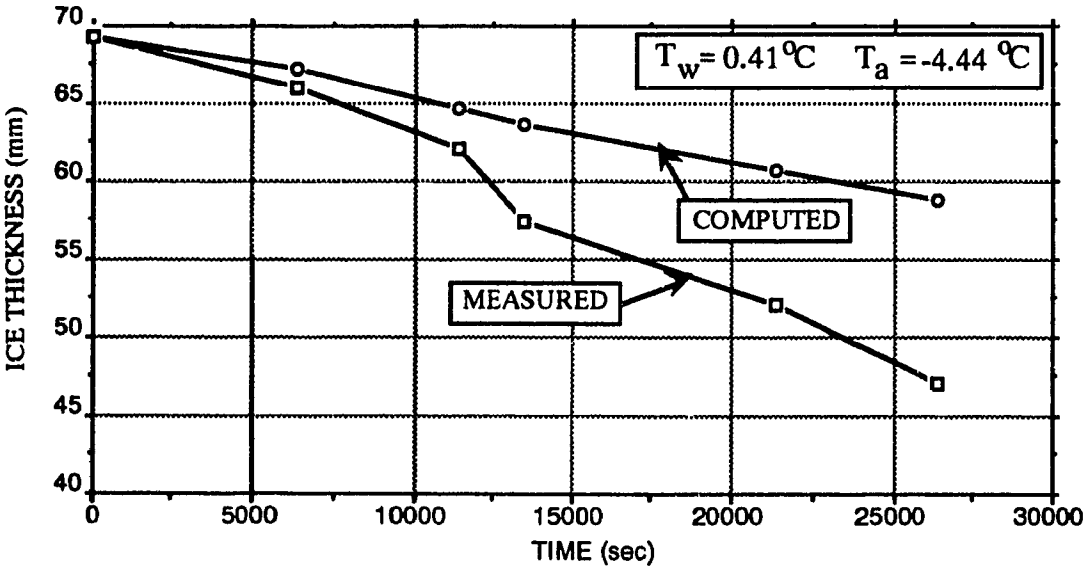

Figure 6.2.28: Ice Cover Thickness as a Function of Time for Experiment 4

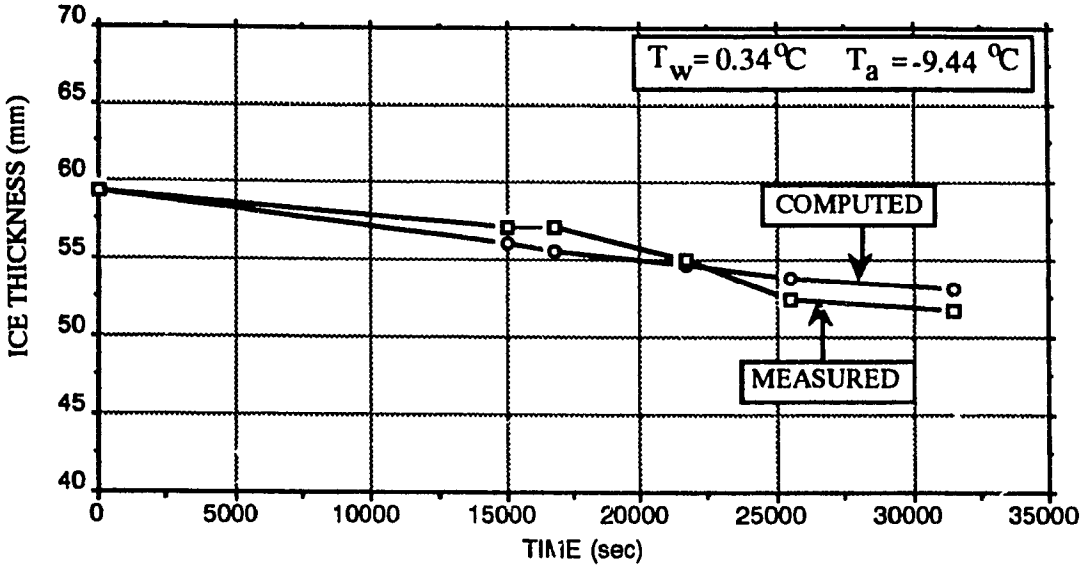

Figure 6.2.29: Ice Cover Thickness as a Function of Time for Experiment 5

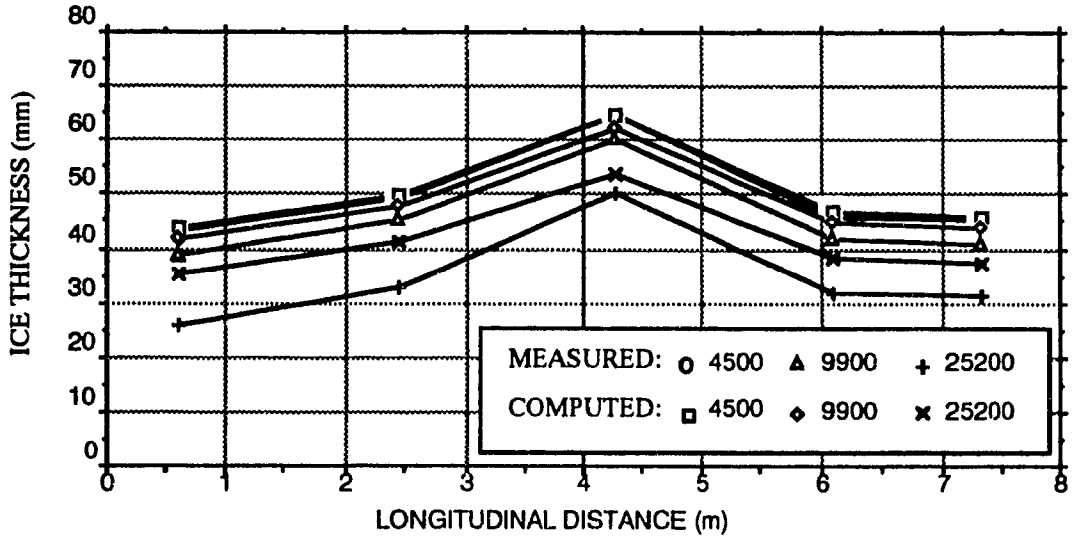

Figure 6.2.30: Longitudinal Ice Cover Thickness Profile for Experiment 2

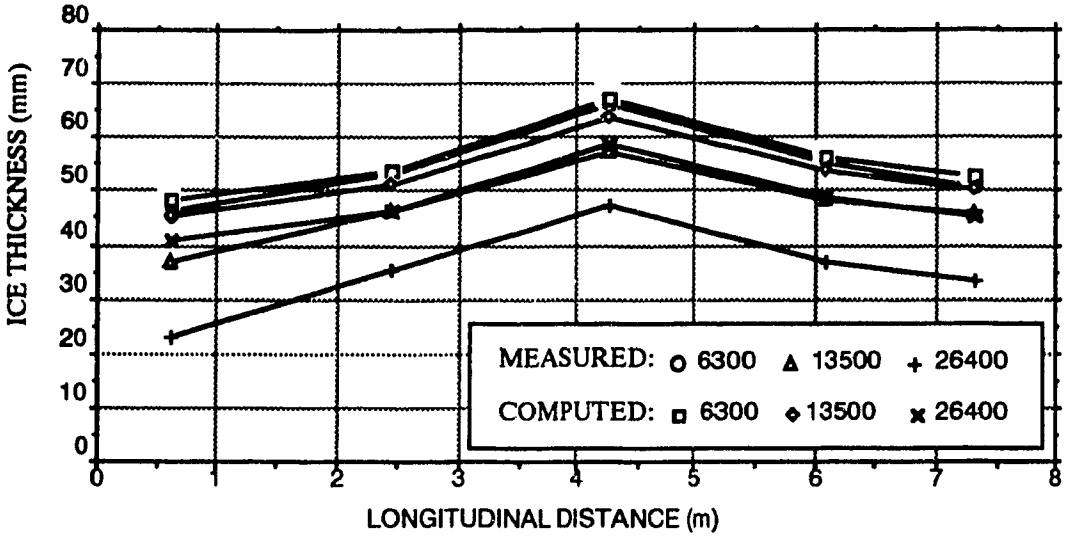

Figure 6.2.31: Longitudinal Ice Cover Thickness Profile for Experiment 4

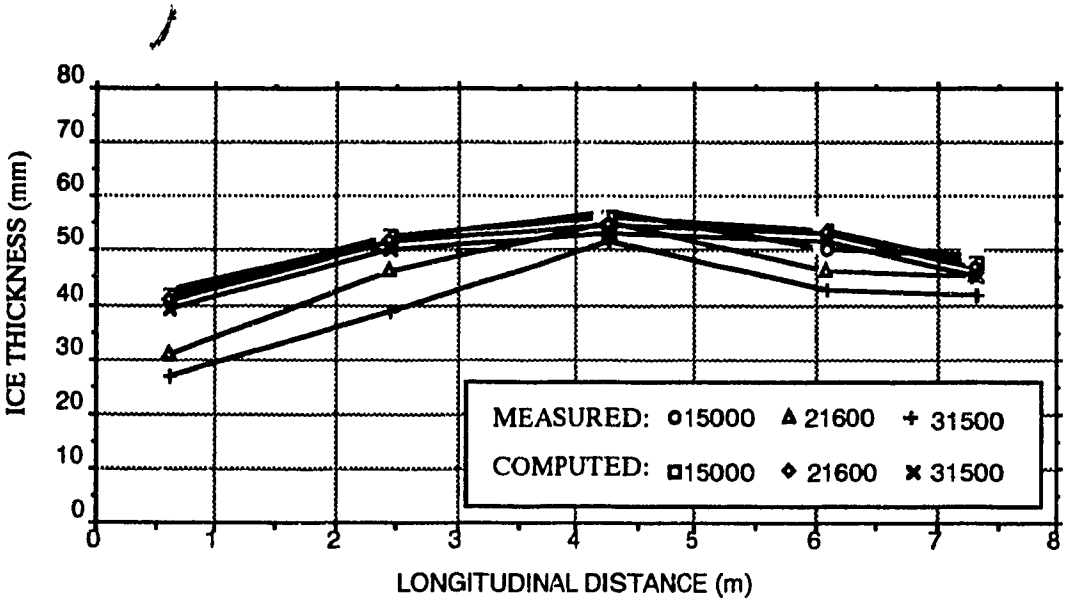

Figure 6.2.32: Longitudinal Ice Cover Thickness Profile for Experiment 5

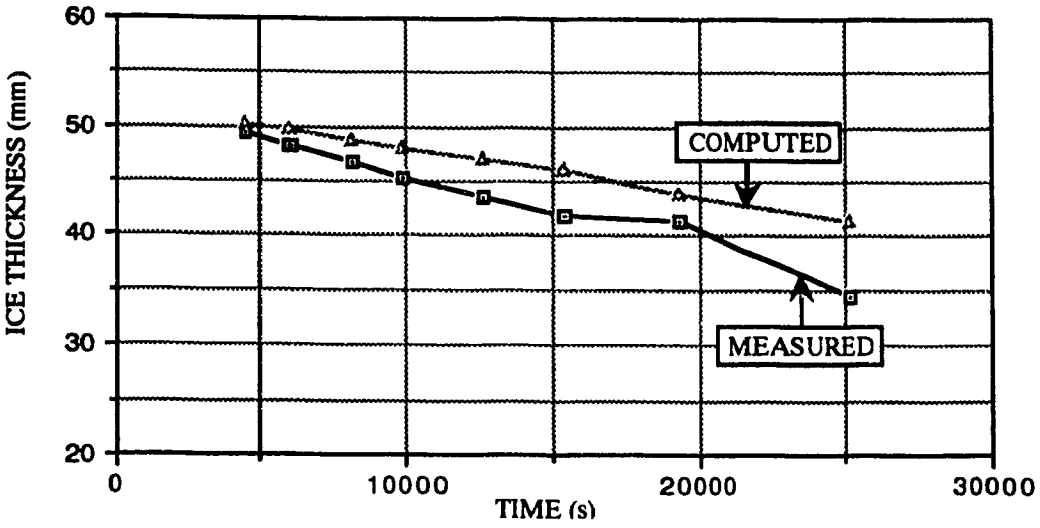

Figure 6.2.33: Average Ice Cover Thickness as a Function of Time for Experiment 2

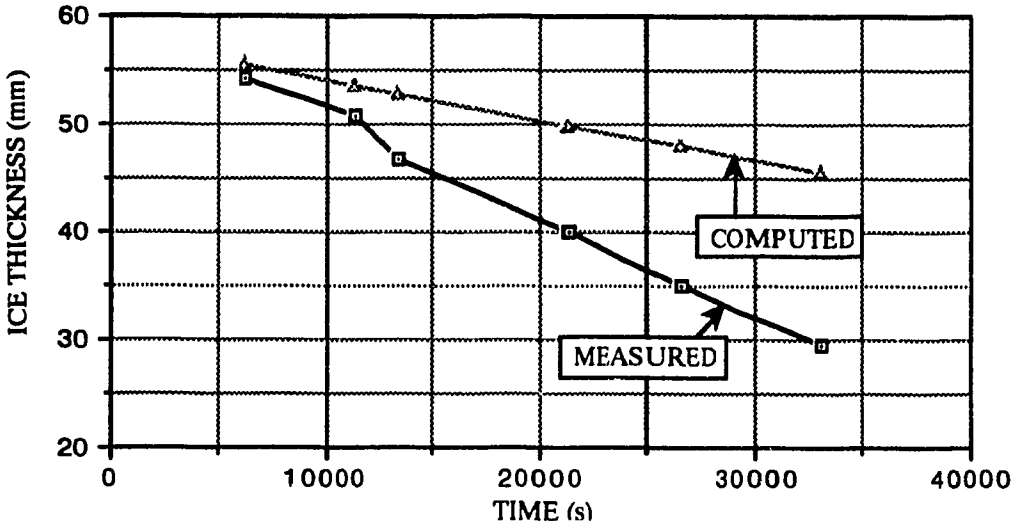

Figure 6.2.34: Average Ice Cover Thickness as a Function of Time for Experiment 4

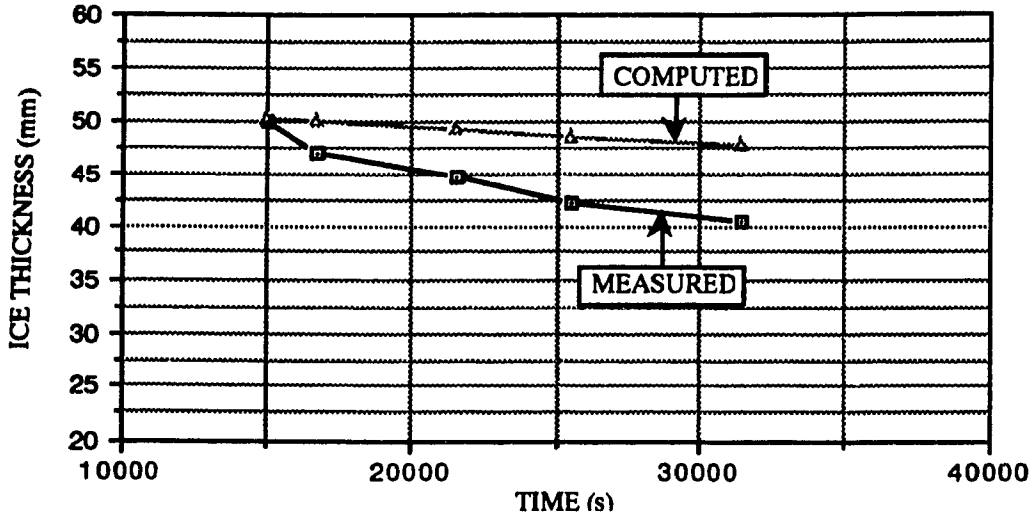

Figure 6.2.35: Average Ice Cover Thickness as a Function of Time for Experiment 5

6.3 Case Study

From February 13 to 18, 1980, a team under the direction of George Ashton of U.S.Army Cold Regions Research and Engineering Laboratory, Hanover, N.H., U.S.A., conducted a field investigation on the suppression of an ice cover on the Mississippi river, due to the discharge of warm water from the Riverside Power Plant of IOWA, Illinois Gas & Electric Co. near Bettendorf, IOWA. Figure 6.3.1 presents a plan view of the Mississippi River reach that was investigated, and table 6.3.1 identifies the locations at which the measurements were taken. An overall number of 16 locations where measurements were taken, spanning an approximate 9km downstream of the power plant. The measurements taken consisted of: velocity; temperature; and depth soundings together with aerial overflights to determine the extent of open water.

Presented in table 6.3.2, the Mississippi River is approximately 1,000 meters in width. The flow rate during the period of investigation was approximately 850 m^3s^{-1}. The flow depth along the side where the effluent is discharged varied between 1.22 meters and 2.74 meters and the magnitude of the current along the length of the study reach varied from 0.14 ms^{-1} to 0.34 ms^{-1}. The water temperature varied from 7.67^{0}C near the power plant discharge to 0.15^{0}C 9.0Km downstream of the power plant.

The river bathymetry was determined from river sounding charts obtained from the Rock Island Corps of Engineers. Although air temperatures were measured during the time of the field measurements, a more complete meteorological record of a three hour observation if available from the Moline, Illinois airport weather station. Also, cloud cover, wind speed, humidity and vapor pressure data were available. As shown in table 6.3.2, which presents the meteorological conditions for the 14th and 17th of February, the air temperature decreased from -2.13^{0}C to -18.75^{0}C thereby reducing

the length of the open water reach. Aerial photographs during the river overflights provided the ice cover edge location. The initial ice cover thickness of 0.25m extended upstream of the power plant discharge over the complete width of the river, therefore reducing the frazil ice deposition in the reach under study to negligible amounts.

The river bathymetry was fitted into a coordinate grid system with a Δx=62.5m and a Δy=25.0m. A reach of 12 Km was considered, such that the flow enters the study reach 3.0Km upstream of the power plant and exits approximately 9.0km downstream of the power plant. A Manning n of 0.030 was used, since the river reach under study consists of clay material with few rocks and relatively smooth transitions in the bottom elevation. The inflow water temperature was set to 0.05^{0}C, since a temperature of slightly above 0^{0}C was measured upstream of the power plant. A flow rate of 850m^{3}s^{-1} was imposed at the entrance. The meteorological conditions were used as indicated in table 6.3.2. A Manning coefficient of 0.020 for the underside of the ice cover was used. The time step was set to 2.5 sec., which satisfies the CFL criteria. A 6.27 ms^{-1} effluent velocity, and an effluent temperature of 8.9^{0}C were obtained from available thermal discharge characteristics power plant records.

The velocity distribution in the Mississippi River in presented in Figs. 6.3.2, 6.3.3, and 6.3.4. Transversal profiles are given at 5 locations along the river, namely at the entrance, effluent, 4600m from the entrance, 7720m from the entrance, and at the exit. The U-component, V-component, and resultant velocity transversal profiles are given in Figs. 6.3 2, 6.3.3, and 6.3.4 respectively.

The velocity enters at an angle of 40^o with the horizontal. Under an 850 m^{3}s^{-1} flow rate, the velocity profile at the entrance of the river, assumes a typical laminar velocity profile, since the flow at the entrance of the river is not yet fully developed. This laminar transversal velocity profile at the entrance of the channel is

experienced in other modelling test cases. The turbulent velocity is shown by the other profiles, from the effluent to the outflow region. The maximum entrance resultant velocity attains a value of 0.30 m s^{-1}. At the effluent region, the U-velocity component increases by about 10%, which is due to the effluent discharge velocity, the V-velocity increases by 50%, since the velocity of the effluent is along the v-direction and the channel orients more into the v-direction, and the resultant velocity increases by 30%. At 4600m from the entrance, the channel orients in the u-direction, thereby reducing the V-velocity by 70%, and increasing the U-velocity by 10%. Thereafter, the velocity maintains a constant value of 0.33ms^{-1} for the U-velocity, 0.1ms^{-1} for the V-velocity, and 0.34 ms^{-1} for the resultant velocity. At the exit of the reach, the velocity attains a value of 0.26ms^{-1}, 0.045ms^{-1}, and 0.27ms^{-1} for the U-velocity, V-velocity, and resultant velocity, respectively.

Fig. 6.3.5 presents the water depth distribution presented in the same format as Fig.6.3.2. This figure also provides a view on the bathymetry of the reach under study. The maximum depth occurs about the centre of the channel. The river has well defined over banks or flood plains. The transversal water depth profiles show that the river goes through a sharp transition from the banks to approximately 60% of the maximum depth. Around the centre of the channel, the depth increases again. The water depth for the first half of the reach takes an average value of 4.0m. The average depth becomes 5.0m and 7.5m at 7720m from the entrance and at the exit respectively. Therefore, the flow conditions in the river reach under study undergo shallow wide cross-section for 7km, then deep narrow cross-section for another 5km.

Fig. 6.3.6 shows the temperature distribution, presented in the same format as Fig.6.3.2. The temperature in the inflow region maintains the imposed river temperature by the model. At the effluent region, the temperature attains its maximum value of approximately 9°C, at the effluent source, and reduces exponentially to the

river temperature at the far bank. The temperature decreases gradually downstream of the effluent, and the maximum temperature value always remains attached to the near bank. Also, due to the meandering characteristics of the river reach, the temperature mixes more effectively in the transversal direction, such that the temperature at the far bank increase as well until the difference in the temperature between the far and near bank becomes in the order of 10%, as shown in Fig. 6.3.6.

Table 6.3.3 present a comparison between computed and measured range in values of depths, temperature, and mean velocity. The predicted mean depth fall within the measured range. The difference between the measured and computed maximum temperature, is in the order of 6%.The difference between the measured and computed maximum and minimum velocity, is 7% and 5% respectively. Therefore, the computed range in mean velocity, water depth, and temperature compare very well with measured value.

Figs. 6.3.7 to 6.3.9 present the computed and measured longitudinal profiles for temperature, velocity, and depth, respectively. Indicated on the figures, is the location of the measured and computed data point in the code form that is defined in Table 6.3.1. The computed temperature profile compares very well with the measured profile, as shown in Fig. 6.3.7. However, the model predictions show more dispersion in the transversal direction. This might be due to the buoyancy effects that are not included in the model. The density gradient due to high temperature gradients, imposes additional pressure on the fluid, thereby increasing the transport of temperature and consequently reducing dispersion. This effect is felt only in the near field region of the thermal effluent, which constitutes a distance of approximately 1.5km. Beyond that point, this effect is not felt.

Comparisons between measured and computed longitudinal velocity profiles are presented in Fig.6.3.8. The difference between the measured and computed velocities along the river reach vary from 50% at BRM-0, to 0% at MLD-4, to 10% at SLD-8. No special pattern is obvious, however the computed velocity fluctuates about the measured mean. This variable difference between the measured and computed velocities along the river length, can be attributed to the numerical discretization of the river boundaries, which follow a stepwise geometry.

The computed water depths compare excellent with the measured depths as shown in Fig.6.3.9, where the longitudinal depth profiles are presented. The difference between computed and measured water depths is negligible up to SLD-8. After that point, the difference increases from 0% to 18% at IBRG-11. Actually, the river narrows down, and increase in depth starting from SLD-8. Therefore, it is obvious that as long as the river is wide and shallow, the model provides excellent predictions of water depths, but when the river narrows and increase in depth, differences between computed and measured water depths begin to show. However, this is simply an observation, and need to be more investigated before definite conclusions are taken.

Figure 6.3.10 presents the computed location of maximum temperature of the thermal flume, and the measured midpoint of the ice free width from the near bank. The computed values compare very well with the measured data with a maximum percentage difference of approximately 15%. The maximum temperature location provides the position of the centre-line of the open water width since melting will occur along this line first, and then progress transversally. Therefore, the open water width and length can be well approximated through the prediction of the maximum temperature location profile. Based on the latter hypotheses, figure 6.3.10 implies that the ice free reach will be well predicted.

The ice free opening is investigated in the near field as shown in figure 6.3.11, and far field region as shown in table 6.3.4. The computed open water width presented in figure 6.3.11 for the near field ice free opening compares well with the measured values, however the ice edge location is overestimated by approximately 12%. If the latter figure is compared to figure 6.3.10, where the midpoint position of the ice edge and the location of the maximum temperature are presented, it is evident that the location of the maximum temperature truly is representative of the midpoint of the ice edge position.

Table 6.3.4 on the other hand, presents the computed and measured open water reach extents for both Feb. 14 and 17. The computed ice free reach of 7200m, underestimates the measured value of 8500m by approximately 15% for the Feb. 14 case, and 28% for the Feb. 17 case. In both cases, the difference between computed and measured ice free reach is acceptable since the difference is usually in terms of km's.

The computation of ice free openings under turbulent flow conditions and caused by the warm water discharge of a power plant compares well with measured data, and are in the same order of magnetude. The k-ε model provides reasonable predictions to the melting of an ice cover due to a thermal effluent and its use for this type of applications is therefore justifiable.

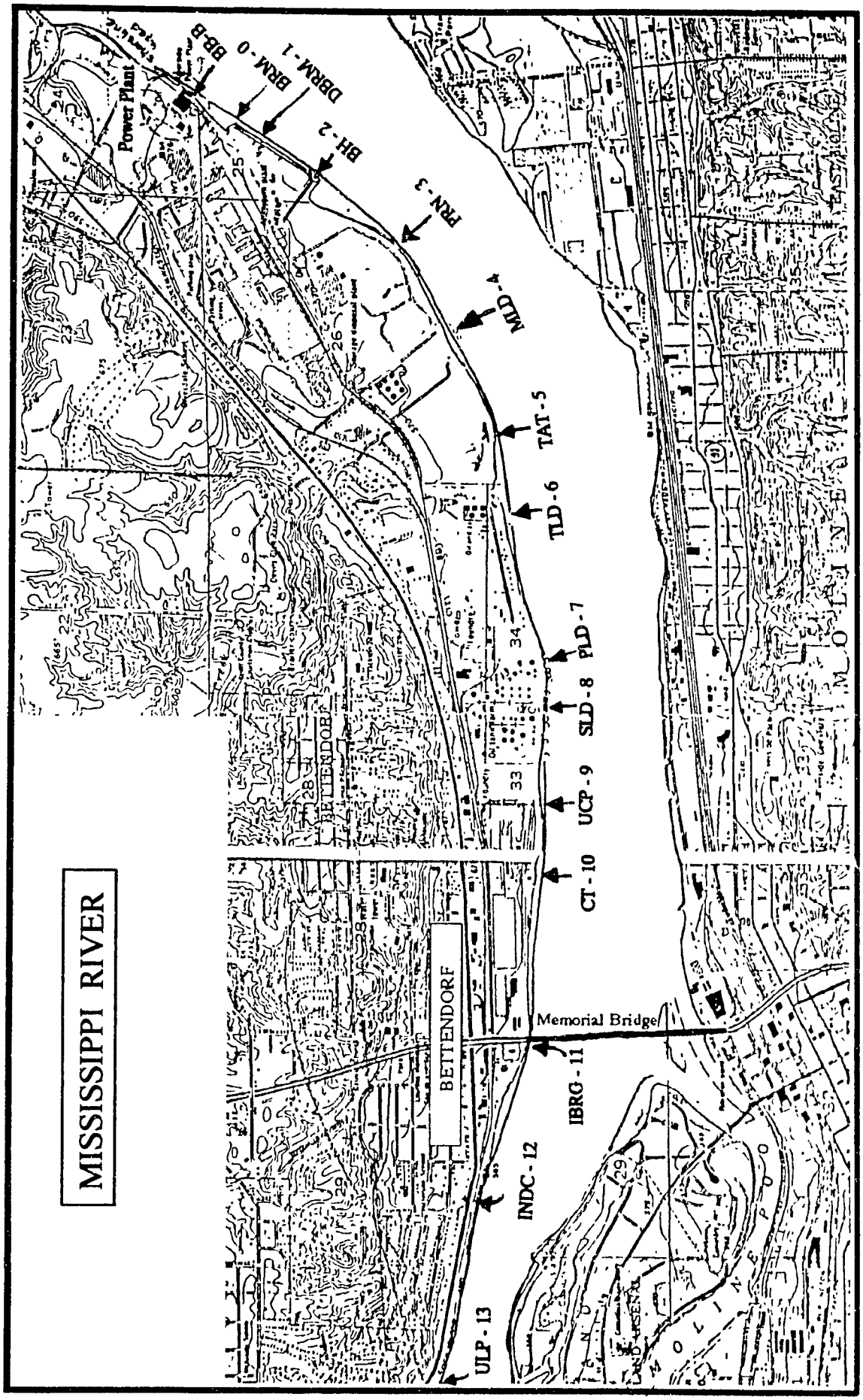

Figure 6.3.1. Plan view of the Mississippi river reach

Table 6.3.1. Locations where data were measured.

Location	Description	Distance from Origin (Km)
BB-B	midpoint of the Brick Building south of the Power Plant.	-0.216
BRM - 0	upstream end of the BeRM of Alcoa.	0
DBRM - 1	one third Downstream of the BeRM.	0.088
BH - 2	the Block House at the end of the berm.	0.097
PRN - 3	Point where the River Narrows.	1.260
MLD - 4	Midpoint between the three Loading Docks.	1.889
TAT - 5	The Turn Above the Texaco loading dock.	2.572
TLD - 6	Texaco Loading Dock.	3.017
PLD - 7	Phillips 66 Loading Dock.	4.022
SLD - 8	Shell Loading Dock.	4.315
UCP - 9	Upstream from the Case Plant along the edge of the building.	4.914
CT - 10	at the Case Tower.	5.346
IBRG - 11	At the I-74 BRidGe, (also the route 6 Memorial Brodge)	6.365
INDC - 12	INDECO Corporation.	7.348
ULP - 13	Upstream end of Lindsey Park.	8.453
BPB - 14	opposite the Brick Pill Box at the	8.794

Table 6.3.2. Meteorological conditions for Mississippi River.

Variable	February 14	February 17
Air Temperature	-2.13^0C	-18.75^0C
Cloud Cover	9.8	0.0
Wind Velocity	4.2 ms^{-1}	3.99 ms^{-1}
Vapour Pressure	2.1 mb	1.05 mb

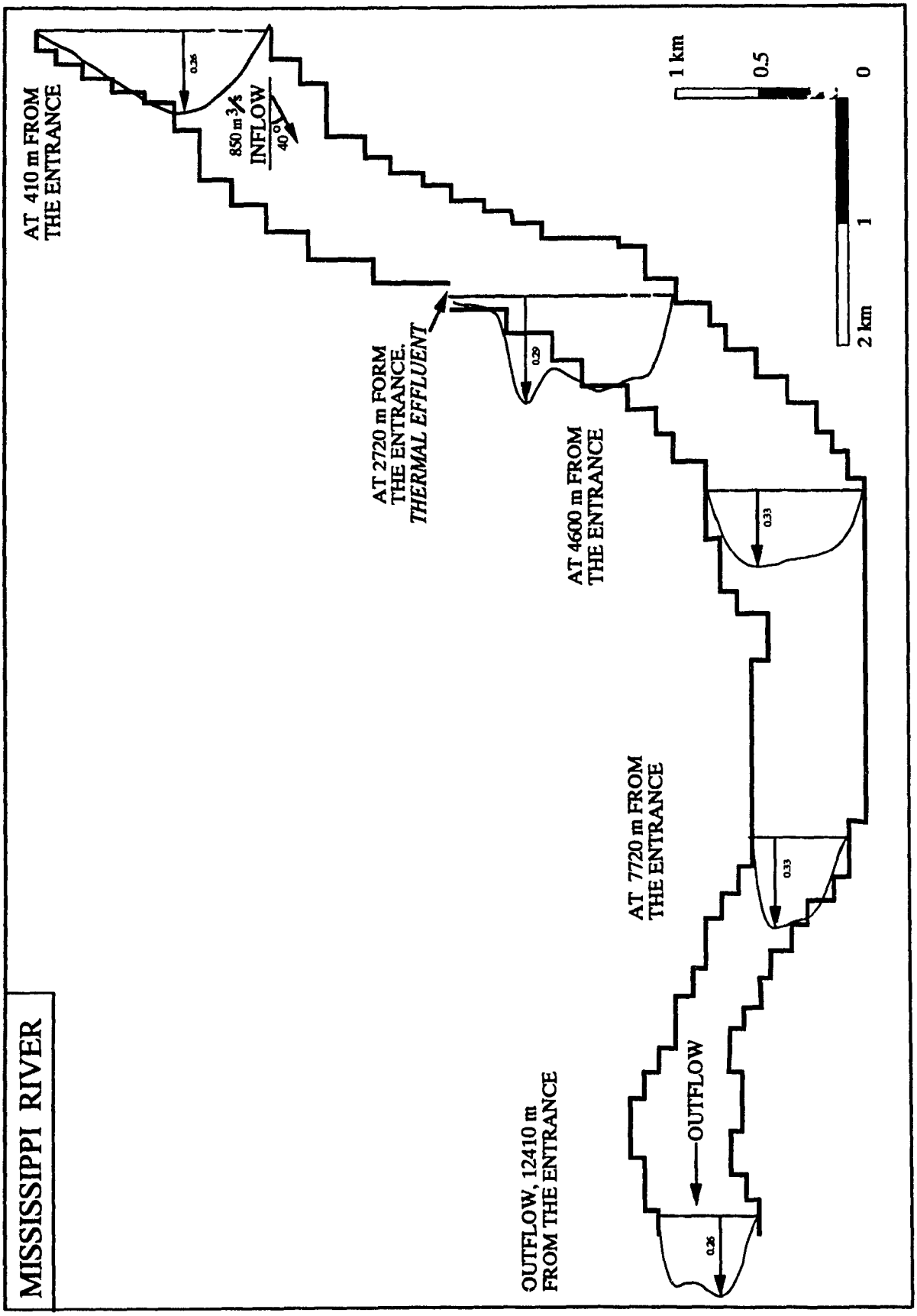

Figure 6.3.2: U-component transversal velocity profile, m s $^{-1}$

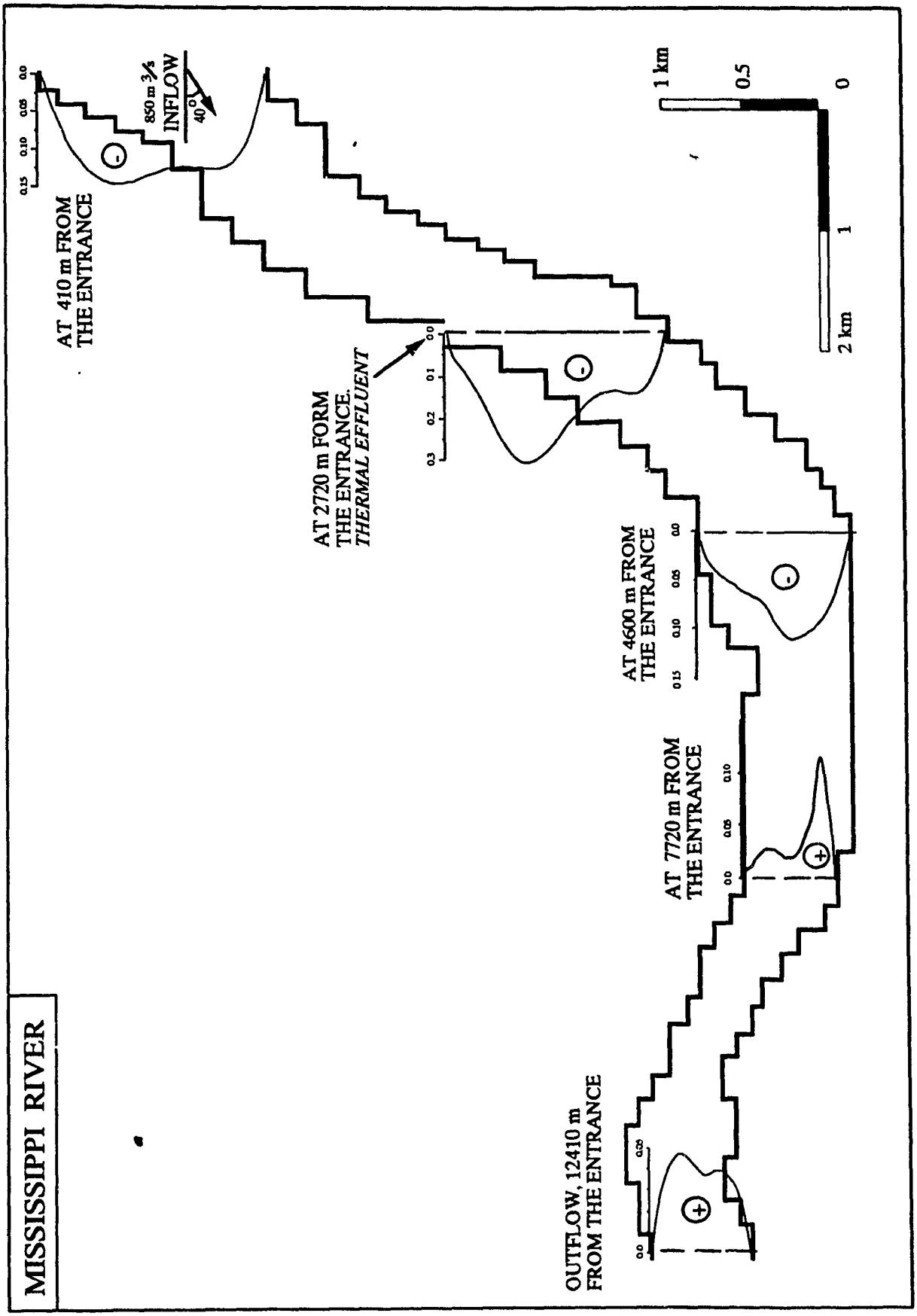

Figure 6.3.3: V-component transversal velocity profiles $m\,s^{-1}$

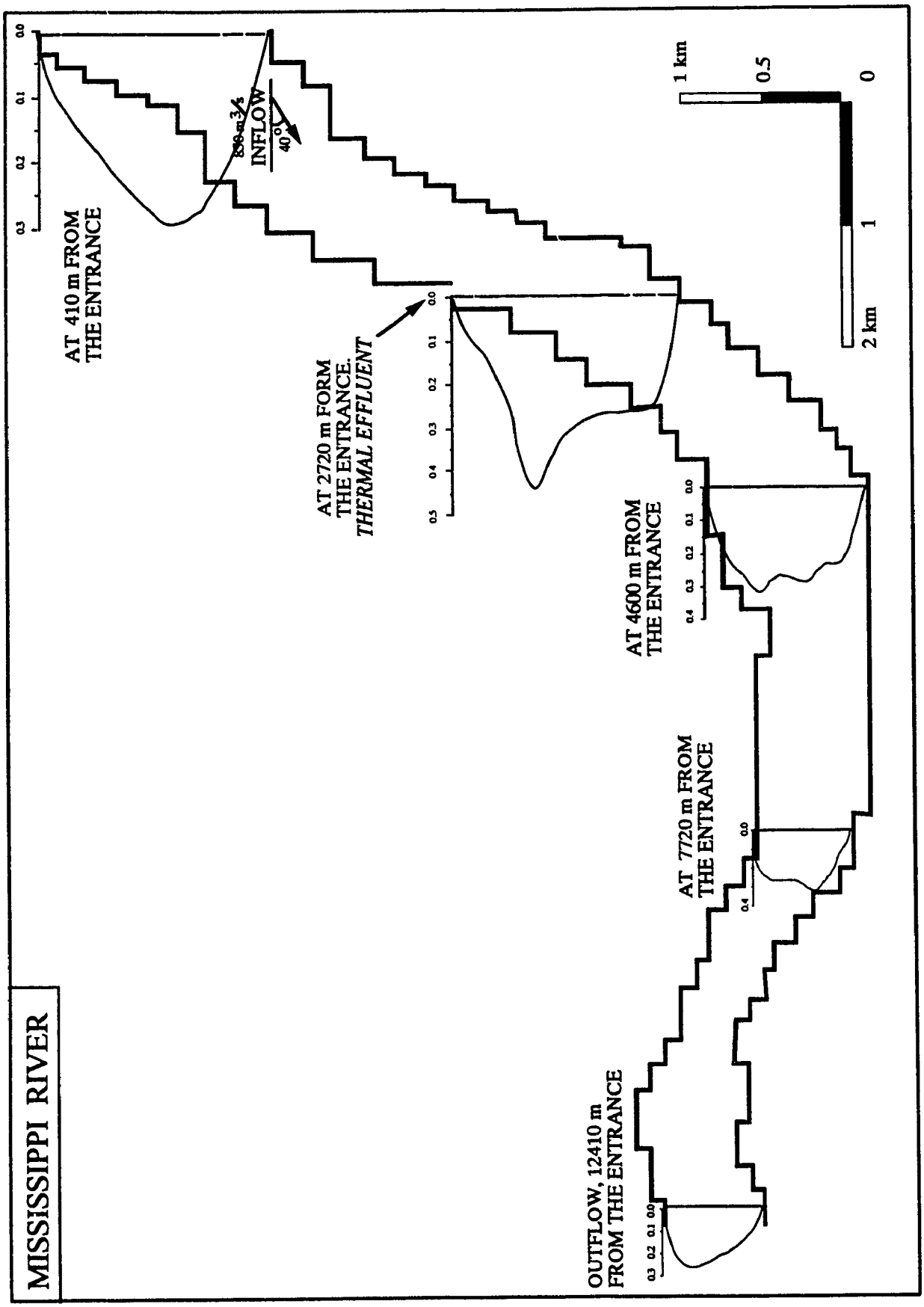

Figure 6.3.4: Resultant transversal velocity profile, $m s^{-1}$

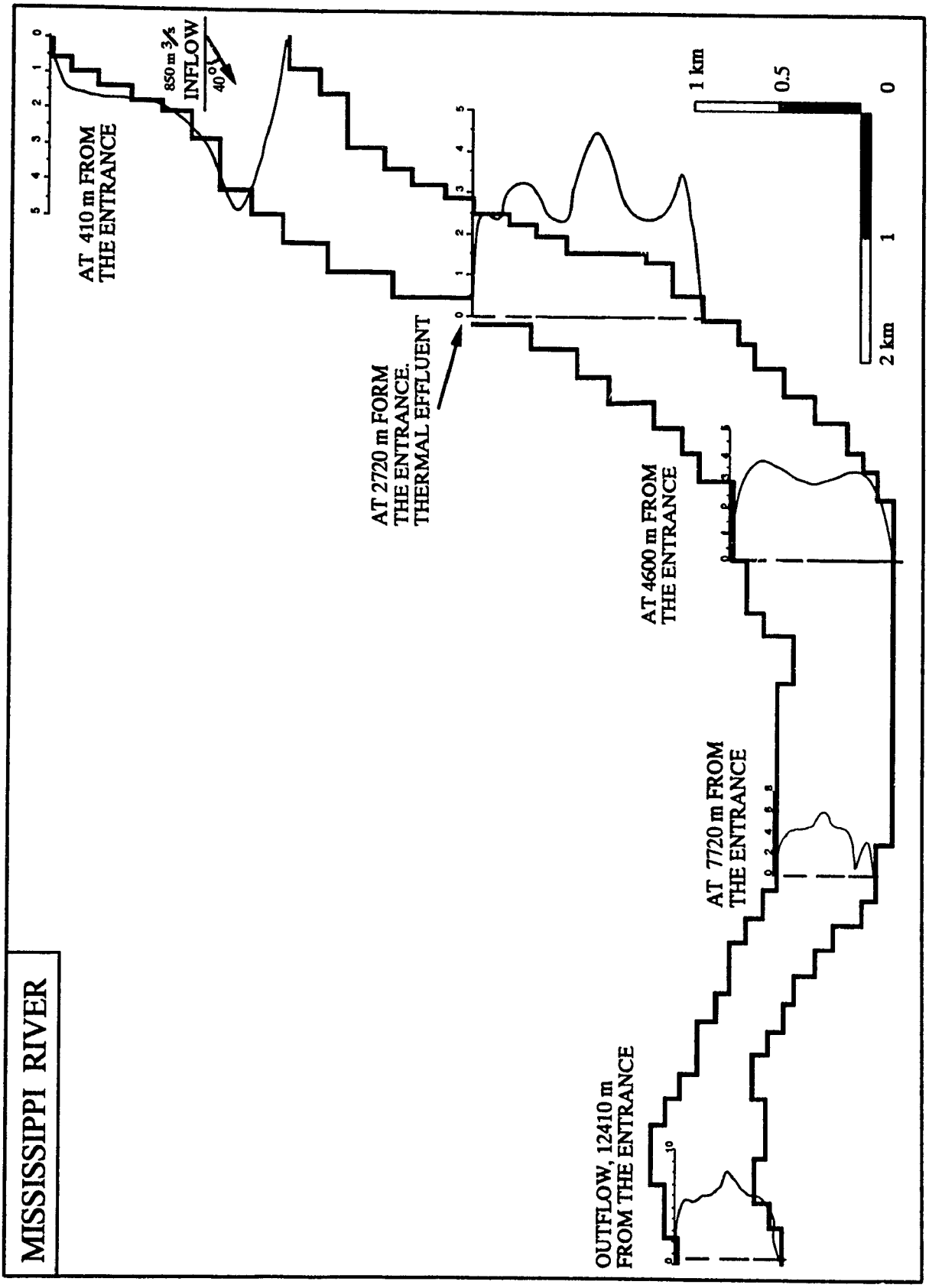

Figure 6.3.5: Transversal water depth profile, $m\,s^{-1}$

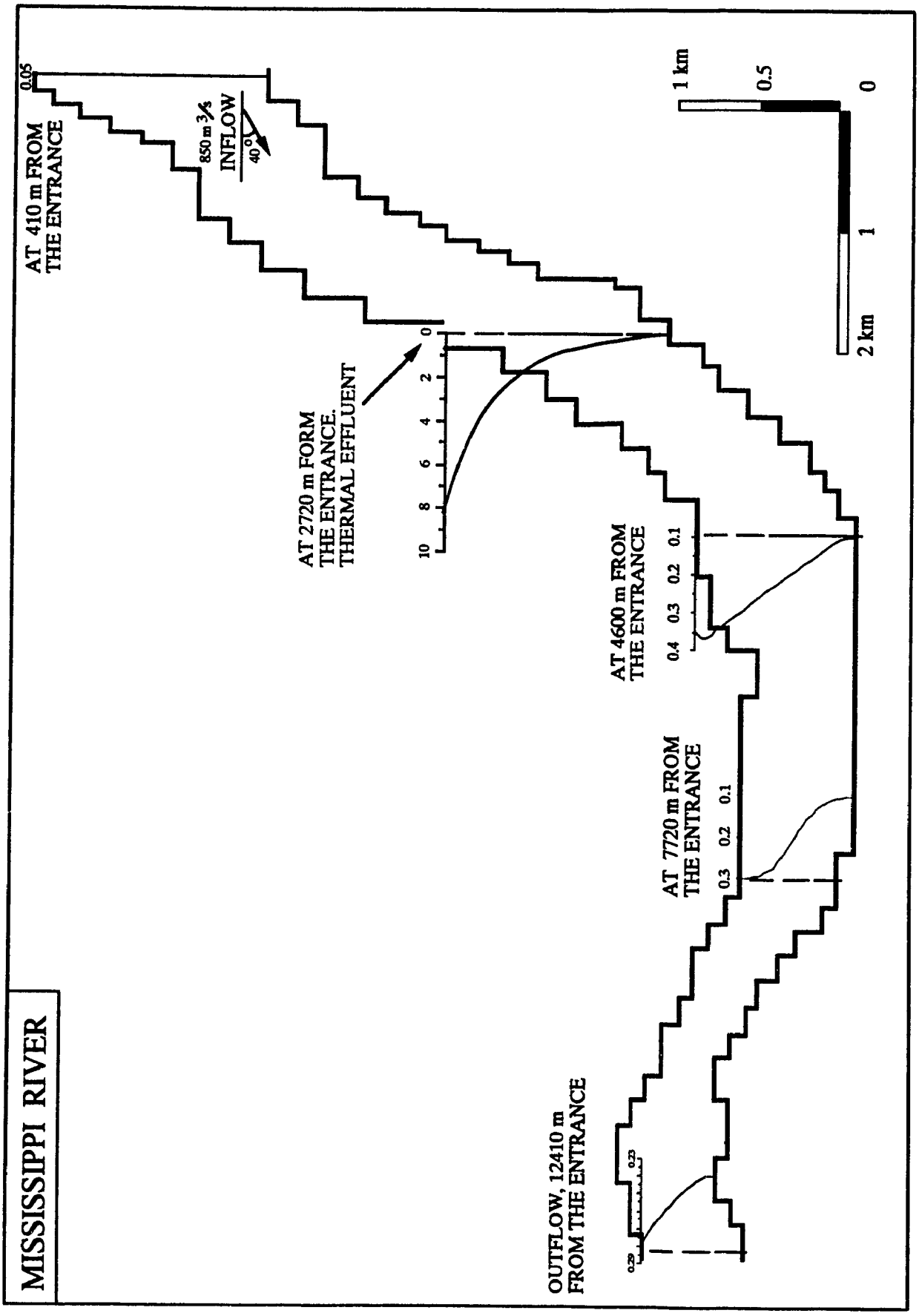

Figure 6.3.6: Transversal temperature profiles, $m\,s^{-1}$

Table 6.3.3. Range in the hydraulic conditions.

PARAMETERS	MEASURED RANGE	PREDICTED RANGE
Depth near effluent	1.22m - 2.74m	1.0 m - 2.5 m
Temperature	7.67 °C - 0.15 °C	7.19 °C - 0.20 °C
Mean velocity	0.14ms $^{-1}$ - 0.34ms $^{-1}$	0.13ms $^{-1}$ - 0.32ms $^{-1}$

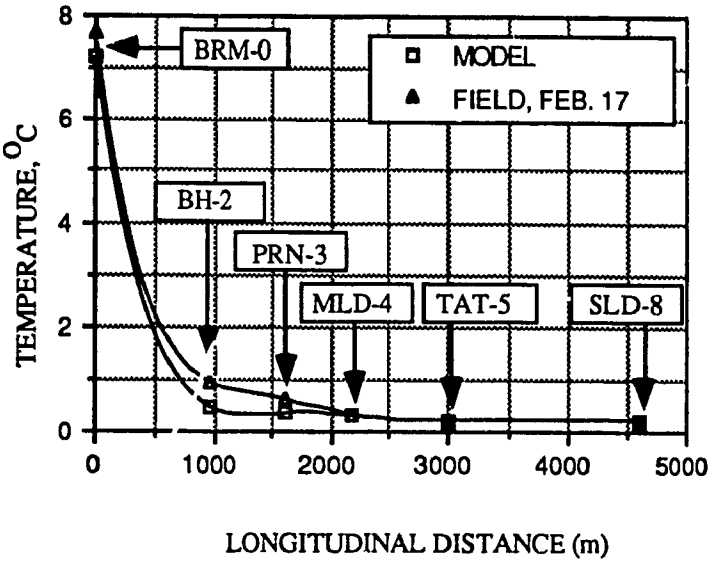

Figure 6.3.7: Longitudinal temperature profiles

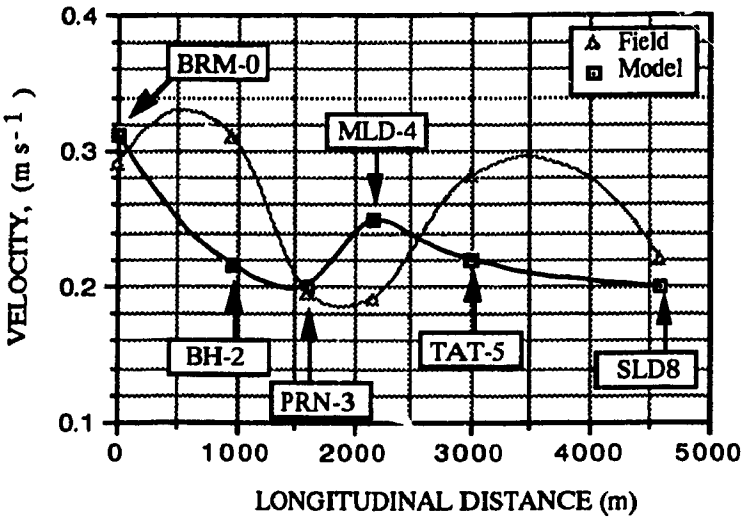

Figure 6.3.8: Longitudinal velocity profiles

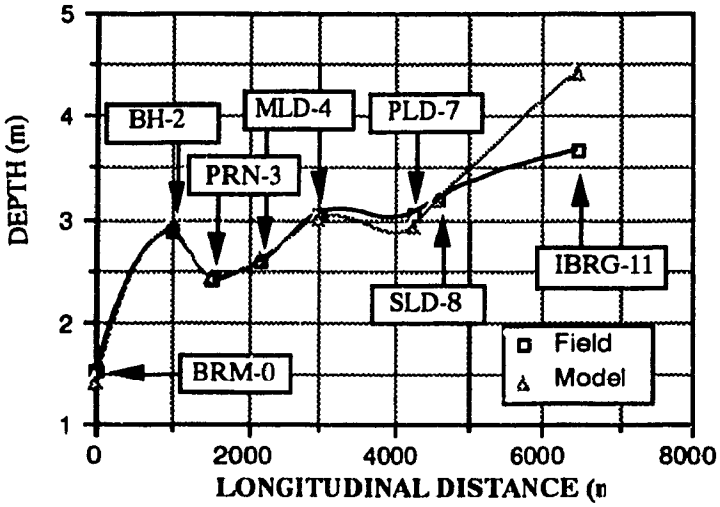

Figure 6.3.9: Longitudinal depth profiles along the near bank

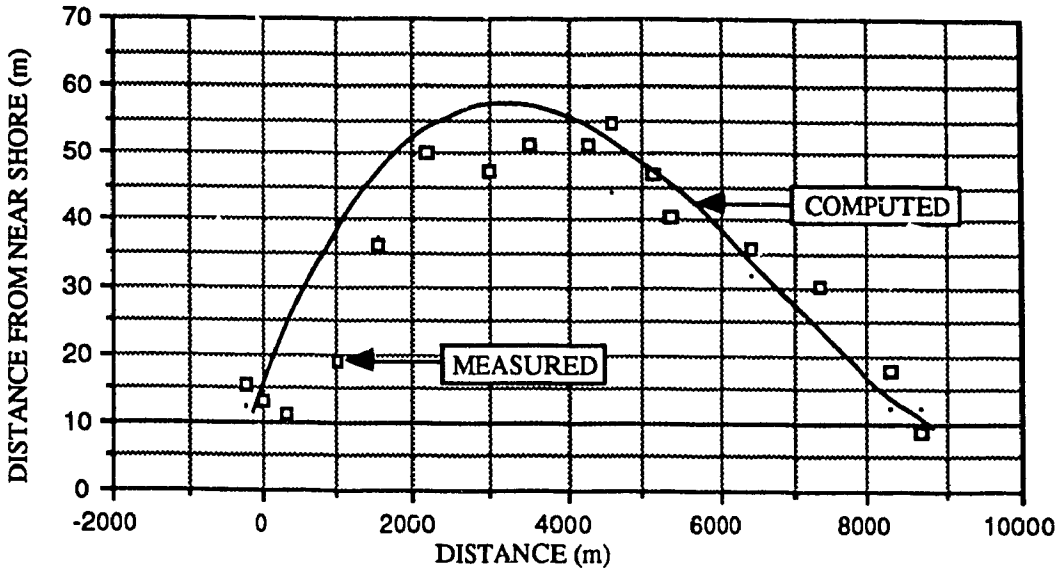

Figure 6.3.10: Midpoint position of ice edge from near bank

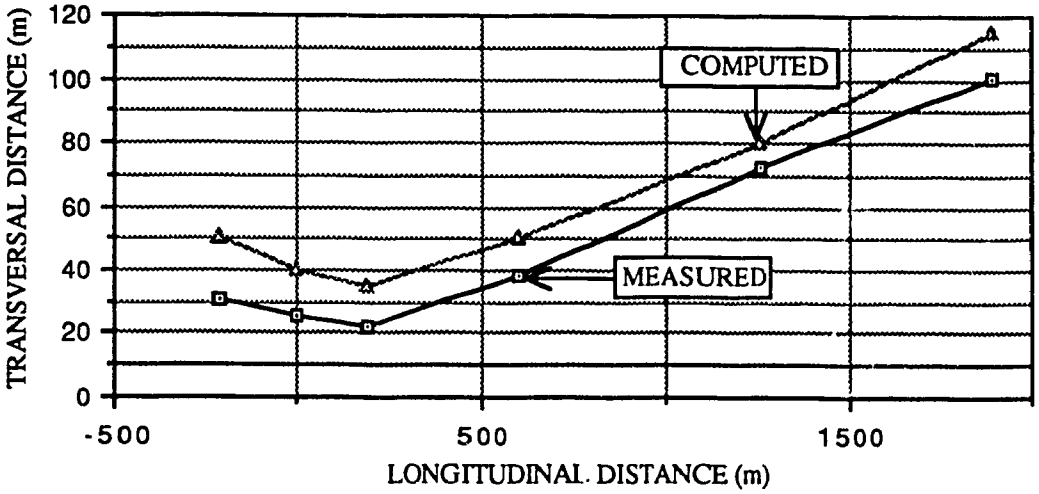

Figure 6.3.11: Near field ice free opening

Table 6.3.4: Length of ice free reach

DATE	MEASURED	COMPUTED
Feb. 14	8500	7200
Feb. 17	4300	3100

CHAPTER 7.0
CONCLUSION

The capability of predicting the magnitude and extent of ice cover melting due to an addition of heated thermal effluents, is important for the efficient use of rivers during the winter season. Therefore, predicting the melting of an ice cover due to added heat, under turbulent flow conditions is of interest to the present study. The study made use of a two-dimensional turbulence model to determine the turbulent flow characteristics, and the temperature distribution affecting the melting of the ice cover.

The model uses the depth-averaged two-dimensional St. Venant equations to solve for the hydrodynamic conditions, the two-dimensional heat equation to compute the temperature transport, the k and ε equations to evaluate the turbulent flow components, and ice equations to determine the extent of growth or melting of a floating ice cover.

The solution to the hydrodynamic equations was obtained through the application of a Modified version of the MacCormack scheme. The solution to the temperature, turbulent kinetic energy k, and the rate of dissipation of the turbulent kinetic energy ε equations were obtained by the use of the upwind finite difference scheme.

The verification of the model capability in predicting hydrodynamic conditions, was performed by comparing the model computations against other

modelling and experimental work done for a similar case that is considered in this study. The model compares well with other measured and computed hydrodynamic results, and in many cases, shows closer results to experimental data than the predictions of other works.

Once the hydrodynamic computations were verified, ice cover melting characteristics were investigated by using the k-ε model. This was performed by numerically reproducing 6 laboratory experiment. The model predictions compares excellent with four of the experiments and satisfactory with the remaining two. The primary reason for the satisfactory results with two of the experiments would be due to the difficulties encountered during the actual laboratory experimentations and the inadequacies involved with the growing and maintaining of a stable ice cover during the experiments. The latter series of tests, gave rise to the problem of melting in the leading edge region, where an increased amount of melting occurs. Beyond a certain distance from the leading edge region, the computed melting rate of the ice cover compares well with measured values. Also, the prediction of melting of the ice cover is more accurate under low air temperatures, however, as soon as the water temperature rises above 0.4°C, the computed melting of the ice cover diverges from the actual value. This is due to the heat transfer coefficient at the water-ice interface which should be more accurately evaluated.

The model was then used to validate its applicability by investigating the ice cover melting of a river in comparison with a field case. The field study selected is one that was done on the Mississippi river. Comparison with hydrodynamic measurements show an overall agreement in the range and mean values. The computed temperature distribution and ice free openings compare very well with the measured values.

Therefore, from a general point of view, the results show a very good performance of the model in predicting, the hydrodynamic, and hydrothermal conditions, as well as the melting pattern and extent of an ice cover.

However, the accuracy of the predictions is a function of the air temperature, water temperature, and the heat transfer coefficient, provided that the hydrodynamic and hydrothermal distributions are well computed. With that in mind, a few recommendation can be given to enhance the computations of ice cover melting characteristics.

When relatively elevated water temperatures are involved, buoyancy effects begin to play an important role in both the maximum jet entrainment and consequently the dispersion of temperature. Furthermore, this might have an effect in the reduction of the ice free width in the near field region since an increase in the temperature dispersion will occur. However, the ice free reach length in the downstream region may not necessarily be affected.

Also, the heat transfer coefficient in the present work was shown to be highly underestimated in the leading edge region. Therefore, the investigation of ice cover melting in the leading edge region, using other methods, is of prime necessity for better predicting the melting rate of the ice cover leading edge progression.

In meandering rivers, which is mostly the case, the water surface elevation in bends across a unique cross section may vary in the order of meters. This two dimensional water surface variation has an effect of the hydrodynamics and consequently on the temperature distribution in the river.

Last but not least the temperature at the ice surface is actually not the temperature of the air, but rather a function of it. This is also another feature that can be investigated to better predict the overall melting or thickening of the ice cover.

REFERENCES

1. Anderson, E.R. (1959), "Energy Budget Studies", in Water-Loss Investigations: Lake Hefner Studies, TR, U.S. Geological Survey, Professional Paper 269, pp.71-118.

2. Ashton, G.D. (1979), "Suppression of River Ice by Thermal Effluents", U.S. Army Cold Regions Research Engineering Laboratory, CRREL Report 79-30, Hanover, N.H., Dec.

3. Ashton, G.D. (1980), "Unpublished Field Data", Mississippi River Study Personal Notes Received During Visit at U.S. Army Cold Regions Research Engineering Laboratory, Hanover, N.H., November 1986.

4. Ashton, G.D. (1981), "River Ice Suppression by Side Channel Discharge of Warm Water", IAHR International Symposium on Ice Proceedings, Quebec, Quebec, pp. 65-81.

5. Ashton, G., "Theory of Thermal Control and Prevention of Ice in Rivers and Lakes", CRREL.

6. Carter, H.H. (1969), 'A Preliminary Report on the Characteristics of a Heated Jet Discharged Horizontally Into a Transverse Current. Part 1-Constant Depth, Chesapeake Bay Inst., Johns Hopkins University, Tech. Rep. no. 61.

7. Chapman,S.R. (1985), "Application of The Two-Equation k-ε Turbulence Model to a Two-dimensional Steady, Free Surface Flow Problem With Separation", International Journal for Numerical Methods in Fluids, Vol. 5, pp. 257-268.

8. Chapman, S.R. (1982), "A numerical simulation of two-dimensional separated flow in a symmetric open-channel expansion using the depth integrated two-equation (K-Epsilon) turbulence closure model", Verginia Polytechnic Institute and State University, Ph.D. thesis.

9. Chow, V.T. (1957), "Open Channel Hydraulics", McGraw Hill, New York, N.Y.

10. Demuren, O.A., and Rodi, W. (1983), "Side Discharges into Open Channels: Mathematical Model", Journal of Hydraulic Engineering, Vol. 109, No. 12.

11. Dingman, S.L., Weeks, W.F. and Yen, Y.C. (1967), "The Effects of Thermal Pollution on River Ice Conditions, Part 1, A General Method of Calculation", U.S. Army Cold Regions Research Engineering Laboratory, CRREL Report 206, Hanover, N.H.

12. Engman, E.O. (1977), "Turbulent Diffusion in Channels with a Surface Cover", Journal of Hydraulic Research, Vol. 15, No. 4, pp. 327-335.

13. Garcia, F.R. (1983), "Mathematical Modelling of Two-Dimentional Hydraulic Problems Using a Fully-Dense Finite-Difference Scheme", M.Sc.A. Thesis, Ecole Polytechnique de Montreal, August.

14. Garcia, R., and Kahawita, R. (1986), "Numerical solution of the St. Venant Equations with the MacCormack Finite Difference Sheme", International Journal for Numerical Methods in Fluids, Vol. 6, pp. 259-274.

15. Hayes, F.D., and Ashton, G.D. (1979), "Turbulent Heat Transfer in Large Aspect Channels", U.S. Army Cold Regions Research Engineering Laboratory, CRREL Report 79-13, Hanover, N.H., May.

16. Hayes, F.D., and Ashton, G.D. (1985), "River Ice Suppresion by Thermal Discharges", U.S. Army Cold Regions Research Engineering Laboratory, CRREL Preliminary Report Work Unit No. 322 89, Hanover, N.H., April.

17. Hewlett, Y. B. (1976), "Rate of Recession of The Leading Edge of Ice Covers on Open Channel Flows", University of Iowa, Masters Thesis.

18. Lam, L.Y., and Krishnappan, G.B. (1981), "Ice Cover Effects on Stream Flows and Mixing", (ASCE) Journal of the Hydraulics Division, Proceedings of the American Society of Civil Engineers, Vol. 107, No. HY10, pp.1225-1242.

19. Launder, E.B., and Spalding, B.D. (1974), "The Numerical Computation of Turbulent Flows", Computer Methods in Applied Mechanics and Engineering 3, pp. 269-289.

20. McGuirk,J.J., and Rodi,W. (1978), "A Depth-Averaged Mathematical Model for The Near Field of Side Discharges Into Open-channel Flow", Journal of Fluid Mechanics, Vol.86, Part 4, pp.761-781.

21. Mikhail, R., Chu, V.H. and Savage, S.B. (1975), "The Reattachment of a Two-Dimensional Turbulent Jet in a Confined Cross Flow, Proc. 16th IAHR Cong., Sao Paulo, Brazil, Vol.3, pp.414-419.

22. Paily, P.P., Macagno, E.O. and Kennedy, J.F. (1974), "Winter-Regime Surface Heat Loss from Heated Streams", Iowa Institute of Hydraulic Research, IIHR Report No. 155, Iowa City, Iowa, March.

23. Paily, P.P., and Macagno, E.O. (1974), "Thermal Response of Heated Streams, Solution by the Implicit Method", Iowa Institute of Hydraulic Research, IIHR Report No. 165, Iowa City, Iowa, May.

24. Patankar, V.S. (1980), "Numerical Heat Transfer and Fluid Flow", Mc.Graw-Hill Book Company, N.Y.

25. Plouffe, R. P. (1987), "Two-Dimensional Modelling of Local River Ice Cover Melting Due to a Side Thermal Effluent", Concordia University, Masters Thesis.

26. Rastogi, K.A., and Rodi, W. (1978), "Prediction of Heat and Mass Transfer in Open Channels", Journal of The Hydraulics Division, ASCE, Vol. 104, No. HY3, March.

27. Report of the Task Committee on Hydrodynamics of Ice of the Committee on Hydromechanics of the Hydraulic Division (1974), "River-Ice Problems: A State-Of-The-Art Survey and Assessment of Research Needs",

28. Roache, P.J. (1976), "Computational Fluid Dynamics", Hermosa Publishers, Alburquerque, N.M.

29. Rodi, W. (1980), "Turbulence Models And Their Applications In Hydraulics - A State Of The Art Review", University of Karlsruhe, Karlsruhe, GFR, pp.1-33.

30. Rotta, C.J. (1975), "Prediction of Turbulent Shear Flow Using the Transport Equations for Turbulence Energy and Turbulence Length Scale", Von Karman Institute for Fluid Dynamics, Lecutre series 76.

31. Roman Gallardo, A. M. (1974), "Influence of Air and Water Conditions on The Melting Rate of Ice Covers", University of Iowa, Masters Thesis.

32. Shen, T.S., and Chiang, L. (1984), "Simulation of Growth and Decay of River Ice Cover", Journal of Hydraulic Engineering, ASCE, Vol. 110, No. 7, July, pp. 958-971.

33. Schertzer, W.A. (1978), "Energy Budget and Monthly Evaporation Estimates for Lake Superior, 1973", Journal of Great Lake Research, Vol.4, No. 3-4, December, pp.320-330.

34. Tennekes, H. and Lumley, L.J. (1974), "A first course in Turbulence", The MIT Press, Massachusetts.